

The Schottky emitter as a source for multi-electron-beam instruments

Guo, X.

DOI

[10.4233/uuid:304cdd73-083a-4f89-ad47-f192e84a5313](https://doi.org/10.4233/uuid:304cdd73-083a-4f89-ad47-f192e84a5313)

Publication date

2024

Document Version

Final published version

Citation (APA)

Guo, X. (2024). *The Schottky emitter as a source for multi-electron-beam instruments*. [Dissertation (TU Delft), Delft University of Technology]. <https://doi.org/10.4233/uuid:304cdd73-083a-4f89-ad47-f192e84a5313>

Important note

To cite this publication, please use the final published version (if applicable). Please check the document version above.

Copyright

Other than for strictly personal use, it is not permitted to download, forward or distribute the text or part of it, without the consent of the author(s) and/or copyright holder(s), unless the work is under an open content license such as Creative Commons.

Takedown policy

Please contact us and provide details if you believe this document breaches copyrights. We will remove access to the work immediately and investigate your claim.

The Schottky emitter as a source for multi-electron-beam instruments

Guo, X.

DOI

[10.4233/uuid:304cdd73-083a-4f89-ad47-f192e84a5313](https://doi.org/10.4233/uuid:304cdd73-083a-4f89-ad47-f192e84a5313)

Publication date

2024

Document Version

Final published version

Citation (APA)

Guo, X. (2024). *The Schottky emitter as a source for multi-electron-beam instruments*. [Dissertation (TU Delft), Delft University of Technology]. <https://doi.org/10.4233/uuid:304cdd73-083a-4f89-ad47-f192e84a5313>

Important note

To cite this publication, please use the final published version (if applicable). Please check the document version above.

Copyright

Other than for strictly personal use, it is not permitted to download, forward or distribute the text or part of it, without the consent of the author(s) and/or copyright holder(s), unless the work is under an open content license such as Creative Commons.

Takedown policy

Please contact us and provide details if you believe this document breaches copyrights. We will remove access to the work immediately and investigate your claim.

The Schottky emitter as a source for multi-electron-beam instruments

Guo, X.

Publication date
2024

Citation (APA)
Guo, X. (2024). *The Schottky emitter as a source for multi-electron-beam instruments*.

Important note
To cite this publication, please use the final published version (if applicable).
Please check the document version above.

Copyright
Other than for strictly personal use, it is not permitted to download, forward or distribute the text or part of it, without the consent of the author(s) and/or copyright holder(s), unless the work is under an open content license such as Creative Commons.

Takedown policy
Please contact us and provide details if you believe this document breaches copyrights.
We will remove access to the work immediately and investigate your claim.

**THE SCHOTTKY EMITTER AS A SOURCE FOR
MULTI-ELECTRON-BEAM INSTRUMENTS**

THE SCHOTTKY EMITTER AS A SOURCE FOR MULTI-ELECTRON-BEAM INSTRUMENTS

Proefschrift

ter verkrijging van de graad van doctor
aan de Technische Universiteit Delft,
op gezag van de Rector Magnificus prof. dr. ir. T.H.J.J. van der Hagen,
voorzitter van het College voor Promoties,
in het openbaar te verdedigen
op woensdag 4 september 2024 om 10.00 uur

door

Xiaoli GUO

Master of Electronic Science and Technology,
Xi'an Jiaotong University, China,
geboren te Xinxiang, China.

Dit proefschrift is goedgekeurd door de promotoren.

Samenstelling promotiecommissie:

Rector Magnificus	voorzitter
Em. prof. dr. ir. P. Kruit	Technische Universiteit Delft, promotor
Prof. dr. ir. J. P. Hoogenboom	Technische Universiteit Delft, promotor

Onafhankelijke leden:

Prof. dr. P. Steeneken	Technische Universiteit Delft
Prof. dr. W. M. J. M. Coene	Technische Universiteit Delft
Prof. dr. ir. O. J. Luiten	Technische Universiteit Eindhoven
G. A. Schwind	ThermoFisher Scientific USA
Dr. C. W. Hagen	Technische Universiteit Delft, reservelid

The work in the thesis has been carried out with financial support from Applied Materials Israel, Ltd. (Israel) and its subsidiary Integrated Circuit Testing GmbH (Germany).



Keywords: Schottky source, Multi-beam instrument, Scanning electron microscope

Printed by: Gildeprint

Cover: A photo from the thesis.

The author set this thesis in L^AT_EX using the Libertinus and Inconsolata fonts.

Copyright © 2024 by X. Guo
ISBN 978-94-6384-617-2

An electronic version of this dissertation is available at
<http://repository.tudelft.nl/>.

CONTENTS

1	Introduction	1
1.1	Overview of SEM applications in the semiconductor industry	1
1.1.1	The basics of a scanning electron microscope	1
1.1.2	SEM for metrology and inspection in the semiconductor industry	2
1.1.3	Multi-beam system as a high throughput SEM	3
1.2	Challenges of the Schottky source used in a multi-beam source	6
1.2.1	Electron sources used in the SEM and lithography	6
1.2.2	Different electron Sources	8
1.2.3	The emission theory and optic theory of the Schottky source	10
1.2.4	Challenges for the off-axial beams in a Schottky source	12
1.3	Practical challenges in manufacturing a multi-beam source	12
1.4	Scope of the thesis	13
2	Electron optics theory of the off-axial electron beams in a Schottky source	15
2.1	Introduction	15
2.2	Principle of CPO2D and Schottky Emission model in it.	19
2.3	The extended Schottky emission theory	20
2.4	Aberration coefficient calculation from electron trajectories	21
2.4.1	Geometric aberration for the off-axial beams	21
2.4.2	Virtual source positions for the off-axial beams.	36
2.4.3	Chromatic dispersion analysis	38
2.5	Virtual source characteristics for off-axial beams	39
2.6	Conclusions	43
3	Emission properties of a 1.0-micron radius Schottky source	45
3.1	Introduction	45
3.2	The characterization setup for a large radius (1.0 μm) Schottky emitter	46
3.3	Angular intensity calculation algorithm and its map in angular coordinate.	47
3.4	Emission patterns and I-V curves for different temperatures	49
3.5	Long-term emission measurement curves	60
3.5.1	The angular intensity and YAG current evolution for a long-term operation.	60
3.5.2	The screen current and the central angular intensity for long term.	61
3.5.3	The profiles of emission patterns for the long-term run	62
3.6	Facet shape comparison for before and after long-term running	63
3.7	Conclusions	63

4	Multi-beam source experiment on individual beam characteristics	65
4.1	Introduction	65
4.2	Design of the experimental setup.	66
4.2.1	The MB source assembly in an Ultra-High Vacuum (UHV) vessel.	67
4.2.2	The characterization setup outside the vacuum vessel.	68
4.3	The embodiments of the MBS design (MEMS and conventional stacks).	69
4.3.1	The source with the MEMS stack.	69
4.3.2	HV insulation issue in the MEMS stack and attempted solutions	70
4.3.3	The source design with the conventional stack.	72
4.4	CCD image acquisition and knife-edge methods	73
4.4.1	50 Hz electromagnetic noise	76
4.5	Principles of the automatic measurement: LabVIEW software and post-process Python scripts	79
4.6	Measurement for the regular ALA	79
4.7	Measurement for the 4-quadrant ALA	82
4.7.1	Through focus series for 4-quadrant ALA	83
4.7.2	High magnification ($\times 20$) through focus series.	87
4.7.3	Beam current for all the four quadrants	90
4.7.4	Astigmatism manipulation with voltage settings.. . . .	92
4.8	Measurement for the large hexagonal patterned ALA.	95
4.9	Measurement for the decelerating lens mode.	97
4.10	Conclusions	102
5	Summary	103
6	Samenvatting	105
	Bibliography	109
	Acknowledgments	115
	Curriculum Vitæ	117

1

INTRODUCTION

1.1 OVERVIEW OF SEM APPLICATIONS IN THE SEMICONDUCTOR INDUSTRY

1.1.1 THE BASICS OF A SCANNING ELECTRON MICROSCOPE

The Scanning electron microscope (SEM) has been applied in many research fields all over the world. The SEM is superior to the optical microscope with respect to spatial resolution and a variety of analytical methods in many ways, like secondary electron (SE) imaging, back scattered electron (BSE) imaging, Voltage Contrast imaging, and the SEM usually has the energy-dispersive X-ray spectroscopy (EDX), which can be used to recognise the different elements in a specimen. The SEM can be used to investigate the physical, and electrical properties of a particular specimen, even a live integrated circuit with these methods. Therefore, an SEM is versatile for many kinds of research [1].

The electron-optical part of an SEM mainly consists of an electron source, condenser lens, scanning coils, objective lens, specimen stage, and detector system. The SEM can form a nanometers size electron probe on the specimen, and scanning coils will scan the probe over a specimen surface in a raster method. Because of the interaction between the electron probe and the specimen, secondary electrons will be emitted from the surface of the specimen and be collected by a detector. A computer unit will synchronize the scanning signal and the secondary electron signal acquired by the detector to generate an image.

However, the throughput of the SEM becomes a bottleneck nowadays in certain biological research and in the semiconductor industry because sometimes there is an enormous surface area to be inspected in these fields. Many efforts have been employed to improve the throughput and develop special variants of a conventional SEM. With the corresponding specialization, an SEM can check biological tissues or inspect wafer defects in much higher efficiency than before. Most efforts are concentrating on outputting more current from the source, in this thesis we will therefore specifically look at the source in the SEM for higher throughput applications. But first in the next sections, we will look in more detail at the purpose of SEM for large-scale inspection of semiconductor wafers.

1.1.2 SEM FOR METROLOGY AND INSPECTION IN THE SEMICONDUCTOR INDUSTRY

The SEM is not only used in academics, it also is a powerful tool to check the silicon wafers in today's technology because of its nanometer-scale resolution. When the dimensions of wafer features go below $0.1 \mu m$, it's difficult for optical microscopes to check the wafer. Furthermore, undesired short or open in the circuits could happen below the surface, which will cause the electrical failure, this can not be seen by an optical system inspecting the surface. Instead, these electrical defects can only be seen from the wafer surface with the illumination of electrons because the secondary electron image generated by an SEM is very sensitive to the electrical situation of the sample [2].

There are three applications of the SEM in the semiconductor industry, Critical Dimension (CD) measurement, wafer defect inspection, and defect review [3].

A. CD MEASUREMENT

The CD-SEM is a kind of dedicated equipment for measuring the dimensions of the fine patterns formed on a semiconductor wafer. The CD-SEM is mainly used in the manufacturing lines of electronic devices of semiconductors.

A CD-SEM differs from the general SEM in three ways:

1. The primary electron beam landing energy on a sample is $1 keV$ or below because lower landing energy reduces the charging of the wafer and reduces the damage.
2. The magnification of CD-SEM is calibrated to the maximum extend, so the measurement accuracy and repeatability are guaranteed.
3. CD-SEM does automatic measurements.

B. WAFER DEFECT INSPECTION

The wafer defect inspection system detects physical defects (usually particles) and pattern defects on wafers and obtains their position. Both laser and electron beam can be used as a probe to inspect the wafer.

Because the resolution of an optical microscope is limited by the wavelength and numerical aperture, it's difficult for a visible laser beam (like $523 nm$ laser) to image a feature below $100 nm$. Therefore, optical interferometry is used to provide nanoscale information by phase image [4].

An electron beam defect inspection system has some different features from a laser inspection system: The electron inspection system can have nanometer resolution like the conventional SEM, which makes it possible to detect nanometer-scale pattern defects directly in an image. Moreover, the electron beam inspection system detects the amount of the secondary electrons from the wafer since the SE yield is significantly influenced by the material conductivity, charging of the surface, and primary beam energy. An e-beam inspection system can also detect electrical defects, which is not possible for a laser tool [5].

Defects can be divided into random defects and systematic defects. E beam inspection system is often used to inspect systematic defects in the research and development department of a semiconductor factory. The systematic defects are mainly caused by the mask,

exposure process and have a huge influence on the yield rate of a newly developed chip. The disadvantage of the electron beam inspection system is its relatively low throughput, and the inspection time can take weeks for a whole 12-inch wafer scan. In the next section, we will talk about an option to improve the throughput of the electron beam inspection system, which is the multi-beam inspection.

C. DEFECT REVIEW

A defect review SEM is an electron beam instrument that will enlarge the defects with a high magnification so that it can review and classify them. The review SEM will load the inspected wafer and defect location information made by an inspection system, then take images of the defects and analyze them. Because the resolution of the inspection SEM is getting close to the review SEM, they may merge into one single kind of tool in the future.

1.1.3 MULTI-BEAM SYSTEM AS A HIGH THROUGHPUT SEM

As mentioned in section 1.1.1, a conventional SEM employs only **ONE** electron beam for imaging and usually is characterized by the probe size and beam current. In this section, we would like to talk about the probe size and the beam current in sequence, and we will talk about the multi-beam systems, which have much higher throughput than a conventional SEM in principle. We will compare the different configurations of multi-beam systems as well.

We take the electron beam diameter, which contains 50% of the total current as the probe size d_p . It is calculated with the Root Power Sum (RPS) method, which fits the full simulation better than the quadrature addition [6]. The minimum FW50 probe size at the image plane is:

$$d_p = \left(\left(d_I^{1.3} + (d_A^4 + d_s^4)^{1.3/4} \right)^{2/1.3} + d_c^2 \right)^{1/2} \quad (1.1)$$

where d_I , d_A , d_s , and d_c are FW50 diameter of the source image, diffraction, spherical aberration, and chromatic aberration at the image plane, respectively, they can be expressed as below:

$$d_I = M d_v \quad (1.2)$$

$$d_A = 0.54 \frac{\lambda}{\alpha} = 0.54 \frac{\Lambda}{V^{1/2}} \frac{1}{\alpha} \quad (1.3)$$

$$d_s = 0.18 C_s \alpha^3 \quad (1.4)$$

$$d_c = 0.6 C_c \frac{\delta U}{V} \alpha \quad (1.5)$$

where λ is the wavelength of the electron beam, M is the magnification on the sample plane, d_v is the virtual source size of the probe, α is the half aperture opening angle of the beam, $\Lambda = 1.226 \times 10^{-9} \cdot mV^{(1/2)}$, V is the beam potential at the sample, C_s is the spherical aberration coefficient, and C_c is the chromatic aberration coefficient, and δU is the FW50 energy spread of the electron source.

When we set an SEM with low beam landing energy and very low beam current mode, the image size and spherical aberration contributions are negligible, and can be ignored,

then the beam size is mainly determined by the chromatic aberration contribution and diffraction contribution. With equations 1.3 and 1.5, equation 1.1 can be written as below:

$$d_p = \left(\left(0.54 \frac{\Lambda}{V^{1/2}} \cdot \frac{1}{\alpha} \right)^2 + \left(0.6 C_c \frac{\delta U}{V} \alpha \right)^2 \right)^{\frac{1}{2}} \quad (1.6)$$

For an optimized α , this is

$$(d_p)_{min} = d_{AC} = 2.81 \times 10^{-5} \frac{C_c^{1/2} \delta U^{1/2}}{V^{3/4}} \quad \text{at} \quad \alpha = \sqrt{\frac{0.54 \Lambda V^{1/2}}{0.6 C_c \delta U}} \quad (1.7)$$

Thus, the probe size is only dependent on the energy spread and electron beam energy for a given electron microscope. Let's assume an SEM with a 2 mm chromatic aberration coefficient and 0.8 eV energy spread from the electron source. When the landing energy is set to 2000 eV, from equation 1.7, we know the minimum probe size is 3.8 nm, and the optimized half opening angle is 5.6 mrad. On the contrary, when we set the SEM with a relatively high beam landing energy (say > 15 keV) and very low beam current mode, the source image size is negligible as well, but the spherical aberration contribution is much greater than the chromatic aberration contribution, then the beam size is mainly determined by the spherical aberration contribution and diffraction contribution. With equations 1.3 and 1.4, equation 1.1 can be written as below.

$$d_p = \left(\left(0.54 \frac{\Lambda}{V^{1/2}} \cdot \frac{1}{\alpha} \right)^4 + (0.18 C_s \alpha^3)^4 \right)^{\frac{1}{4}} \quad (1.8)$$

For an optimized α , this is

$$(d_p)_{min} = d_{AS} = 1.03 \times 10^{-8} \frac{C_s^{1/4}}{V^{3/8}} \quad \text{at} \quad \alpha = 1.23 \left(\frac{\Lambda}{C_s V^{1/2}} \right)^{1/4} \quad (1.9)$$

Then, the probe size is only dependent on the spherical aberration coefficient and the electron beam landing energy for a given electron microscope. Let's assume an SEM with a 5 mm spherical aberration coefficient. When the landing energy is set to 20000 eV, from equation 1.9, we know the minimum probe size is 0.07 nm, and the optimized half opening angle is 7.9 mrad.

So far, we have briefly demonstrated how to achieve the minimum probe size with respect to the optical parameters of an SEM, and we mentioned two important modes,

- (a) **Low landing energy mode.** In this mode, the radiation damage will be minimized because of the low incident energy of the electrons. It's especially useful for biological tissues and wafers, which are very vulnerable to radiation damage. In this mode, the energy spread is a key factor to the probe size.
- (b) **High landing energy mode.** In this mode, the smallest probe size of an SEM will be achieved, and the spherical aberration coefficient becomes the key factor to the probe size. In both modes, the half opening angle of the electron beam is the independent variable and can be optimized for the smallest probe size, and the optimized value is 5.6 or 7.9 mrad for these two modes.

The throughput in SEM imaging is limited by the beam current at a desirable probe size. The beam current that can be obtained in an electron beam focusing system can be expressed as:

$$I_p = B_r \frac{\pi}{4} (Md_v)^2 \pi \alpha^2 V \quad (1.10)$$

where B_r is the reduced brightness of the electron source, and the definition will be explained in section 1.2.1. For example, for a Schottky source with reduced brightness of $1.0 \times 10^8 \text{ A}/(\text{m}^2 \cdot \text{sr} \cdot \text{V})$, the virtual source size is 25 nm , if we assume the magnification of an SEM is 0.04, the beam current I_p is about 15.3 pA for the low landing energy mode, beam current is 311 pA for the high landing energy mode for the optimized half beam opening angle. From equation 1.10, we can see the maximum beam current at a desirable resolution is limited by the brightness of a given electron source used in the SEM. The concept of multi-electron beam systems, which aims to improve throughput for a given source brightness and Coulomb interactions, was initially presented in the late 1960s. The various research on multi-beam systems all over the world can be divided into 4 categories.

1. multi-axis systems [7].
2. multi-source, single column systems [8].
3. single source, single column system [9][10].
4. single source, multi-column systems [11][12].

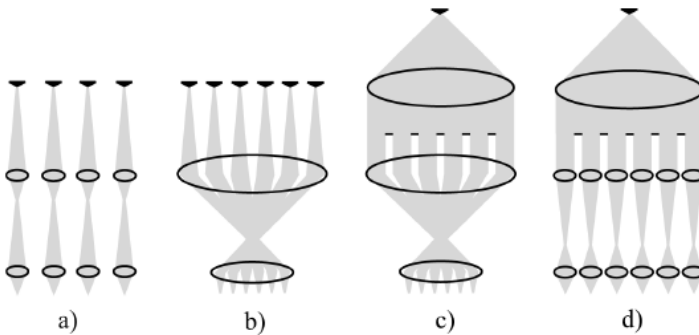


Figure 1.1: a. multi-axis system, b. multi-source, single column system, c. single source, single column system, d. single source, multi-column system. (Figure reproduced with permission from [13])

The first and second concepts have the challenge of fabricating identical and stable emitter arrays. The third concept doesn't need an emitter array. Instead, it generates multi-beams with a well-developed thermionic source or Schottky source and beam splitter. This configuration has been successfully used for EBID (electron beam introduced deposition) [14] and transmission imaging [15] - [16]. With a second column to focus and separate the secondary electron signal to a multi-detector array, this configuration can also be used for SE imaging [17][18]. But the third concept has two disadvantages (a) there is a crossover of all the beams above the objective lens, which will limit the total current that the system

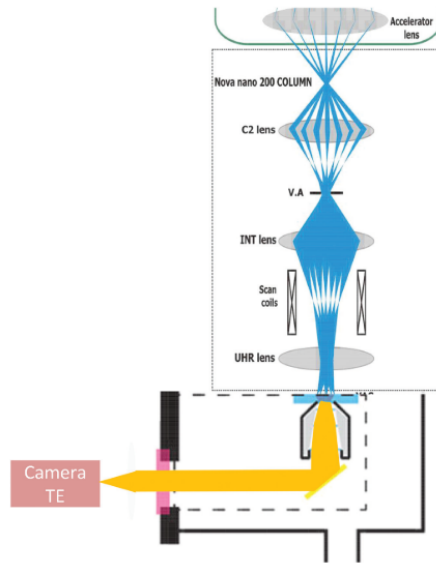


Figure 1.2: Combination of Delft MBSEM1 and SECOM platform. (Figure reproduced with permission from [19])

can deliver because of the stochastic Coulomb interactions, which increase the probe size. (b) off-axial beams will suffer from off-axial aberrations in the column, which will limit the number of the total beams and the spot size. Some efforts are needed to compensate for the off-axial aberration. To overcome these two disadvantages of concept 3, a single source with a multi-column system was proposed. An example of this is the MAPPER system [11][12], which is dedicated to high throughput maskless lithography. This single-source, multi-column system can avoid the off-axial issues and Coulomb interactions in the objective since every beamlet has its own column. With proper design, it has the potential to do SE imaging and can be used as a wafer inspection tool. We will show more analysis in the following chapters.

1.2 CHALLENGES OF THE SCHOTTKY SOURCE USED IN A MULTI-BEAM SOURCE

1.2.1 ELECTRON SOURCES USED IN THE SEM AND LITHOGRAPHY

We will explain the brightness and energy spread in this section first. Different kinds of electron sources will be discussed afterwards. There are many parameters of an electron source, as we will explain in more detail in section 1.2.2. Brightness and energy spread are the most important SEM characteristics for a low beam landing energy, high throughput application, for example, a multi-beam SEM aimed at biological sample or wafer inspection. We may also mention other parameters in this section.

BRIGHTNESS

For modern electron-optical instruments, like electron microscope and its variants, one small beam size (nanometer scale) formed by a lens system is always desired, and in the meantime, more beam current is wanted for a better signal-noise ratio in the detection. A small beam opening angle is usually taken to limit the aberrations, like spherical aberration and chromatic aberrations. Therefore, we want the electron source to have a large current density, and this current density distributed in a small opening angle. To describe this performance of an electron source, the parameter ‘brightness’ is used. The differential brightness of an electron beam is defined as:

$$B_{diff} = \frac{dI}{dAd\Omega} \quad (1.11)$$

where dI is the current passing through a surface dA within a solid angle $d\Omega$. When an aperture is inserted in the beam, either the area or the angle is lowered, but the current is proportionally reduced, so the brightness remains constant. However, the differential brightness will not keep constant in the acceleration or deceleration, which occurs inevitably in an electron optical system, because the beam angle changes in these situations, it will decrease with acceleration and increase with deceleration. The problem is solved by defining a reduced brightness of the beam as

$$B_r = \frac{dI}{dAd\Omega \cdot V} \quad (1.12)$$

Because the reduced brightness is constant in the whole system, it can also be used as a parameter of the source. A current distribution with the largest density in the center and often long tails can be seen in a source image. Although this is not a formal definition, a frequently used concept is practical brightness $B = I/A \cdot \Omega$, which necessitates defining the size of the source image. The definition of the full width that contains 50% of the current: FW50 is recommended. Then, the practical brightness is slightly larger than the differential brightness [20]:

$$B_{pract} = \frac{I}{\frac{\pi}{4} d_{FW50}^2 \pi \alpha^2} = 1.44 B_{diff} \quad (1.13)$$

ENERGY SPREAD

Besides the brightness, the other important parameter is energy spread. The energy spread of an electron beam will enlarge the focused beam size, and the contribution to the spot size can be written as equation 1.5. From the electron emission theory, the tangential energy (energy perpendicular to the emitter axis) distribution of the electron current density can be found by integrating the product of the Fermi-Dirac distribution and the transmission probability over normal energy (energy along the emitter axis) [21].

$$j(E_{tan}) dE_{tan} = \frac{me}{2\pi^2 \left(\frac{h}{2\pi}\right)^3} dE_{tan} \int_0^\infty \frac{D(W)}{1 + \exp\left(\frac{E_{tan} + W - E_F}{kT}\right)} dW \quad (1.14)$$

E_{tan} is the tangent energy of an electron, W is the normal energy of the electron, m is the mass of the electron, e is the charge of the electron, h is Planck’s constant, E_F is the Fermi level, k is Boltzmann constant, T is the temperature in *Kelvin*, $D(W)$ is the transmission

function with respect to the normal energy.

With equation 1.14, we can plot the probability of current density according to the tangent energy and normal energy in figure 1.3.

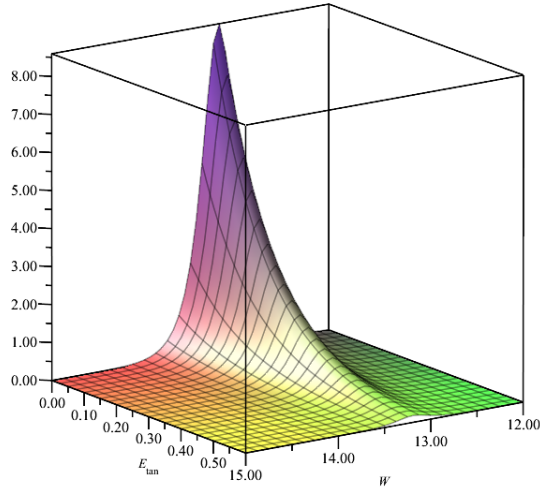


Figure 1.3: The tangent and normal energy distribution of electrons emitted by a surface at 1800 K, with a work function of 2.93 eV, calculated from equation 1.14.

1.2.2 DIFFERENT ELECTRON SOURCES

In electron optics, the research of electron sources is an important task. The performance of electron microscopes and electron beam lithography machines depends critically on the quality of the electron source used in the instrument. The main function of the electron source is to provide a bright electron beam with low energy spread in SEMs or e-beam lithography machines. Therefore, the brightness and energy spread are more vital characteristics than the total emission current and other parameters [22].

Table 1.1 shows several popular kinds of electron sources and their performance in the electron microscope and electron beam lithography machines. The thermionic emission type cathodes, like tungsten hairpin and lanthanum hexaboride (LaB_6), dominated the electron source applications in the past. BaO cathode is also a kind of thermionic emitter and was used in the cathode ray tube (CRT) system in the past, like old-fashion televisions or other display equipment. It became a good alternative source for a multi-beam electron lithography system because of its high brightness and total beam current. The cold field emission source and Schottky source (thermal assisted field emission source) have been available for some time, and the field emission technology is commonly used in a wide variety of both laboratory type and process type electron beam systems, especially at the low accelerating voltages needed for nondestructive inspections, like biological sample imaging and semiconductor inspection.

Thermionic emission sources are the simplest type and are still used widely. Some electrons

Table 1.1: Comparison of several electron source characteristics [1][22][23][24].

	Unit	BaO	Tungsten Hairpin	LaB_6	TF emitter	CF emitter
Reduced Brightness	$A/(m^2 srV)$	10^6	10^5	10^6	10^8	10^9
Virtual source size	nm	$> 10^4$	$> 10^4$	$> 10^3$	25	5
Energy spread	eV	–	3	1.5	0.7	0.3
Short-term beam current stability	%RMS	1	1	1	1	4–6
Work temperature	K	1300	2600	1800	1800	300
Work function	eV	2.1	4.5	2.6	2.8	4.5
Vacuum	Pa	10^{-6}	10^{-4}	10^{-6}	10^{-8}	10^{-11}
Typical life	$Hour$	5000	40	1000	5000	2000

gain so much kinetic energy by heating that they can overcome the potential barrier at the cathode surface. An electric field generated by a positive anode will accelerate the electrons which already leave the surface. Tungsten hairpin and LaB_6 are two popular kinds of thermionic sources. Their advantages are low cost and easy maintenance, and low working vacuum pressure also lowers the cost of the vacuum system. The disadvantages are low brightness, high energy spread, and shorter lifetime compared to the Schottky source.

In a Schottky source (also called thermal field emission source or TFE source), electrons at the barrier energy level will go through the potential barrier either because of the tunnel effect or because of their kinetic energy. An electric field at the magnitude of $1 V/nm$ can lower the potential barrier and make it thinner. Even electrons with an energy level below the barrier have some probability to tunnel through the barrier and get out of the cathode surface. ZrO/W emitter is the most popular kind of Schottky source. The advantages of a Schottky source are its high brightness, small virtual source size, and long lifetime. The reduced brightness of the ZrO/W emitter is about $2.0 \times 10^8 A/(m^2 srV)$, which is 2 or 3 orders of magnitude higher than a thermionic source. A Schottky source can have a stable emission for more than 1 year. The disadvantage of the ZrO/W emitter is that it needs an ultra-high vacuum.

A cold field emission source (CFE source) works in an even stronger electric field than a TFE source, but at room temperature. The emitter is not heated, and the electrons at the Fermi energy level will tunnel through the potential barrier by a high electric field. The advantages of the CFE source are the small energy spread and high brightness, as shown in table 1.1. The disadvantages of a CFE source are that it needs an even better ultra-high vacuum and a less stable emission current than a TFE source. A CFE source usually delivers less beam current and needs regular flushes.

Considering brightness, energy spread and some practical aspects, like maintenance, we

conclude that the Schottky source is the best candidate for a multi-beam electron microscope application. More theoretical and experimental investigations of a Schottky source will be elaborated on in chapter 2 and chapter 3, respectively, to explore the extreme performance of a ZrO/W type Schottky source.

1.2.3 THE EMISSION THEORY AND OPTIC THEORY OF THE SCHOTTKY SOURCE

As shown in figure 1.4, the high electric field lowers the potential barrier and reduces the barrier width in a Schottky source, and the consequence is that the emission current is enhanced concerning the thermionic emission. The surface current density J_s for the Schottky source is determined by the work function ϕ , temperature T , and the electric field F by the Schottky equation [25]:

$$j_s = \frac{4\pi m e}{h^3} (kT)^2 \exp\left(\frac{-\phi - \sqrt{\frac{e^3 F}{4\pi\epsilon_0}}}{kT}\right) \quad (1.15)$$

The Schottky equation describes the effect of lowering the potential barrier in figure 1.4, by the term $\Delta\phi_s = e^{3/2} F^{1/2} / (4\pi\epsilon_0)^{1/2}$. Usually, the Schottky emitter operates in the ‘extended

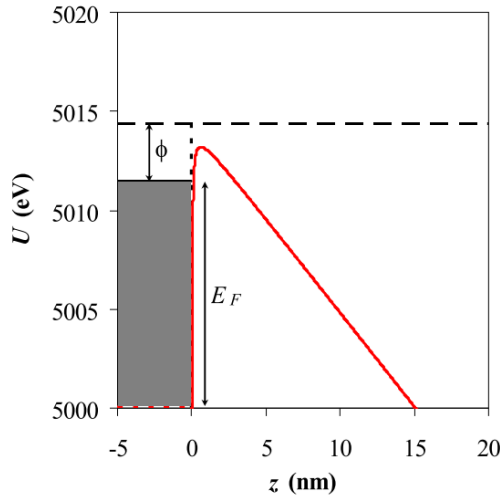


Figure 1.4: The analytical description of the potential energy barrier near the surface of a perfectly conducting semi-infinite metal for a field strength of 0.95 V/nm. (Figure reproduced with permission from[21])

Schottky regime’, where the tunnelling current cannot be neglected. A measure of the tunnelling current is given by the dimensionless parameter q . For $0.15 < q < 0.7$, the current density can be approximated by

$$J_{ES} = J_s \cdot \frac{\pi q}{\sin(\pi q)} \quad (1.16)$$

With $q = \frac{h(4\pi\epsilon_0 e)^{1/4}}{2\pi^2 m^{1/2}}$.

The angular current density is related to the cathode surface current density by the launch position r at the facet and the beam angle α after the extractor [21].

$$I' = \left(\frac{r}{\alpha}\right)^2 j \quad (1.17)$$

where r is the distance between the launch position and the optical axis, α the final ray angle of the launched electron in the field-free zone behind the extractor. With equation 1.17, one can construct the emission pattern of the full facet with simulated electron trajectories (figure 1.5).

Besides some theoretical research done with the off-axis electron beam, some numerical

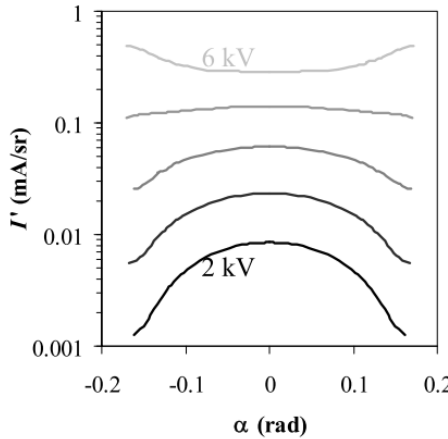


Figure 1.5: The angular intensity according to different extraction voltages. Figure is reproduced with permission from [21].

simulations of the off-axis electron beam have also been done [26]. The authors developed a computer program modelling program, which can calculate many key performance measures of a Schottky source. The work function ϕ , field factor β , and the source brightness B_r can be calculated from the on- and off-axis experimental angular intensity I' data. The energy spread ΔE_{50} and angular intensity I' are directly measured for the off-axis emission up to 4° (69.8 mrad).

Because of the dramatic distribution, the electric field in a Schottky source cannot be represented by an expansion of the axial field, as is usually done for lens systems in electron optics. The familiar paraxial assumptions and aberration theory for characterizing lenses are not applicable, neither. However, researchers still attempt to apply the familiar optical concepts to an electron source. One of the approaches is called Canonical Mapping Transformation [27]. In the CMT method, Fujita & Shimoyama defined the focal length, The definition of the electron gun focal length by normal electron rays. With the assumption that the source can be taken as a lens system and made the CMT, the spherical aberration can be extracted from the CMT. It has been shown that the CMT can be characterized by a

small number of optical parameters. Therefore an electron source can be characterized by only several parameters.

1.2.4 CHALLENGES FOR THE OFF-AXIAL BEAMS IN A SCHOTTKY SOURCE

From literature mentioned above, several aspects for the off-axial beams in a Schottky source are not clear and need to be addressed if we want to design a Multi-Beam Source based on a Schottky source.

First, the stability of whole uniform emission range need to be checked in an experiment. The stability of the central electron beams of a Schottky source is thoroughly tested and understood, nevertheless, it's not clear how the emission at the other area evolves, what operation conditions are needed to maintain a stable uniform emission over a certain polar angle, which is essential for a multi-beam source.

Secondly, performance difference between the central beams and off-axial beams is critical for the uniformity of beamlets in a multi-beam source. For instance, the angular intensity difference between an off-axial beam and a central beam will cause beam current difference between these two beamlets, assuming the identical apertures are used to separate the beam. The virtual source size difference between an off-axial beam and a central beam will cause the different spot size for these two beams.

To address the first challenge, one experiment was conducted to test the long-term stability of the whole emission pattern of an Schottky source. The related content will be elaborated in Chapter 3.

To address the second challenge, we will use CPO2D software[28] to calculate the field distribution in a Schottky source, then simulate the electron trajectories from the face till the field-free area after the extractor. The transfer matrix from the facet plane to the virtual source plane will be determined by the MATLAB manuscript using the least square root method. With the transfer matrix, more detailed performances of a source can be explored, like virtual source sizes, virtual source positions, aberrations for the on- and off-axis electron beams. The influence of the dramatic field distribution between the emitter and extractor, which was neglected in the multi-beam source research, will be explored.

1.3 PRACTICAL CHALLENGES IN MANUFACTURING A MULTI-BEAM SOURCE

After the design of an electron gun, the next phase should be manufacturing and assembling it, and some practical challenges will appear in the experiments. A design of the Multi-Beam Source used in Delft MB-SEM was mentioned in literature [29]. This design combines an SE source, and Aperture Lens Array (ALA), and E1 & E2 electrodes between the SE source and ALA. With dedicated E1 and E2 geometry and voltage settings, the MBS can generate focused beams at the image plane, also minimize the aberrations of the source, which can be proved by the simulation. However, the simulation is based on the assumption that we have perfectly aligned elements, and all these elements have perfect geometry, like round apertures. Real conditions deviate from the 'perfect' condition somehow. Any machining and assembling will generate errors to some extent, which are called tolerance in engineering. Either a tolerance analysis or an experiment setup can

verify the performance of a MBG with some tolerance, we made an experiment setup to do so in this thesis.

Another particular issue for the multi-beam source in Delft is the high voltage insulation

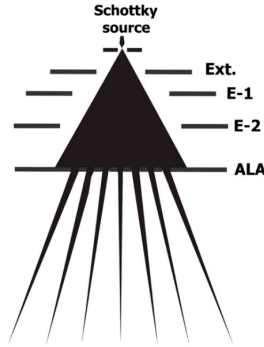


Figure 1.6: Schematic drawing of the multibeam source used in the MBSEM to produce an array of focused beams.

for a MEMS-based assembly, like a source assembly or an objective assembly. An electron optical column based on MEMS technology can be significantly more compact and repeatable as compared to the conventional column [11]. Nevertheless, this scale-down also brings the challenge of high voltage insulation in the vacuum. The surface flashover is begun by the electron emission from the cathode triple junction (CTJ), and the CTJ is the junction of the insulator, cathode, and vacuum [30]. When the emitted electrons hit the insulator surface, more secondary electrons will be emitted by the incident electrons. Those secondary electrons will stimulate more electrons if they impact the surface again by the electric field. The chain action will generate quite some current on the anode electrode eventually. This process is called a secondary electron emission avalanche (SEEA) [31]. SEEA can be affected by the insulator shape. Therefore, many kinds of insulator shapes have been reviewed and tested experimentally in the past decades. The scale is usually at about 10 mm, and the insulator material is usually ceramic. But the situation can be different for 1 mm scale and for glass insulation, which is the dimensions and material used in MEMS-based electron optical columns.

1.4 SCOPE OF THE THESIS

This thesis was trying to address the possibility and performance of a Schottky emitter in a multi-beam inspection application. Both theoretical work and experimental work were carried out in this thesis.

Chapter 1 mainly explains some backgrounds of this thesis. Some basics of SEM applications in the semiconductor industry are explained in section 1.2. the theory and challenges for the Schottky source in a multi-beam source are explained in section 1.2. The practical challenges are briefly explained in section 1.3. Section 1.4 explains the scope of the thesis. Chapter 2 elaborates on the extended Schottky emission theory and aberration coefficient extraction from the trajectories. With the software CPO2D, we simulated some trajectories from facet to the plane in the field-free area for both a 0.5 μm radius emitter and a 1.0 μm

radius emitter. The virtual source property is analyzed and aberrations of the off-axial beams are retrieved.

Chapter 3 presents the experimental results of an R1.0 Schottky emitter characterization setup. We aimed to achieve 1.0 mA/sr angular intensity for this radius $1.0 \text{ }\mu\text{m}$ emitter, we found the beam current could be reasonably stable for the whole emitting facet at 0.81 mA/sr angular intensity.

Chapter 4 explains the experimental work of manufacturing a multi-beam source with $0.5 \text{ }\mu\text{m}$ emitter, which can deliver a few hundred beamlets. The spot size and beam current in the image plane at $z = 300 \text{ mm}$ were measured, they are reasonably uniform. The octupole effect for the square-patterned aperture lens array (ALA) was observed, and shaped apertures were used to compensate for the octupole effect. Astigmatism was also observed.

Chapter 5 summarizes the main innovations and conclusions of the work. And Chapter 6 is a Dutch version of the chapter 5.

2

ELECTRON OPTICS THEORY OF THE OFF-AXIAL ELECTRON BEAMS IN A SCHOTTKY SOURCE

2.1 INTRODUCTION

In a multi-electron beam system, off-axial electron beams are of special interest. The axial property of the emission of a Schottky source has been investigated extensively for many decades [32][33][34][35]. The SE source is used widely in many electron optical systems nowadays because of its high brightness, low energy spread, and long-term emission stability. However, most of these apparatuses only use the axial electron beams within a very small half-opening angle. Considering the total emission angle of an SE source of more than 200 mrad , it will increase the efficiency significantly if the off-axial electrons could also be used. For the application of a certain monochromator type [36], which uses lens dispersion on the off-axial beam, the performance of the off-axial electrons is also of interest. We shall first discuss what is known about the off-axis emission properties, then conclude that what is missing is a good model for the virtual source size of off-axial beams, and then try to complement the existing body of knowledge through careful trajectory simulations.

As shown in figure 2.1, three different angular current distributions for three different extractor voltages were measured for a $1.0\text{ }\mu\text{m}$ radius SE emitter: the shape of the distribution is convex for a lower extractor voltage of 2900 V , flat for the medium extractor of 3700 V , concave for the higher extractor voltage of 4600 V , respectively. There are two effects playing a role in this: One is that the electric field increases with the distance from the center of the facet, which causes the current density to be higher near the edge than it is at the center. The second is the lens effect of the emitter system which will broaden the solid angle more for the electrons from the area near the edge than electrons from the central area. This effect will reduce the angular intensity of the outer beams. At high fields, the emission distribution is very concave, and the lens effect cannot compensate for this. At lower fields, the lens effect can make the angular distribution convex. When the lens effect

exactly compensates for the emission non-uniformity, the angular distribution after the extractor will be flat up to a certain angle. For a multi-beam source, it is essential to have an equal beam current for every beamlet, so the flat emission is preferable, and the lens effect in a Schottky emitter is of significant interest.

In order to find the lens effects, one would usually take the axial field and then use well-

2

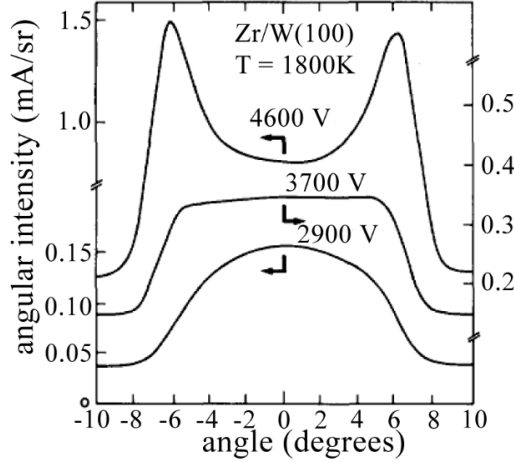


Figure 2.1: Measured angular current density for different extractor voltage. the graph is cited from [13], which is replotted from [35].

known integrals to find the lens properties, but the field distribution inside the electron gun is not suitable for the representation by axial field expansion, because the field at the cathode changes dramatically with the distance to the center. Moreover, the angle between the ray and the axis may be too large for the usual approximations. Therefore, the paraxial equations and aberration theory that characterize a lens system are not applicable, and retrieving the aberrations from real ray tracing is preferable. One attempt was made by Fujita and his colleague [27]. They modified the conventional approach and made it possible to evaluate an electron source with only a few parameters. Another approach, which is based on the modified temporal theory used to study mirrors, has been published by Rose [37]. We will explain only Fujita's theory because of its similarity to our work. Fujita and Shimoyama [27] proposed the canonical mapping transformation (CMT) method to characterize the property of a thermionic electron source with a small number of optical parameters, and afterward, they also applied the CMT theory to the Schottky source [38]. In the CMT method, the electron gun focal length f is like the paraxial approximation theory and relates the electron trajectory slope after the extractor to the original position of the trajectory at the emitter surface. The crossover size and the angular current intensity can be described by the electron gun focal length f and the spherical aberration coefficient of the lens system formed by the emitter, grid, and extractor.

$$\frac{1}{f} = - \left. \frac{\partial \sin \beta}{\partial \xi} \right|_{u=0, \xi \rightarrow 0} \quad (2.1)$$

$$x_c(\xi) = -C_s(\xi/f)^3 \cong C_s \sin^3 \beta \quad (2.2)$$

$$I' = f^2 j_s \quad (2.3)$$

where β is the slope angle of an electron trajectory at the field-free area after the extractor, ξ is the original position at the emitter surface of an electron trajectory, $x_c(\xi)$ is the intercept in the crossover plane, over the position on the facet, and C_s is the spherical aberration coefficient, I' is the angular current density at the field-free area after the extractor, j_s is the emitter current density.

Liu and Schwind et al. [39] carried out a study to explore the operating conditions under

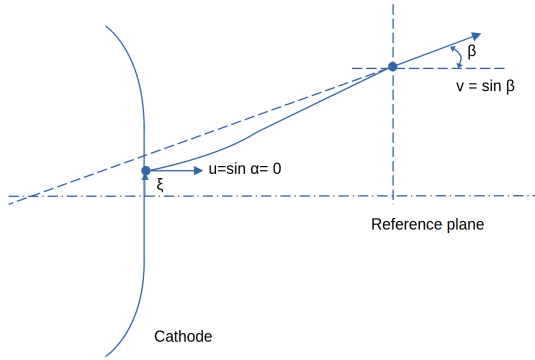


Figure 2.2: The definition of the electron gun focal length by normal electron rays, figure is replotted from [38].

which the emitter can end up with 3 end form shapes [40][41], and found a correlation between work function and electric field, which can explain the shape change of the emitter, they also measured the angular intensity, and it showed that different end shapes of the emitter have not only different magnitudes of angular intensity at the center, but also different polar angle ranges. They also measured the energy spread for off-axis electron beams in another paper [42]. Kellogg described a hybrid experimental and numerical method, which can determine many parameters simultaneously for both on-axis and off-axis electrons beams [26]. Nevertheless, virtual source shape and size on different directions and aberration coefficients for the off-axial beams were not touched in the research, and will be done in this chapter.

$$I'(\beta) = \left(\frac{\partial r}{\partial \sin \beta} \right)^2 j_s(\xi) \quad (2.4)$$

Bronsgeest pointed out that the lens effect not only influences the angular intensity distribution in the field-free area after the extractor (equation 2.4), but it also influences the virtual source size of different beamlets launched from different positions on the facet. To a first-order approximation, Bronsgeest assumed that the field strength on the relevant facet

area equals that at the launch position of the cold electrons in the beamlet. The virtual source size (FW50) of an off-axis beamlet can then be found from the equation:

$$d_v = 1.67 \frac{dr}{d\alpha} \sqrt{\frac{kT}{eV_{ext}}} \quad (2.5)$$

An example is given in figure 2.3. As can be seen, for this approximation, the virtual source size goes to zero for the outermost beamlets (see: $dr/d\alpha \rightarrow 0$), associated with emission near the facet edge. We shall re-examine these conclusions and find different results. The intermediate conclusions from the literature are: It is possible to create a fairly

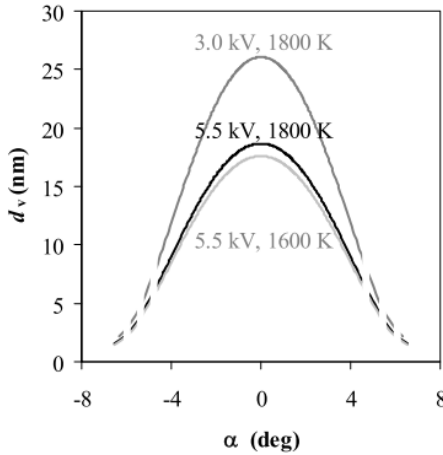


Figure 2.3: Virtual source size as a function of the angle of the beamlet in the field free zone [21].

uniform angular current density distribution, which seemed a good requirement for using a Schottky emitter as an electron source for multi-beam systems. However, there are three problems with this:

1. To get a uniform angular emission pattern, the emitter might not be operated at the maximum possible angular intensity or maximum brightness.
2. The virtual source size at the edges of the beam array may be much smaller, resulting in different spot size characteristics in the multi-beam system.
3. The electrons from different areas on the facet will go through some different off-axial paths, where the field is inhomogeneous, to the field-free zone after the extractor, and these electrons will pick up off-axial aberrations, like astigmatism, coma, distortion, and field curvature.

The third problem has had very little attention in the literature. Therefore, more research on the off-axial electron beams is necessary for multi-electron-beam systems.

In this paper, the properties of off-axial electron beams will be investigated. In an SE source, the size of the functional area is about 1 mm. However, the radius of the emitter end is

between 0.5 and 3 μm . Because of this multi-scale feature of the SE source, the Boundary Element Method (BEM) is preferable for the field calculation, and we chose electron optics simulation software CPO2D [43], which is a dedicated electron optics design software provided by Electron optics company. CPO2D is also employed for the 2-dimensional or 3-dimensional electron trajectory calculations. MATLAB scripts are also made to analyse the rays and extract the transfer matrix between the aberration-free rays and aberrated rays. Based on the transfer matrix, more information can be extracted.

2.2 PRINCIPLE OF CPO2D AND SCHOTTKY EMISSION MODEL IN IT.

The CPO2D and CPO3D use the Boundary Element Method (BEM) to find electrostatic potentials and fields for systems of conducting electrodes. CPO2D is designed to deal with systems that have axial or planar symmetry, and CPO3D will deal with systems of more general symmetry or no symmetry at all. In both cases, use can be made of any planes of reflection symmetry that might exist. The Boundary Element Method is sometimes referred to as the Surface Charge Method or the Integral Equation Method. The first systematic lens data analysis with BEM was made by Dr. Read, Manchester group, in 1971 [44]¹. The principle of the BEM is based on the fact that in a system of conducting electrodes, real free charges appear on the surfaces of the electrodes when potentials are applied to them. These surface charges are the sources of all the potentials and fields in the system. Therefore, the electrodes are replaced by these charges in the BEM. The surface charges are deduced from the potentials applied to a set of electrodes. The only parts of the system that the user must specify are the surfaces of the electrodes and the corresponding voltages on the electrodes [43].

In the CPO2D programs, the surfaces are divided into basic segments. Figure 2.4 shows that cylinders are divided into circular hoops in CPO2D.

The surface charge density on each segment is taken to be uniformly distributed over its surface on the assumption that the segments have been chosen to be sufficiently small. With a given set of charges q_i the potentials V_i can be calculated by Coulomb's Law. In more detail, the relation between the potentials and charges is written through the linear equation.

$$V_j = \sum_{i=1}^n q_i P_i(\mathbf{r}_j) \quad (2.6)$$

where r_j is the mid-point position of segment j , and $P_i(\mathbf{r}_j)$ is the potential at \mathbf{r}_j due to a unit charge on segment i . In other words, the potential V_j of segment j is due to the charges q_i on all the segments i , including the self potential due to the charge q_j on the segment j itself. Clearly the coefficients $P_i(\mathbf{r}_j)$ can be calculated, essentially by using Coulomb's Law and averaging over the areas of the segments. There are n of these equations, for $j = 1$ to n . Since the user defines the voltages of the electrode surfaces, V_j is known. There are only n unknown variables, q_i , for $i = 1$ to n . Therefore, the surface charge q_i can be solved for the n equations. The electrostatic simulation is then completely solved. The system of electrodes has become a set of segments each of which carries a known charge uniformly

¹ It is interesting to note that for the support of my work with CPO2D, I had personal contact with professor Read who returned to his old hobby after a very successful career in atomic and molecular physics.

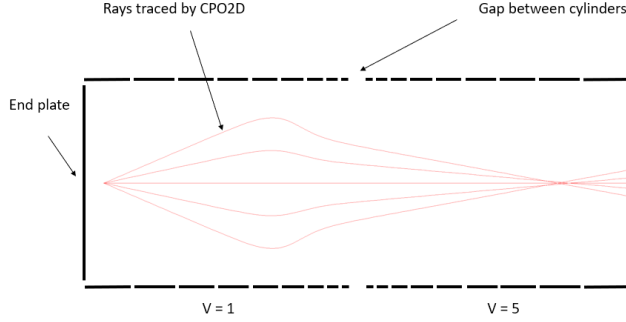


Figure 2.4: A schematic view of a double cylinder lens in CPO2D, this graph is from the user guide of CPO2D program.

distributed over its surface. Potentials and fields can now be calculated anywhere in space, again essentially by using Coulomb's Law. Comparing to the very popular FEM (Finite Element Method), the BEM has several advantages [45]:

1. Artificial mesh or points in the space enclosed by the electrodes are not necessary. Therefore, the matrices to be solved are much smaller than those in the FEM. This will save calculation resources and time consumption.
2. Another feature is that the system can be unbounded in the BEM calculation.
3. The BEM has no restrictions on the relative size of the electrodes.
4. During ray tracing, the field at each point is calculated directly from the surface charges and not through an approximate interpolation between mesh points.

2.3 THE EXTENDED SCHOTTKY EMISSION THEORY

The emission theory of the extended Schottky source is complex, and we only cite several conclusions from the literature in this section.

The cathode current density J_s for the Schottky emission regime is related to the work function ϕ , temperature T , and electric field F by the Schottky equation [46]:

$$J_s = \frac{4\pi m_e (kT)^2}{h^3} \exp\left(\frac{e^{3/2} F^{1/2}}{(4\pi\epsilon_0)^{1/2} kT} - \frac{\phi}{kT}\right) \quad (2.7)$$

A measure of the tunnelling current is given by the dimensionless parameter q , where

$$q = \frac{h(4\pi\epsilon_0 e)^{1/4} F^{3/4}}{2\pi^2 m_e^{1/2} kT} = 1.656 \times 10^{-4} \frac{F^{3/4}}{T} \quad (2.8)$$

And F is in V/m , T is in *Kelvin*. For example, when $q = 0.5$, approximately half of the current is due to tunnelling. When q is small, the emission characteristics are adequately

described by equation 2.7, with only a small fraction of current due to tunnelling. For higher values of q , the emission is in the extended Schottky regime, and the current density J_{ES} can be approximately described by the following equation:

$$J_{ES} = J_S \frac{\pi q}{\sin(\pi q)} \quad (2.9)$$

The practical brightness of thermionic and SE sources, expressed in properties on the surface [20]:

$$B_r = 1.44 \frac{eJ_{ES}}{\pi kT} \quad (2.10)$$

The practical reduced brightness B_r can also be expressed in properties of the beam further away from the emitter surface:

$$B_r = \frac{4I'}{\pi d_v^2 V_E} \quad (2.11)$$

Where d_v is the FW50 diameter of the virtual source, as seen from the plane in which I' is measured. FW50 diameter is the diameter of the disc that contains 50% of the total current. Then, we can also deduct the formula of angular current density I' related to the reduced brightness B_r ,

$$I' = B_r V_E \frac{d_v^2 \pi}{4} \quad (2.12)$$

2.4 ABERRATION COEFFICIENT CALCULATION FROM ELECTRON TRAJECTORIES

2.4.1 GEOMETRIC ABERRATION FOR THE OFF-AXIAL BEAMS

Based on the paraxial approximation, the geometrical performance of an electrostatic or magnetic lens can be characterized with Gaussian optical parameters and aberrations up to certain orders of the term for the aperture angle or the object position, or their combinations, and aberrations are deviations from the Gaussian optics. Gaussian optical parameters, like focal length, object distance, image distance, and magnification, can characterize the linear behaviour of a lens system according to the opening angle and object position. On the contrary, aberration coefficients describe the non-linear part with respect to the opening angle and object position of the lens system.

A conventional and popular approach to calculate the aberration coefficients is aberration integration. In this method, the axial field distribution and its derivatives to a certain order are needed for the aberration coefficient integrals. Some prevalent electron optics software can determine lens aberration coefficients by computing aberration integrals.

Scherle's paper [47] described a fitting method in particle optics. It describes a computer-based calculation of various paths in a beam as well as data fitting, both of which are utilized for beam shape analysis and optimization. Kasper [48] explained the use of least squares fitting for determining aberration coefficients. Van der Stam and Kruit [49] presented a more generic framework for particle tracing and coefficient fitting. Then, it took a long time to precisely compute many trajectories using ray tracing, which is why this method was not frequently utilized for calculating aberration coefficients. It is now possible to obtain tens of thousands of precise trajectories on a PC in a few minutes. Therefore, Oral

and Lencova [50] proposed a method with procedures for the calculation of aberration coefficients using ray tracing.

For this approach, we need accurate field calculation and trajectory calculation. We made some models in CPO2D for a Schottky source, shown in figure 2.5 and figure 2.6. The model a is based on figure 3.1 in Bronsgeest's thesis, which is based on an SEM image of a real emitter.

2

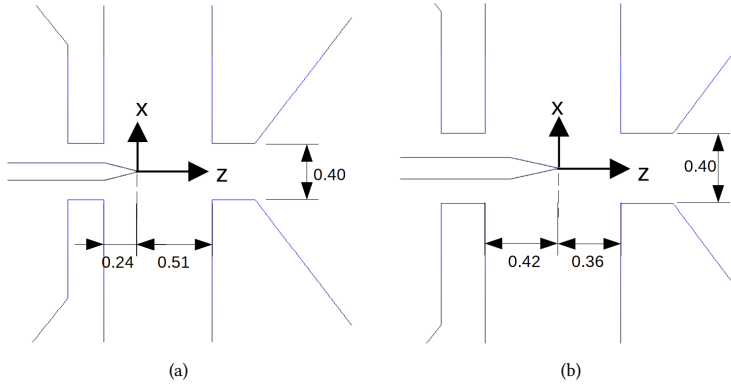


Figure 2.5: Geometries of two Schottky emitters. (a), radius $0.5 \mu\text{m}$ emitter, (b), radius $1.0 \mu\text{m}$ emitter. The diameter of the suppressor and extractor are both 0.4 mm , and the distances between the facet and the extractor surface are 0.5 mm for case a, and 0.36 mm for case b, the distance between the suppressor surface and the extractor surface are both about 0.75 mm .

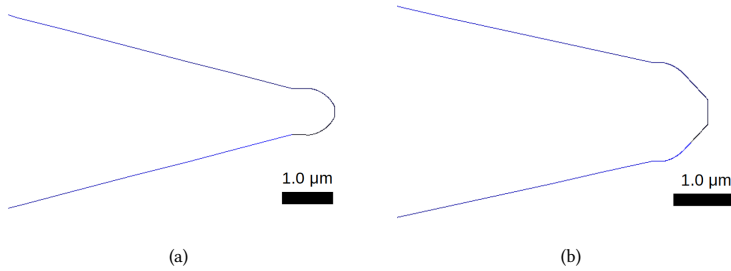


Figure 2.6: The end shape of two emitters. (a), radius $0.5 \mu\text{m}$ emitter, (b), radius $1.0 \mu\text{m}$ emitter

We want to compare the performance of a radius $0.5 \mu\text{m}$ emitter and a radius $1.0 \mu\text{m}$ emitter at 5 kV extraction voltage. We also would like to investigate the performance of 6 kV extraction voltage on the radius $1.0 \mu\text{m}$ emitter for higher emission. The suppressor voltage is set to -480 V so we can keep the field at the facet the same as in case b. From now on, we will name cases a, b, and c for different simulation results. Figure 2.6 shows the shape of two emitters, the left one is taken from the Bronsgeest's thesis [21], and the right one for the $1.0 \mu\text{m}$ radius is taken from an SEM photo of the emitter used in our experiment, which will be mentioned in Chapter 3. We did the simulations for 3 cases,

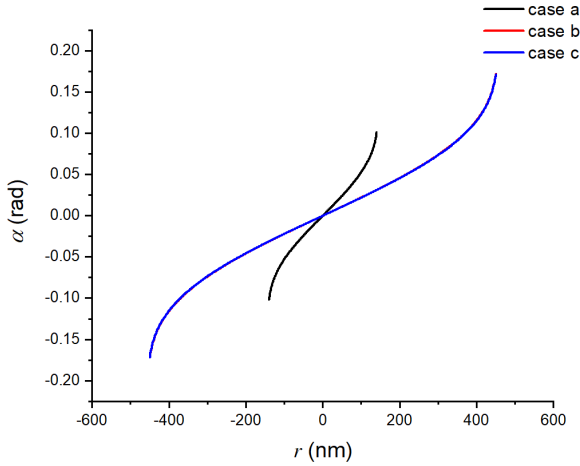


Figure 2.7: The relationship between electron positions at the facet and polar angle in the field free area ($z = 1.5$ mm) for cold emitted electrons of three cases. (The curve for case b is overlapped by the curve of case c.)

- (a) the radius $0.5 \mu\text{m}$ emitter with 5 kV extraction voltage and -300 V suppressor voltage at a temperature of 1800 K .
- (b) the radius $1.0 \mu\text{m}$ emitter with 5 kV extraction voltage and -300 V suppressor voltage at a temperature of 1800 K .
- (c) the radius $1.0 \mu\text{m}$ emitter with 6 kV extraction voltage and -480 V suppressor voltage at a temperature of 1800 K .

The geometry of the model in case a is from Bronsgeest's file, and geometry of the cases b and c is from the SEM photo mentioned in Chapter 3. In the case a, we set the position of the facet is $z = 0.0 \text{ mm}$, the surface of suppressor is at $z = -0.24 \text{ mm}$, the top surface of the extractor is at $z = 0.51 \text{ mm}$, and the diameter of the extractor aperture is 0.40 mm , the plane of the field free area is taken at $z = 1.5 \text{ mm}$. In the cases b and c, we set the position of the facet is $z = 0.0 \text{ mm}$, the surface of suppressor is at $z = -0.42 \text{ mm}$, the top surface of the extractor is at $z = 0.36 \text{ mm}$, and the diameter of the extractor aperture is 0.40 mm , the plane of the field free area is also taken at $z = 1.5 \text{ mm}$. For every case, we first do the ray tracing for the electrons on a line in x-z plane, which is from the center of the facet to its edge, with an interval of 2 nm . To avoid the inaccurate field in the region near the facet, we emit the electrons from the plane at 1 nm from the facet as suggested by the manual of CPO2D. The electrons will gain some transverse kinetic energy (very small) as they travel from the facet to the plane at $z = 1 \text{ nm}$, the transverse speed is calculated according to the radial electric field, tangent electric field, and total kinetic energy, which is related to the potentials of the electron on the line. After setting the initial conditions, we run the software, which calculates surface charge distribution on the electrodes according to the voltage setting and calculates the trajectories of the electrons, we take the plane at z

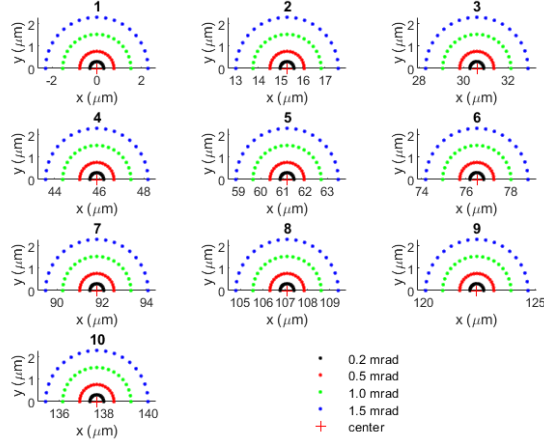


Figure 2.8: The electron positions for 10 apertures in the x - y plane at $z = 1.5 \text{ mm}$. The polar angles of their centers are from 0 to 90 mrad with intervals of 10 mrad . The unit is μm in the graph.

$= 1.5 \text{ mm}$ as the end plane of the trajectories. With the position and slope of an electron trajectory in the plane at $z = 1.5 \text{ mm}$, we can trace back these rays to find the virtual source position for the central beams, the value for case a is about $-30 \mu\text{m}$ and it's about $-13 \mu\text{m}$ for cases b and c. In the field free area, we take virtual source positions for the central beams as the point where all the electrons are from, and we can calculate the polar angles for every electron. The relationship between the electron positions at the facet and its polar angle in the field free area for cold emitted electrons is shown in figure 2.7. 'Cold emitted' electrons here mean that there is no energy distribution, but all the electrons have a fixed normal energy 0.155 eV ($0.155 \text{ eV} = kT$, and $T = 1800 \text{ K}$) and 0 eV tangential energy. By skipping the energy distribution, it's possible to get a clear result, otherwise, it's difficult for the software to give a good ray tracing result.

In the next step, we do the ray tracing for the off-axial beams. We take case a as an example to explain our strategy. For case a, we assume that there are 10 apertures in the $z = 1.5 \text{ mm}$ plane, located on the x -axis in the x - y plane, with a polar angle from 0 to 90 mrad with respect to the source axis. The interval between two adjacent apertures is 10 mrad , as shown in figure 2.8. There are electrons located on 4 half circles around the center of every aperture with 0.2 , 0.5 , 1.0 , and 1.5 mrad half opening angles around the aperture center and one extra electron at the center of every aperture. Because the in-plane mode ray tracing of CPO2D gives very high precision, we convert the coordinates of these electrons in figure 2.8 from Cartesian coordinates (x, y) to polar coordinates (ρ, Φ) , where ρ is the distance from the axis of the source system, and Φ is the azimuthal angle of the electron with respect to the x axis. A separate file is created to store the value of Φ , which is constant for every electron, and only ρ is used for the next step thus getting all the electrons in x - z plane. We calculate the position, slope, and potential values at the facet of all the electrons ending up on the circles in the $z=1.5 \text{ mm}$ plane by interpolating between the ray tracing results

mentioned in the last paragraph. With these interpolated initial conditions, we do the ray tracing for the second round in CPO2D. Then, we get the accurate positions and slopes of the electrons in the field free area, with which we trace back to the virtual source plane of the central beams. With the stored Φ value, the back traced electron positions can also be converted to Cartesian coordinates.

For cases b and c, the procedure is the same, but the polar angles of the aperture centers are different, which are from 0 to 160 *mrad* for the first 9 apertures, with 20 *mrad* interval, and the polar angle for the 10th aperture is 170 *mrad*.

We will analyze the results in the following part of this section.

Figure 2.9 (a) shows the back traced rays (located on half the circles as mentioned above) at the region of the virtual source plane for aperture 5 of case a, which has an axis angle of 40 *mrad* from the source axis, projected in two planes, x-z plane and y-z plane. The top graph is the projection in the x-z plane, and the lower graph is the projection in the y-z plane. The red dashed line is the ray passing the center of aperture 5 in the $z=1.5$ mm plane. The crossovers in the two graphs are at different locations on the z-axis, which indicates the astigmatism of the source system, and the crossover in the x-z plane projection is on the left of the one in the y-z plane projection. Figure 2.9 (b) shows the rays at the region of the virtual source plane for the aperture 3 of case b, which also has an axis angle of 40 *mrad* from the source axis, projected in the x-z plane and y-z plane. The crossovers in the two graphs are also at different locations, but on contrary to Figure 2.9 (a), the crossover in x-z plane projection is on the right of the one in the y-z plane projection. Because of the similarity to case b, the rays for case c are not included.

Figure 2.10 (a) shows the electron positions in 7 slices between two crossovers for aperture 5 of case a. The spot shape is a vertical line for the first crossover and a horizontal line for the second crossover, and the Gaussian image plane should be just in the middle of these two crossovers. The spot shape is quite round in this plane. Figure 2.10 (b) shows the electron positions in 7 slices between two crossovers for aperture 3 of case b. From Figure 2.10 one can see that the source image blur caused by the lens effect is below 1 nm, which is smaller than the order of magnitude of the virtual source size (about tens of nm). Because of the similarity to case b, the slices for case c are not included.

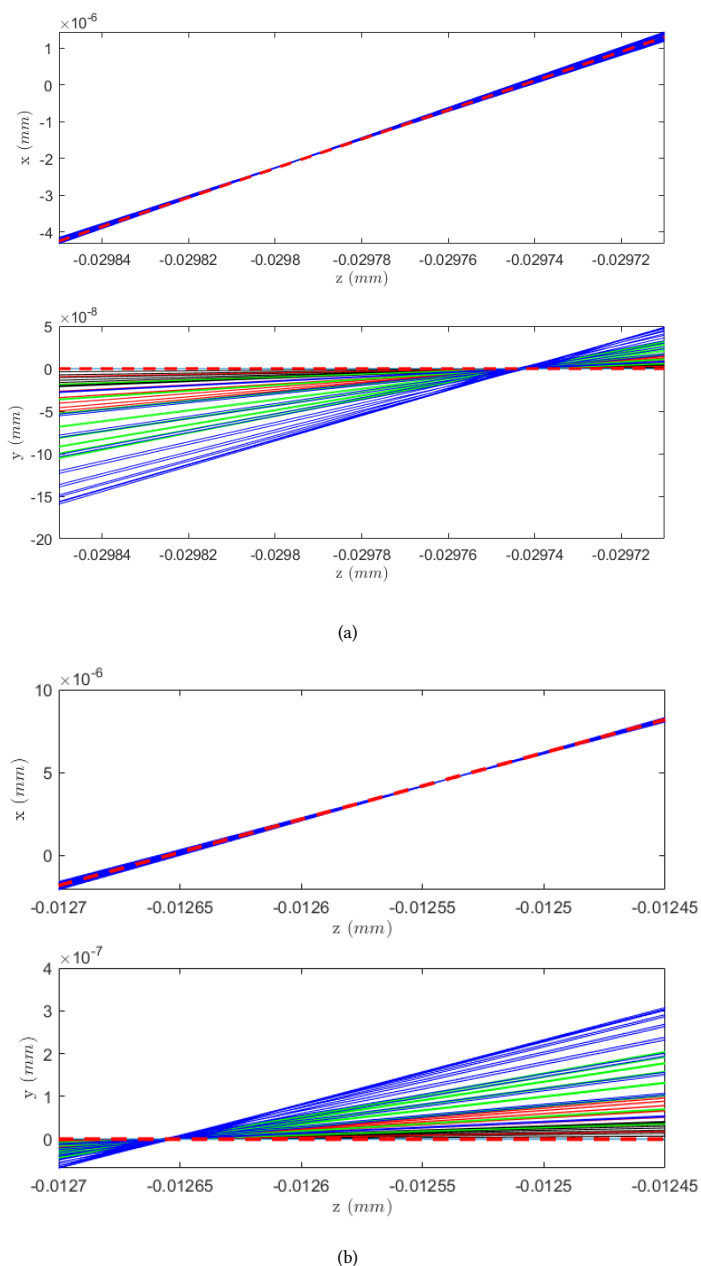
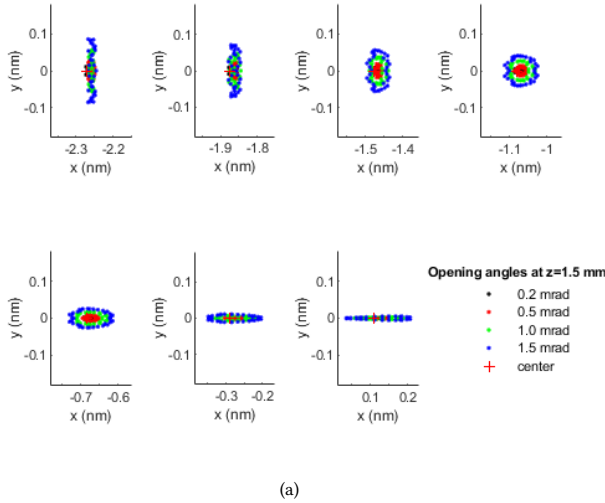
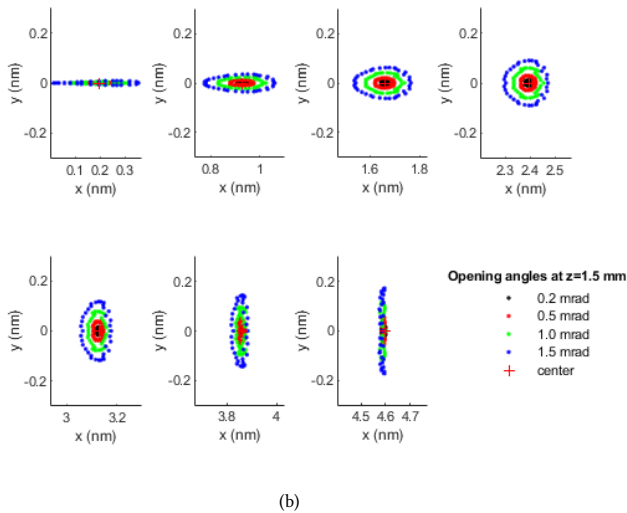


Figure 2.9: (a) Projection on x plane and y plane of the electron trajectories for aperture 5 of case a. Only trajectories of electrons on the half circles at the aperture are calculated, which is only visible in the y-z plane. Note the difference in vertical scales in the 2 figures. The red dash line is the rays of the electron on the axis. (b) Projection on x plane and y plane of the electron trajectories for aperture 3 of case b. The plane at $z=0 \text{ mm}$ is the facet plane. The unit in the graphs is mm . Note that (a) and (b) are at a different scale to accommodate the slope in the x, z projection.



(a)



(b)

Figure 2.10: (a) Trajectory positions in the x and y planes for aperture 5 of case a (axis is at 40 mrad angle). Only electrons on the half circles were traced. The slices are from $z = -29.8 \mu\text{m}$ to $z = -29.74 \mu\text{m}$. And the plane at $z=0.0 \text{ mm}$ is the facet plane. (b) Trajectory positions in the x and y planes for aperture 3 of case b (axis is also at 40 mrad angle). Only electrons on the half circles were traced. The slices are from $z = -12.65 \mu\text{m}$ to $z = -12.54 \mu\text{m}$. The plane at $z=0.0 \text{ mm}$ is the facet plane. Due to the similarity to the case b, the trajectory positions of case c are omitted. The unit in the graphs is nm.

Figure 2.11 (a) shows the electron positions for all 10 apertures in the virtual source plane of the central aperture for case a, where the x and y axis are in 1:1 ratio. The crossovers of the rays and axis are at the left side of the virtual source of the central aperture. The spot shape goes more elliptical as the polar angle of the aperture increases. Figure 2.11 (b)

shows the electron positions for all 10 apertures in the virtual source plane of the central aperture for case b. On contrary to the case a, the crossovers of the rays and x axis in case b are at the right side of the virtual source of the central aperture.

Now, when only the distance from the axis r at the virtual source plane and the polar angle

2

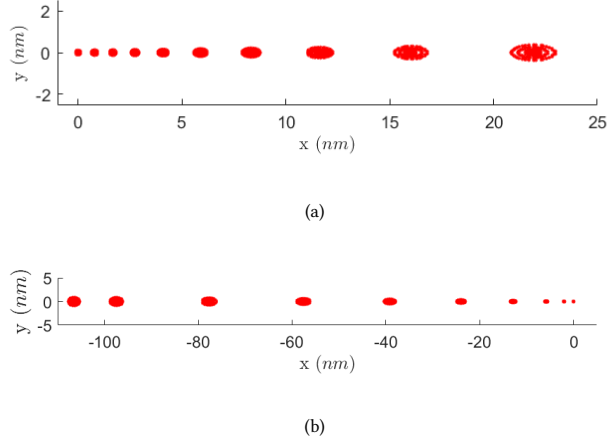


Figure 2.11: (a) The electron positions in the virtual source plane of the central aperture for case a. The x and y axes are in a 1:1 ratio. The electrons were traced at half circles and are here also plotted at the other side of the symmetry plane. (b) The electron positions in the virtual source plane of the central aperture for case b. The x and y axes are in a 1:1 ratio. The unit in the graphs is nm .

with the source axis α are considered, and the positions are mirrored for the negative polar angle, we obtain figure 2.12 for total 10 apertures for cases a and b, the electron positions for case c are not plotted because of its similarity to the data of case b. We can express the relation between r and α as below.

$$r = \Delta f \alpha + C_{S3} \alpha^3 + C_{S5} \alpha^5 \quad (2.13)$$

Where Δf is the remaining defocus from the perfect Gaussian image plane. C_{S3} is the 3rd order spherical aberration coefficient, and C_{S5} is the 5th order spherical aberration coefficient. We perform the fitting at $z_{vs} = -29.6 \mu m$ for case a and at $z_{vs} = -12.8/-13.0 \mu m$ for cases b and c.

The corresponding fitting up to the 3rd order spherical aberration coefficient and the 5th order spherical aberration coefficient are also shown in figure 2.12. In order to avoid contributions from even terms in α , we mirrored the data around $\alpha = 0$.

The most significant conclusion is that the C_{S3} of case a is positive, which is consistent with the literature [21] for the same geometry, but C_{S3} is negative for cases b and c, which have larger radius emitters and different source geometry. At first sight it is surprising to find a negative C_{S3} because it seems to contradict Scherzer's theorem. However, in this case, the emitter surface is part of the lens and this breaks one of the assumptions of Scherzer's theorem namely that there should not be space charge inside the lens. When the trajectories are checked in the test planes with different distances from the emitter facet to

Table 2.1: The spherical aberration coefficients calculated from different fittings.

Coefficients	$\Delta f(\mu m)$	$C_{s3}(\mu m)$	$C_{s5}(mm)$	$Z_{vs}(\mu m)$	
Fit up to 3 rd order	0.06	23.7	-	-29.6	case a
Fit up to 5 th order	0.08	13.9	1.04	-29.6	case a
Fit up to 3 rd order	-0.23	-15.1	-	-12.8	case b
Fit up to 5 th order	-0.10	-34.7	0.56	-12.8	case b
Fit up to 3 rd order	-0.14	-14.9	-	-13.0	case c
Fit up to 5 th order	-0.01	-34.8	0.58	-13.0	case c

the extractor, it's found that the 3rd order spherical aberration is always negative in the planes near the emitter facet, because the emitter is on the axis and cannot be seen like a normal lens, and C_{s3} get less negative or even positive when the electrons travel further from the emitter, when they get more influenced by the field closer to a normal round lens. Secondly, the 5th order spherical aberration is more pronounced for case b, and it should be the same for case c, which has very similar trajectories as case b. In case a, both fittings up to the 3rd order and 5th order spherical aberration don't show a visible difference. But overall, the 3rd order spherical aberration is dominating for every case.

The fitted coefficients can be seen table 2.1. For the fitting up to the 3rd order, the calculated spherical aberration coefficients are $23.7 \mu m$, $-15.1 \mu m$ and $-14.9 \mu m$ for cases a, b and c, respectively. For the fitting up to the 5th order, the calculated 3rd order spherical aberration coefficients C_{s3} are $13.9 \mu m$, $-34.7 \mu m$ and $-34.8 \mu m$ for cases a, b and c, respectively, the calculated 5th order spherical aberration coefficients C_{s5} are $1.04 mm$, $0.56 mm$ and $0.58 mm$ for cases a, b and c, respectively.

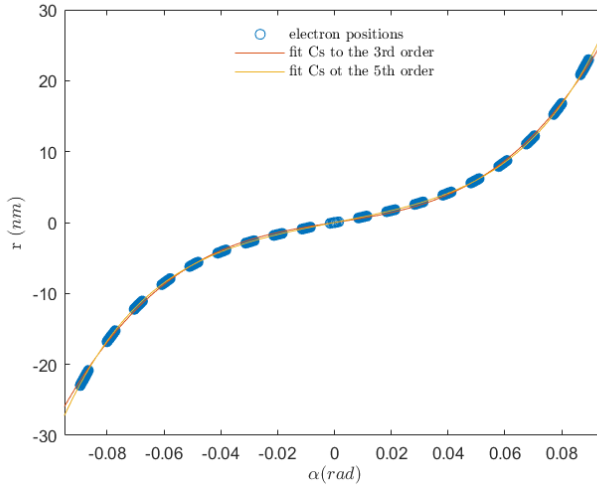
Now, we would like to investigate the contributions of the off-axial aberrations to the virtual source and express them in emission angle and the half opening angle of the off-axial beams. We use the opening angle $d\alpha$ and azimuth angle χ with respect to the aperture center to represent a position in an aperture. Note that the polar angle of the aperture center α is then constant for the aperture. we can get the equations for the electron positions in the virtual source plane of the central aperture as below.

$$x_{vs}(d\alpha, \chi) = B d\alpha^3 \cos \chi + F(2 + \cos(2\chi)) d\alpha^2 \alpha + (C + D) \cos(\chi) d\alpha \alpha^3 + E \alpha^3 \quad (2.14)$$

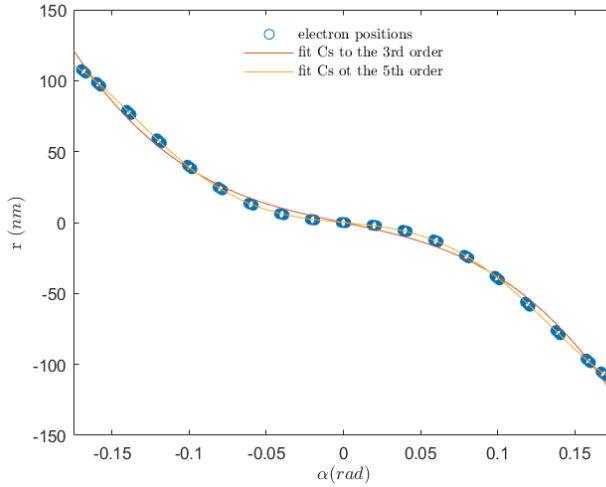
$$y_{vs}(d\alpha, \chi) = B d\alpha^3 \sin \chi + F \sin(2\chi) d\alpha^2 \alpha + (D - C) \sin(\chi) d\alpha \alpha^2 \quad (2.15)$$

where B is the spherical aberration coefficient, F is coma coefficient, C is astigmatism coefficient, D is field curvature coefficient, and E is distortion coefficient. We should keep in mind that these equations are based on terms only up to the 3rd order, for large polar angle beams, the 5th order terms will appear and these equations are not accurate. Figure 2.13 shows the electron position in the virtual source plane of the central aperture and the individual fitting for different apertures. Except for the central beams, the fitting results for the off-axial apertures match the electron positions very well.

The (a) figures of figures 2.14, 2.15 and 2.16 show the individually fitted coefficients for

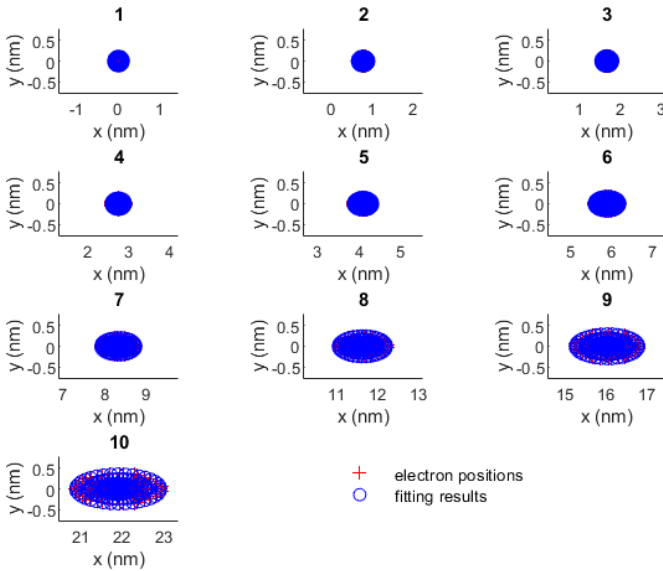


(a)



(b)

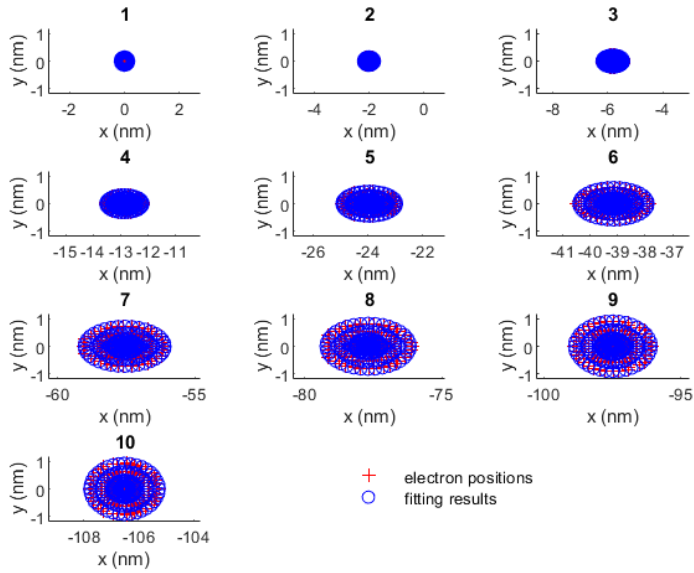
Figure 2.12: (a) The relationship between electron position in the virtual source plane of the central aperture and their polar angle, as well as the fittings up to the 3rd order and 5th order curve. This graph is for case a. The data for the negated polar angles are mirrored for the real ray tracing. (b) The relationship between electron position in the virtual source plane of the central aperture and their polar angle, as well as the fittings up to the 3rd order and 5th order curve, are also included. This graph is for case b. The data for the negated polar angles are mirrored for the real ray tracing



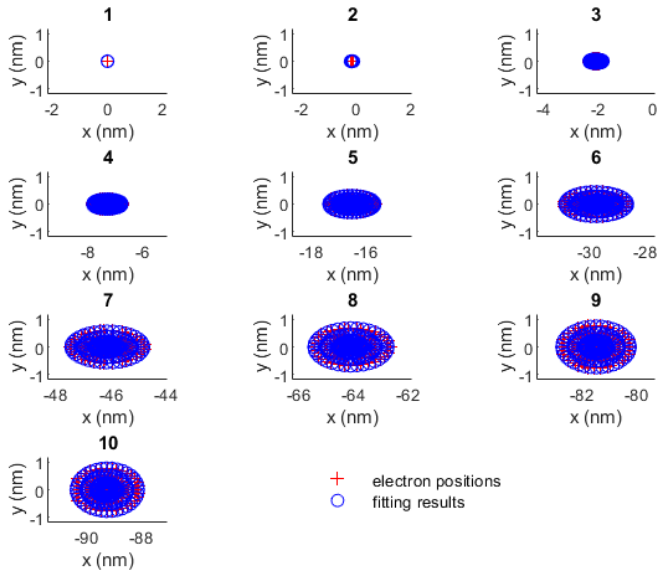
(a)

Figure 2.13: (a) The individual fitting for different apertures for the electrons in the virtual source plane of the central aperture for case a. Red crosses are the electron position, and the blue circle are the fitted results. The x and y axes are in a 1:1 ratio for every subplot.

the off-axis beams of 9 apertures (indices 2-10) for 3 cases, where aperture 1 is the central aperture and is skipped, since the fitting results don't match the electron positions for which the reason could be that the electrons passing the central aperture cannot be described by the equations 2.14 and 2.15. The discrepancy from the trend for the apertures close to the axis may also be related to the fact that the fitting is not done in the exact Gaussian image plane of the central aperture. The (b) figures of figures 2.14, 2.15 and 2.16 show the corresponding aberrations calculated with 1.5 mrad opening angle for every aperture. We see that the discrepancies from the trend in the coefficients have disappeared. We found that the spherical aberration and coma do not show a clear trend for the 3 cases, the reason could be that 1.5 mrad opening angle is too small to display an obvious contribution of spherical aberration and coma in electron positions. Defocus/field curvature and astigmatism contribute a significant part of the spot size, and they both increase with the angle for case a, as expected. When 5th order C_{s5} plays a role, like in cases b and c, the equations 2.14 and 2.15 will be less accurate when the polar angle increases, therefore, the astigmatism coefficient start at about the value of C_{s3} and then goes almost to zero when the positive C_{s5} starts to have an effect.

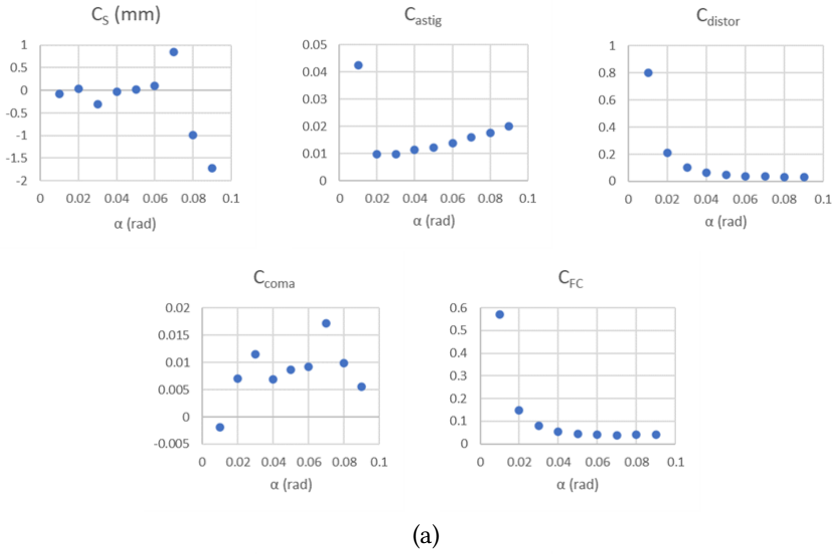


(b)

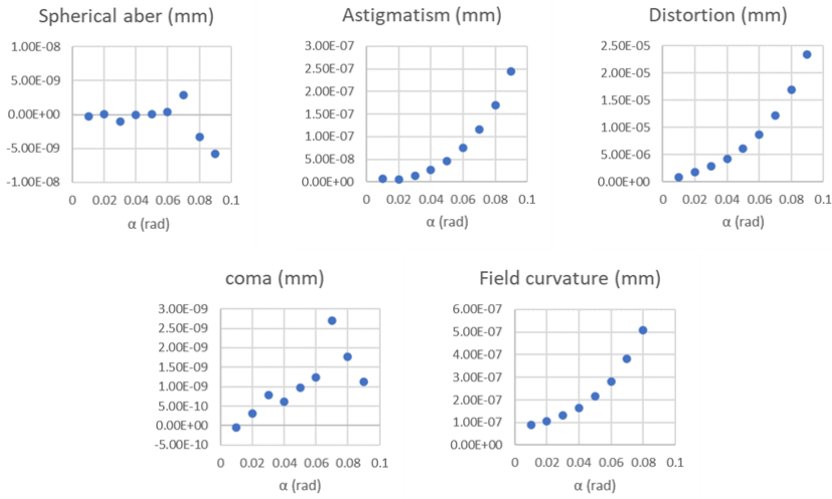


(c)

Figure 2.13: (b) The individual fitting for different apertures for the electrons in the virtual source plane of the central aperture for case b. (c) The individual fitting for different apertures for the electrons in the virtual source plane of the central aperture for case c. Red crosses are the electron position, and the blue circle are the fitted results. The x and y axes are in a 1:1 ratio for every subplot.



(a)



(b)

Figure 2.14: The individual fitting coefficients for the 9 off-axial apertures of case a (a) and the corresponding values of the aberrations (in mm) for a half opening angle of 1.5 mrad in the off-axial beams (b).

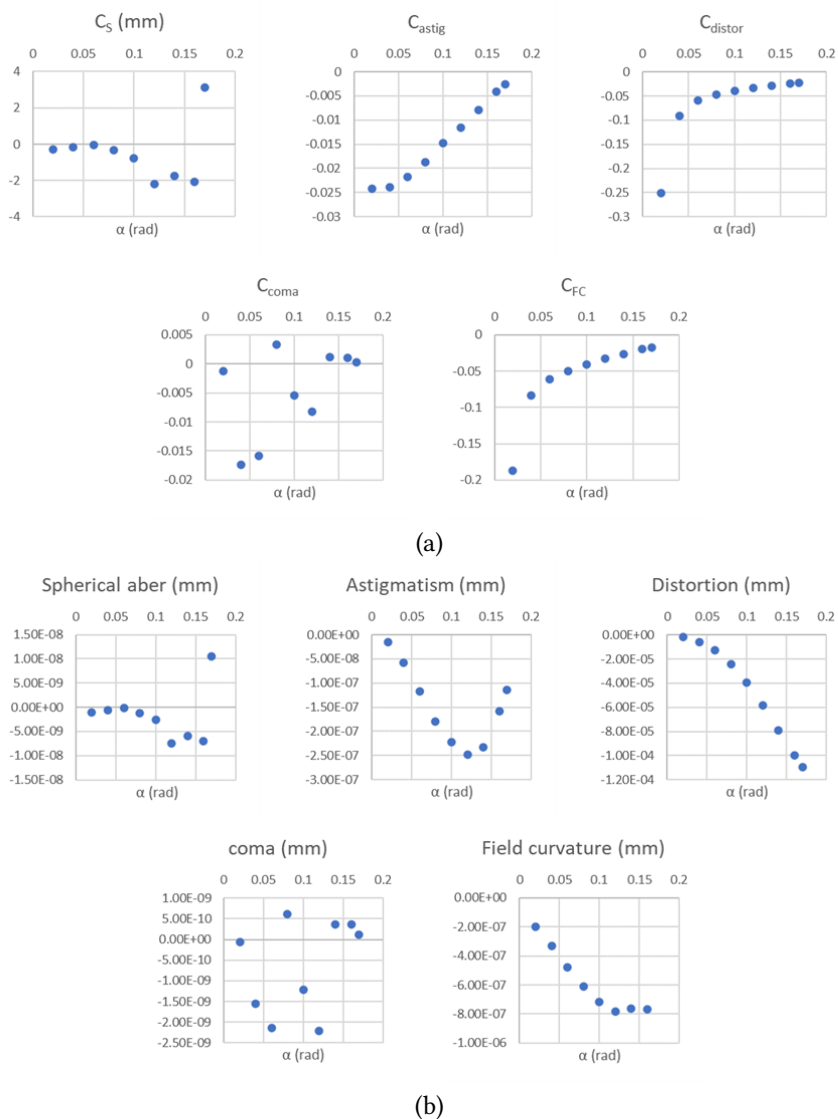


Figure 2.15: The individual fitting coefficients for the 9 off-axial apertures of case b (a) and the corresponding values of the aberrations (in *mm*) for a half opening angle of 1.5 mrad in the off-axial beams (b).

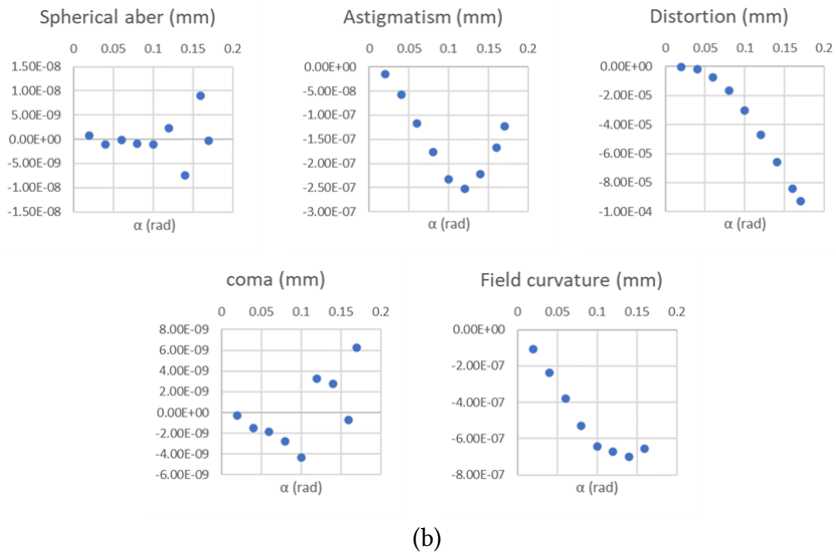
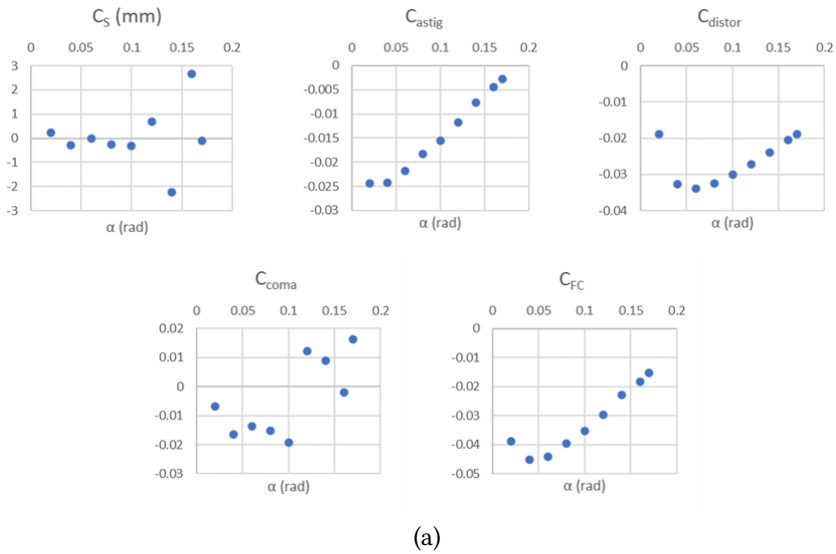


Figure 2.16: The individual fitting coefficients for the 9 off-axial apertures of case c (a) and the corresponding values of the aberrations (in mm) for a half opening angle of 1.5 mrad in the off-axial beams (b).

2.4.2 VIRTUAL SOURCE POSITIONS FOR THE OFF-AXIAL BEAMS

2

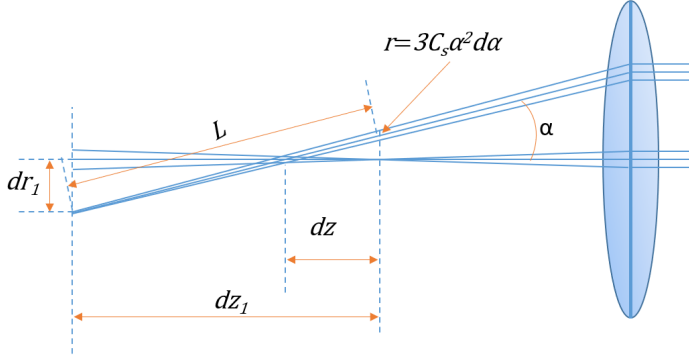


Figure 2.17: The schematic overview of defocus for the off-axial beams in the x - z plane.

It is known that the virtual source positions of the off-axial beams are different from the positions of the central beams. We would like to find out the virtual source position of the electron beams with an off-axial angle now. In the meridional plane of a lens system, the off-axial rays have a displacement from the axis and defocus from the Gaussian plane because of the spherical aberration. For simplicity, only the 3rd order C_{s3} is considered here. For the simplicity, only the 3rd order C_s is considered here. They can be written as below (see figure 2.17):

$$dr = C_s \alpha^3 \quad (2.16)$$

$$dz = C_s \alpha^2 \quad (2.17)$$

dr and dz are the displacement and defocus, respectively, α is the polar angle of the off-axial ray.

For a beam that has a central ray at an angle α with respect to the axis, and a half-opening angle of $d\alpha$, the situation is different, we will derive the displacement and defocus for this beam.

The angles of two rays at the edge of this off-axial beam in the Gaussian image plane are

$$(\alpha \pm d\alpha)^3 = \alpha^3 \pm 3\alpha^2 d\alpha + O(d\alpha^2) \quad (2.18)$$

where $O(d\alpha^2)$ are high-order terms of $d\alpha$, which are negligible for a small $d\alpha$. Therefore, in the meridional tangent plane, the vertical size of the beam is:

$$r = 3C_s \alpha^2 d\alpha \quad (2.19)$$

When we set L as the length on the axis between the virtual source of the on-axis beam and its intercept in the Gaussian plane of an off-axial aperture, the half-opening angle $d\alpha$ can also be written as below.

$$d\alpha = \frac{r \cdot \cos(\alpha)}{L} = \frac{3C_s \cdot \alpha^2 \cdot d\alpha \cdot \cos(\alpha)}{L} \quad (2.20)$$

Then we get

$$L = 3C_s \alpha^2 \cos(\alpha) \quad (2.21)$$

When we set dz_1 as the virtual source defocus for an off-axial aperture, we have

$$dz_1 = L \cos(\alpha) = 3C_s \alpha^2 \cos(\alpha)^2 \quad (2.22)$$

because

$$\cos(\alpha)^2 \cong 1 \quad (2.23)$$

In the end, we have the formula for the defocus of an off-axial aperture,

$$dz_1 = 3C_s \alpha^2 \quad (2.24)$$

When we set dr_1 as the distance from the optical axis of the system to the virtual source of an off-axial beam, with the geometries in figure 2.17, we have:

$$\alpha = \frac{dr_1}{dz_1 - dz} \quad (2.25)$$

Substitute equations 2.17 and 2.24 in equation 2.25. We can have the distance from the axis to the virtual source of an off-axial aperture.

$$dr_1 = \alpha \cdot 2C_s \alpha^2 = 2C_s \alpha^3 \quad (2.26)$$

The equations 2.24 and 2.26 can be used as a mathematical model of defocus dz_1 and displacement dr_1 with factor C_s and position of the central virtual source. The hidden variable in the model is the polar angle α . As explained in figure 2.9 and 2.10, the crossover explained in figure 2.17 is only for the trajectories in the x-z plane, which is also called the meridional focus, there is another crossover in the y-z plane, and this is not at the same position on the z direction because of the astigmatism. The real Gaussian image plane should be between these two crossovers.

Figure 2.18 shows the positions of virtual sources according to equations 2.24 and 2.26 for

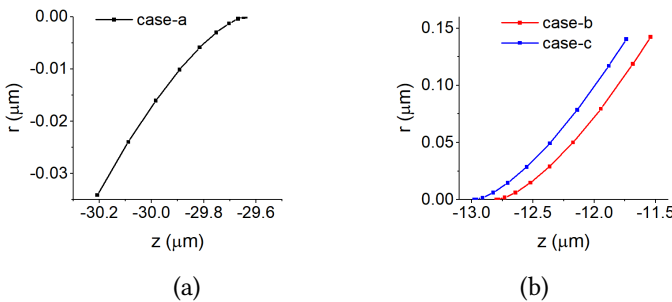


Figure 2.18: The defocus and displacement of the virtual source for axial and off-axial electron beams, (a) for case a, (b) for cases b and c, the value is calculated with the spherical aberration fitted up to only the 3rd order in table 2.1.

the apertures in the 3 cases, with the calculated C_s from table 2.1. For case a, the trend of

the virtual source positions is consistent with the results in literature [21], and the positions for off-axial beams are at the left side of the one for the axial beam, and below the x axis, but for cases b and c, the positions for off-axial beams are at the right side of the one for the axial beam, and above the x axis. Therefore, in order to get the virtual source positions for the off-axial beams in an electron source, it's necessary to do a simulation for different geometries of this source.

2.4.3 CHROMATIC DISPERSION ANALYSIS

Besides the geometric aberration, the dispersion caused by the energy spread is another aberration that should be investigated. By 'dispersion' we refer to the displacement of the virtual source in the r -direction as caused by a different starting energy of the electrons. As mentioned, initial electron positions are set in the plane which is 1 nm after the facet, and the kinetic energy is set as the potential value according to that position. To investigate the dispersion caused by the energy spread in the virtual source plane, besides the default electron, some electrons with higher or lower kinetic energy at the same position are set in the 1 nm plane for a certain angle of an off-axial beam. After ray tracing in CPO2D, their positions and slopes are achieved in the field free region (for instance, in a plane at $z = 1.5\text{ mm}$). Usually, these electrons with different energies have different positions and slopes in the plane at $z = 1.5\text{ mm}$. To acquire the slope in this plane for the electron with default initial energy E at the position of the electron with $E + 1.0\text{ eV}$ initial energy, we calculate the slope for the electron with default initial energy E at the position of the electron with $E + 1.0\text{ eV}$ (the blue dash arrow in figure 2.19). Since we achieved the slope difference of

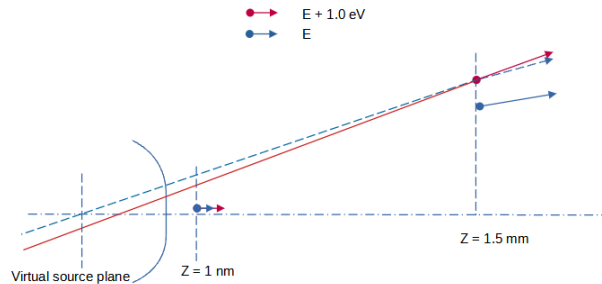


Figure 2.19: The positions and slopes of electrons in the initial plane ($z = 1\text{ nm}$) and field free plane ($z = 1.5\text{ mm}$) with different kinetic energies for an off-axial beam.

these two electrons at the same position, and their initial energy difference is 1.0 eV , we found their position difference at the virtual source plane by back tracing. This position difference is the chromatic dispersion caused by the 1.0 eV energy spread.

Figure 2.20 shows the results for 3 cases with this algorithm. We can see the dispersion caused by the energy spread is below 2 nm/eV for all three cases.

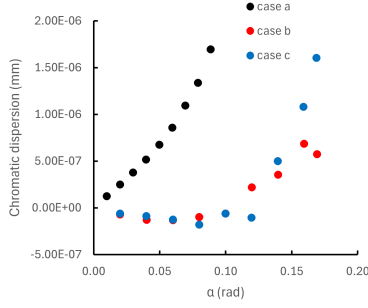


Figure 2.20: Chromatic dispersion caused by 1 eV energy difference for 3 cases.

2.5 VIRTUAL SOURCE CHARACTERISTICS FOR OFF-AXIAL BEAMS

To find the virtual source shape and size for the off-axial beams, we would like to trace the electrons that are emitted from the facet following the Maxwell distribution, because when we follow them to the field free plane at $z = 1.5 \text{ mm}$, we would find the angular distribution of the traces at the center of each aperture. That angular distribution, when looking back at the virtual source plane, gives the virtual source size and the current density distribution in the virtual source. Unfortunately, we found that the ray tracing in this simulation is not sufficiently precise, because we must do this in full 3D ray tracing. Although this is possible in CPO2D with the fields in cylindrical symmetry, a nm size accuracy is required over 1.5 mm distance. We could not get the tracing sufficiently accurate. Therefore, we decided to use Liouville's law to determine the virtual source shape and size.

According to Liouville's law, the emittance is constant along the trajectory. We take ρ as the distance from the optical axis in the virtual source plane, then for the on-axis electron beams emitted from the facet center with tangential energy E_{tan} , there should be equations like below [32][33]:

$$\begin{aligned}
 \underbrace{[\Delta r \Delta p_r]}_{\text{emitting surface}} &= \underbrace{[\Delta r \Delta p_r]}_{\text{virtual surface}} \\
 \Leftrightarrow \underbrace{[r_{launch} m v_t]}_{\text{emitting surface}} &= \underbrace{[\rho m (\alpha_{final} v_{ext})]}_{\text{virtual surface}} \quad (2.27) \\
 \Leftrightarrow r_{launch} \sqrt{E_{tan}} &= \rho \alpha \sqrt{eV_{ext}}
 \end{aligned}$$

This can be rewritten as [20]:

$$\rho = \frac{r}{\alpha} \sqrt{\frac{E_{tan}}{eV_{ext}}} \quad (2.28)$$

The on-axis virtual source size d_v containing 50% of the current is [20]:

$$d_v = 1.67 \frac{r}{\alpha} \sqrt{\frac{kT}{eV_{ext}}} \quad (2.29)$$

Similarly, if the half opening angle of an off-axial aperture in the field free plane ($z = 1.5 \text{ mm}$) is $d\alpha$, and the emission area at the facet has the radius dr , the virtual source size

should be [21]:

$$d_v = 1.67 \frac{dr}{d\alpha} \sqrt{\frac{kT}{eV_{ext}}} \quad (2.30)$$

So now we have found equation 2.5 again, but connected it to Liouville's law. However, we realized that equation 2.30 should not be interpreted as the diameter of a round virtual source, but should be used separately in the plane perpendicular to the plane defined by the optical axis and the off-axial beam (the y - z plane). According to equation 2.30. We then need to know the area on the facet from which the cold electrons came that fill the aperture at $z = 1.5 \text{ mm}$ in the y - z plane.

Thus, we set a series of apertures in the $z = 1.5 \text{ mm}$ plane in case a, with a half-opening

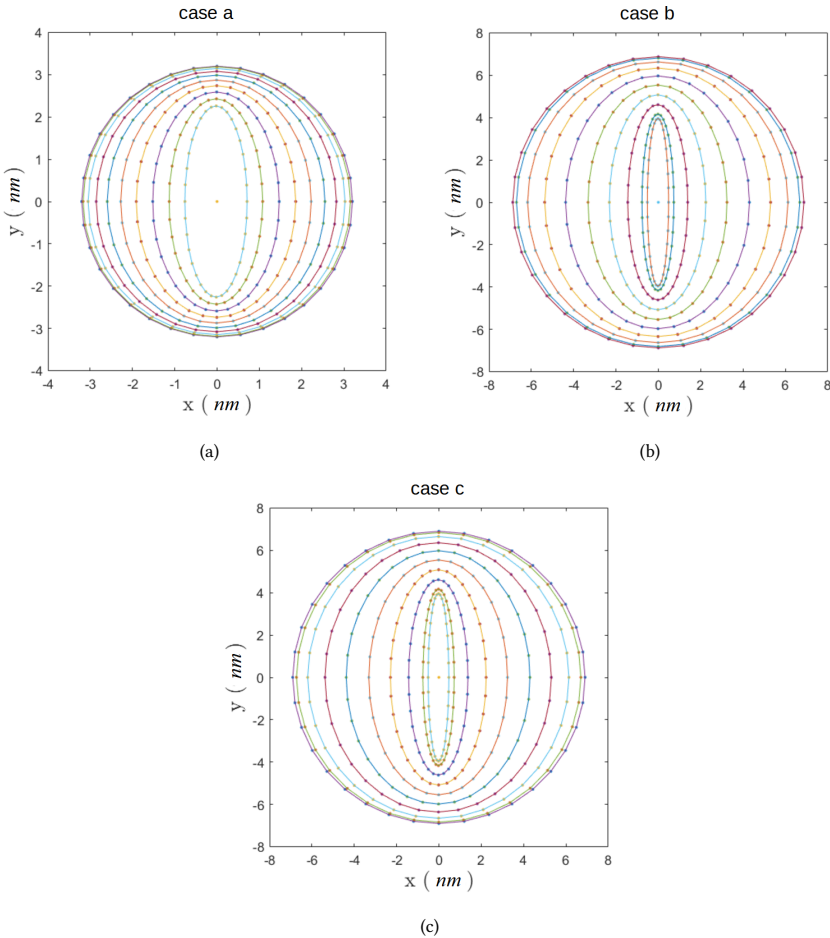


Figure 2.21: The electron positions at the facet, which are backtracked from the electrons at the edges of the apertures in the field-free area. (a)(b)(c) are for cases a, b and c, respectively. They are shifted so the centres are the same as the centre of the axial beam. The connections of electrons for an aperture indicates the emission area at the facet for the aperture. The unit in the figures is nm .

angle of 1.5 mrad , and their axis located on the x-axis at $0, 10 \text{ mrad}, 20 \text{ mrad}$, till 90 mrad with intervals of 10 mrad , then we have 10 apertures in total. For cases b and c, we can define 10 apertures with 1.5 mrad half opening angle, located on the x-axis starting at 0 , then $20 \text{ mrad}, 40 \text{ mrad}$ etc. with 20 mrad interval till 160 mrad , and 170 mrad for the 10^{th} one. When the trajectories of cold emitted electrons are considered, we can find the area on the facet that was responsible for the off-axis beams.

The results are shown in figure 2.21. The first thing that one can see is that the radius of the on-axis emitting area of $1.0 \mu\text{m}$ emitter has almost double the size of the on-axis emitting area of the radius $0.5 \mu\text{m}$ emitter at 5 kV extraction voltage. When we increase the extraction voltage of the radius $1.0 \mu\text{m}$ emitter, the emitting area decreases. We can also see that the size of the emitting area decreases with the polar angle of the apertures, and the size drops faster in the x direction than in the y direction, which means the virtual source is not round for the off-axis beams which has consequences for the application of the Schottky source as a multi-beam source. With the conversion equation 2.30, now applied to both the x-direction and the y-direction, it is possible to convert the size of the emitting area to the size of the virtual source, the results are given in figure 2.22.

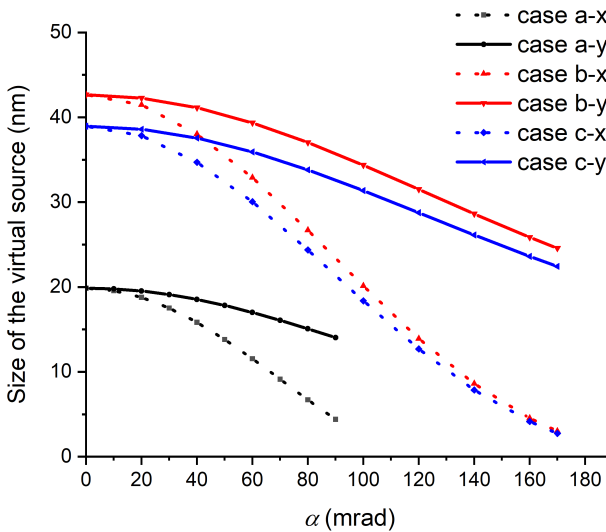


Figure 2.22: The sizes of the virtual source for different directions according to the formula 2.30 and figure 2.21. Black curve and black dash curve represent the virtual source sizes for y and x direction of case a, red curve and red dash curve represent the virtual source sizes for y and x direction of case b, blue curve and blue dash curve represent the virtual source sizes for y and x direction of case c.

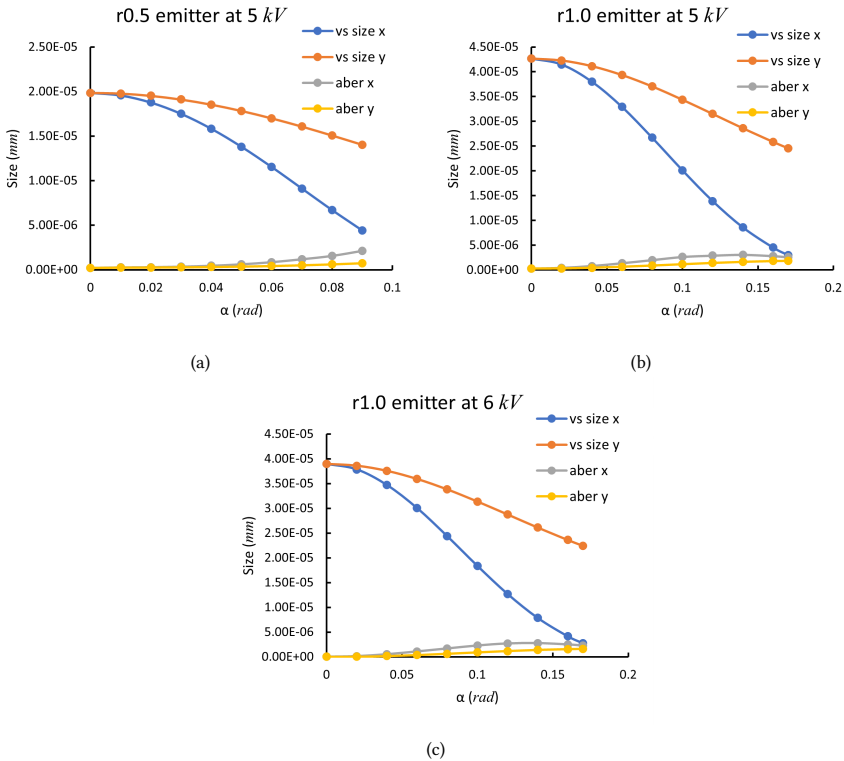


Figure 2.23: The comparison between the virtual source sizes and the spot sizes measured from figure 2.13, which consist of the aberrations in the virtual source plane of the central beams. The aberrations in the plane mainly consist of defocus/field curvature and astigmatism (see figures 2.14, 2.15, 2.16). Figures (a)(b)(c) are for cases a, b and c, respectively.

A comparison between the virtual source sizes and the aberrations in the virtual source plane of the central beams is made in figure 2.23. The aberrations in the plane consist mainly of defocus and astigmatism, as shown in figures 2.14 to 2.16. The blur caused by defocus and astigmatism, in the virtual source plane of the central beams, is smaller than the virtual source sizes up to the maximum polar angles for every case, and the virtual source size is the dominant contribution of the total source size in a Schottky source system.

From the field calculation in CPO2D and the emission current density formula 2.9, we can find the current density anywhere at the facet. Now that we also have the emission areas for the off-axial beams, we can calculate the beam current with the product of the corresponding surface area and the current density for every aperture. The results are shown in figure 2.24. The beam current for the radius $0.5 \mu\text{m}$ emitter at 5 kV extraction voltage is about 2 nA at the central uniform region, the beam current for the radius $1.0 \mu\text{m}$ emitter at 5 kV and 6 kV extraction voltage can be 3 nA and 6 nA respectively, the temperature for all the emitters is at 1800 K .

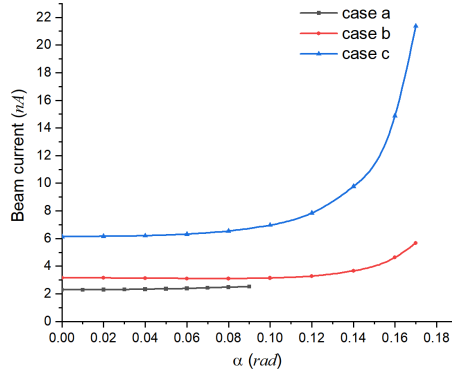


Figure 2.24: The theoretical beam current for different apertures derived from their emission surface area and the current density for 3 cases. Black curve, red curve and blue curves are for cases a, b and c, respectively.

2.6 CONCLUSIONS

In this Chapter, we first reviewed some research on the off-axial electron beam in a source from the literature. Then, we briefly explained the theory of boundary element method (BEM). With the software CPO2D, which is based on the Boundary Element Method, We first did ray tracing of a Schottky source for the cold emitted electrons. With the rays from the facet to a field free plane, we calculated spherical aberration coefficient for 10 apertures of 3 cases, first case is a radius $0.5 \mu\text{m}$ emitter at 5 kV extraction voltage, second case is radius $1.0 \mu\text{m}$ emitter at 5 kV extraction voltage, and the third case is also a radius $1.0 \mu\text{m}$ but with 6 kV extraction voltage, the virtual source plane of the central aperture was chosen for the fitting. We also calculated some aberrations individually for on-axis and off-axial apertures.

We also derived the defocus and displacement of the meridional focus plane for the off-axial apertures. We calculated the planes with these formulas and the spherical aberration coefficient from the last step.

By checking the emission area at the facet for an off-axial aperture in the field-free area, we calculated the virtual source size on both x and y directions for off-axial apertures, we found that the virtual source size is different in x and y direction for off-axial beams, which must be taken into account for a multi-beam application.

We also calculated the size and shape of the aberrations, and we found that both the virtual source and aberration spot will be elongated in y direction, and individual stigmators will be needed to correct for astigmatism. The blur caused by defocus/field curvature and astigmatism, in the virtual source plane of the central beams, is smaller than the virtual source sizes up to the maximum polar angles for every case, and the virtual source size is the dominant contribution of the total source size in a Schottky source system.

3

EMISSION PROPERTIES OF A 1.0-MICRON RADIUS SCHOTTKY SOURCE

3.1 INTRODUCTION

The stability of the emission current of a Schottky source is always of great interest for almost every application. To maintain a constant emission, the temperature and vacuum level in the source chamber must be kept within certain ranges. The emission change is usually due to the emitter shape, and the evolution of the source shape has been studied by several authors [46][51][52][53][54][39][55][41].

Fujita and Shimoyama did experimental research on the emitter shape evolution of a single-crystal tungsten emitter [55]. They applied different temperatures and extraction fields to the emitter and recorded the emission pattern on a phosphor screen to investigate the shape evolution of the emitter. In addition, they tried to explain the emitter shape evolution with the electrostatic field energy stored in the emitter and the extractor system. Bronsgeest and Kruit researched the tip geometry change for different conditions [53][54] by recording the pattern change of the 'ring collapse', which is always associated with the periodic fluctuations of the beam current. It's found that the emitter shape changes with large time intervals, and the cycle starts with a (1 0 0) facet at the tip end, then it decreases in size, and then a ring-shaped step is formed on the facet. The cycle finishes when the atoms of the step are transported away. Furthermore, it was found that a low extraction voltage can continuously cause the change of the emitter end, 'ring collapse' happens, and the size of the emitter grows. On the other hand, if the extraction voltage is too high, there will be more distinguished steps at the facet, and the facet will get smaller. Therefore, a sufficiently high extraction voltage can prevent the ring collapse, and a compromised extraction voltage can keep the emitter shape constant.

Bahm et al. carried out research on the long-term operation of different size Schottky emitters at different angular intensities [56]. The radii of the emitters used in their research are from $0.32 \mu\text{m}$ to $0.83 \mu\text{m}$, and the operations for the emitters are from about 10000 to

18000 hours, the angular intensities in their study are from 0.25 to 0.71 mA/sr. They found that ring collapse does not occur, and the emission is stable when the angular intensity is greater than 0.3 mA/sr. However, this research was only about the central angular intensity, and we would like to know the performance of the off-axial electron beam, as this is important in a multi-beam electron source.

In this chapter, we want to check the emission stability for a higher angular intensity, say 1.0 mA/sr, for the whole emission pattern. A large radius Schottky emitter benefits applications with a large beam current because of its stable emission at high angular intensity. Therefore, we would like to choose a 1.0 μm radius emitter for the experiment. The range of the uniform emission is also of particular interest for a multi-beam application because an equal beamlet current is needed in that scenario. Therefore, we designed and built a setup to check the emission stability and pattern to achieve the goals.

3

3.2 THE CHARACTERIZATION SETUP FOR A LARGE RADIUS (1.0 μm) SCHOTTKY EMITTER

Figure 3.1 shows the design of the emitter characterization setup. The setup can measure the beam current and simultaneously photograph the emission pattern. The yellow part is the vacuum vessel with 6 ConFlat (CF) UHV Flanges. The emitter source module is mounted on the left flange, and a viewport is mounted on the right flange of the vacuum vessel. The Faraday cup module is brown and mounted on the emitter module. It is electrically isolated from other parts but only connected to a feedthrough pin (not shown in the graph). The pin is connected to a pico-Amp meter outside the vacuum. Therefore, we can measure the total beam current through the extractor. Figure 3.1b shows how the Faraday cup is isolated. The Faraday cup is mounted to a metal plate with PEEK screws, and there are glass washers between the Faraday cup and the metal plate. The green geometry indicates the emission cone determined by the emitter tip and extractor hole.

Because the bottom of the faraday cup is a YAG screen coated with a thin layer of aluminum, we can take a photo of the emission pattern on the YAG screen with a camera and a 1 inch tube lens outside the vacuum chamber at the same time. We assume the integration of the total brightness in a photo is proportional to the total YAG current with a converting factor. After we get the factor by integrating the brightness and comparing the result with the YAG current measured by a pico-Amp meter, it will be used to calibrate the image intensity in terms of current for every pixel. With the dimensions of the setup geometry, we can convert the emission pattern from pixel coordinates (on camera CCD) into polar angular coordinates (in the source). In this way, we can get the angular intensity distribution concerning the emission angle. We will discuss the details of the pixel-angle conversion in the next section.

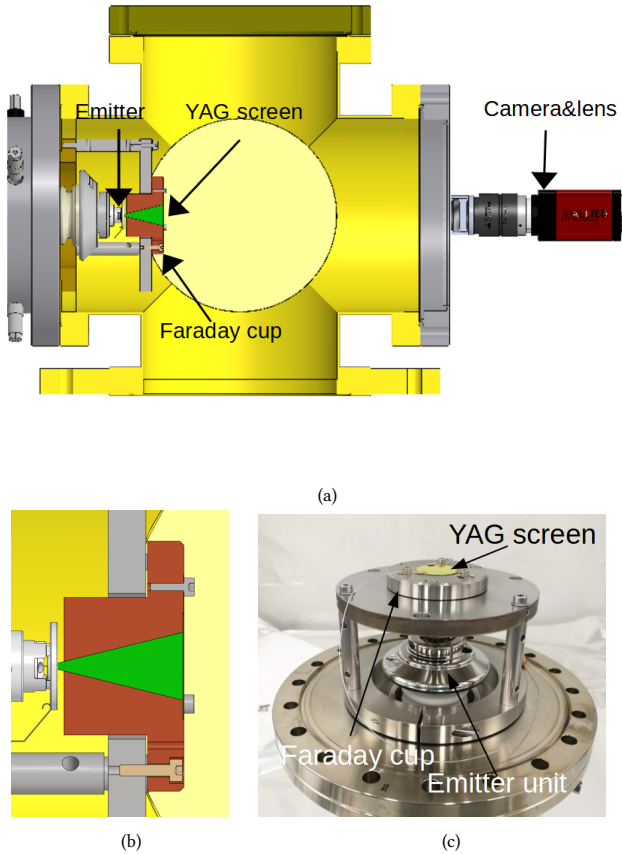


Figure 3.1: (a) The schematic view of the characterization setup. (b) The emitter unit and Faraday cup in the setup. (c) The photo of the emitter unit and Faraday cup during assembling.

3.3 ANGULAR INTENSITY CALCULATION ALGORITHM AND ITS MAP IN ANGULAR COORDINATE

The angular intensity is one of the essential parameters for any electron source, and it's preferable to be expressed in the angular coordinates. However, when we take a photo of the emission pattern on a YAG screen in the setup, it's just a photo without any angular information. There is no angular intensity, either. Therefore, we need to convert the pattern in the image into angular coordinates according to the setup's geometry. Below we will show the derivation of the converting equations, and we also made the Python code accordingly.

First, we need to find the center of the emission pattern in the photo. The Moments() function in the OpenCV library [57] has been used to calculate the mass center of the pattern regarding the brightness of every pixel. A photo ($x \times y$ pixels) in grey level will be

taken as an array $P(x, y)$ in Python3.7 [58]. The spatial moments m_{ji} is computed as:

$$m_{ji} = \sum_x \sum_y P(x, y) \cdot x^j \cdot y^i \quad (3.1)$$

where P is the pixel brightness at the (x, y) position. The mass center is calculated as follows:

$$\bar{x} = \frac{m_{10}}{m_{00}}, \bar{y} = \frac{m_{01}}{m_{00}} \quad (3.2)$$

Then the original 640×480 pixels image will be cropped to a 201×201 pixel image with the center at (\bar{x}, \bar{y}) .

Then we integrate the brightness of the whole cropped photo and calculate the ratio between the integral (total light) and I_{screen} measured by a pico-Amp meter. We assume there is a factor R_{oe} , which satisfies the following equation:

$$\iint R_{oe} P(x, y) dx dy = I_{screen} \quad (3.3)$$

Or in a discrete form

$$\sum R_{oe} S_1 P(x, y) = I_{screen} \quad (3.4)$$

Where S_1 is the area of a pixel. Then,

$$R_{oe} = I_{screen} / (S_1 \times \sum P(x, y)) \quad (3.5)$$

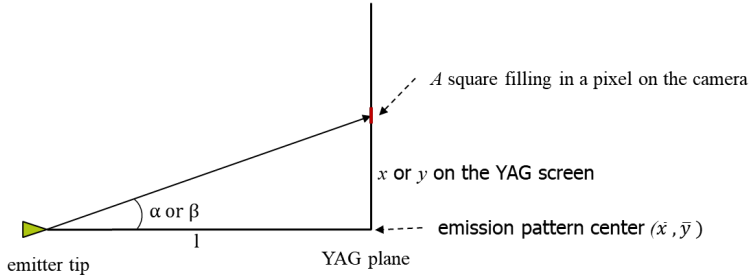


Figure 3.2: The schematic view of the geometry of the virtual source and a pixel on the YAG.

With the pixel position (x, y) and the distance between the virtual source and the YAG plane, we can correlate every pixel with the angle coordinates (α, β) .

$$\alpha = \arctan(x/l), \beta = \arctan(y/l) \quad (3.6)$$

$$\gamma = \sqrt{\alpha^2 + \beta^2} \quad (3.7)$$

$$S_{ef} = S_1 \cdot \cos(\gamma) \quad (3.8)$$

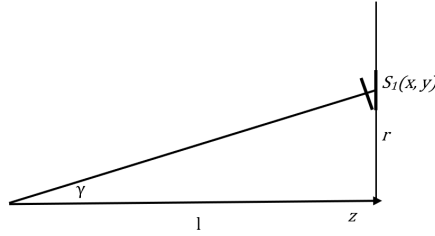


Figure 3.3: The graph shows the relation between the pixel area surface and the opening angle.

With the R_{oe} from equation 3.5, then the current for an individual pixel is

$$I_{pixel} = R_{oe} \cdot S_1 \cdot P(x, y) \quad (3.9)$$

The corresponding solid angle for the individual pixel is

$$\gamma_{pixel} = \frac{\cos \gamma \cdot S_1}{l^2} \quad (3.10)$$

So, the angular intensity for a particular pixel

$$I'(x, y) = \frac{I_{pixel}}{\gamma_{pixel}} = \frac{R_{oe} \cdot l^2 \cdot P(x, y)}{\cos \gamma} \quad (3.11)$$

We replace every pixel (x, y) with the angle (α, β) . And make the plot of $I'(\alpha, \beta)$. After implementing the algorithm in Python3.7, we can plot the angular intensity map with the angular coordinates shown in the next section.

3.4 EMISSION PATTERNS AND I-V CURVES FOR DIFFERENT TEMPERATURES

A $1.0 \mu m$ radius TFE emitter from Denka Company Limited. was put into the setup and operated after necessary preparations. The Emitter serial number is 231815, and it's revised in the factory for the angular intensity of 1.0 mA/sr . The emission patterns and YAG current for different extractor voltages are recorded for 1700 K, 1750 K, 1800 K, and 1850 K temperatures, the temperature was calculated from the filament current according to the data sheet. Before the measurements for every temperature, we run the emitter for at least 40 hours to get the emission stable. Table 3.1 shows the extractor voltage and angular intensity before the measurement. The relation between filament current and temperature in our setup could be slightly different from the table because of the different environments. The proportional suppressor voltages (shown in table 3.2) are also applied to keep the field the same at the emitter facet. The base pressure in the emitter chamber was about $0.9 \times 10^{-9} \text{ mBar}$, and it was about $4.0 \times 10^{-9} \text{ mBar}$ when the source was running.

Table 3.2: The extractor and suppressor voltages used in the measurement.

$V_{extractor} / kV$	$V_{suppressor}/V$
3.00	240
3.50	280
4.00	320
4.50	360
5.00	400
5.50	440
6.00	480

Table 3.1: Conditioning parameters before measurement.

Filament Current /A	Filament Temperature /K	Run time before measurement /hour	Extractor Voltage /kV	I' /mA/sr
2.20	1700	40	5.50	0.54
2.24	1750	40	5.25	0.51
2.29	1800	40	5.00	0.54
2.32	1850	40	5.30	0.81

Figure 3.4 shows the angular intensity maps for the temperature of 1700 K, with the extractor voltages from 3.5 kV to 6.0 kV with a 0.5 kV interval. All the maps are rotated to be straight. From the graph, we can see that the angular intensities increase with the extractor voltage, but the value at about 150 mrad increases faster than the value at the center, this is because the angular intensity I' varies non-linearly with the field, and the field at the edges is much larger than it in the center. There are eight emission vertexes in the ring of 150 mrad, which is caused by the crystalline structure of the facet. Another observation is that the angular intensity is evenly distributed up to 100 mrad within the 'dog ear' region. Figure 3.4 is an equivalent 2D render of the classical three kinds of I' distribution [59], and the classical three kinds of distributions are unimodal distribution, uniform distribution, and bimodal distribution or 'dog ear' distribution.

Figure 3.5, Figure 3.6, and Figure 3.7 are the angular intensity maps with different extractor voltages for the temperature of 1750 K, 1800 K, and 1850 K, respectively. They show a similar trend as figure 3.4. For 1750 K and 1800K, the flat emission pattern occurred at 4.0 kV and 4.5 kV, respectively. For 1850 K, the relative flat emission pattern occurred at about 4.5 kV. For the same extractor voltage, the height of the ring decreases as the temperature increases from 1700 K to 1850 K.

As shown in Figure 3.7f, there is a horizontal dash line at the center and a slant dash line crossing two vertices of the emission pattern. The profiles along the horizontal line (blue dash line) and the slant line (yellow dash line) will be presented in the next paragraphs for a different presentation of the emission.

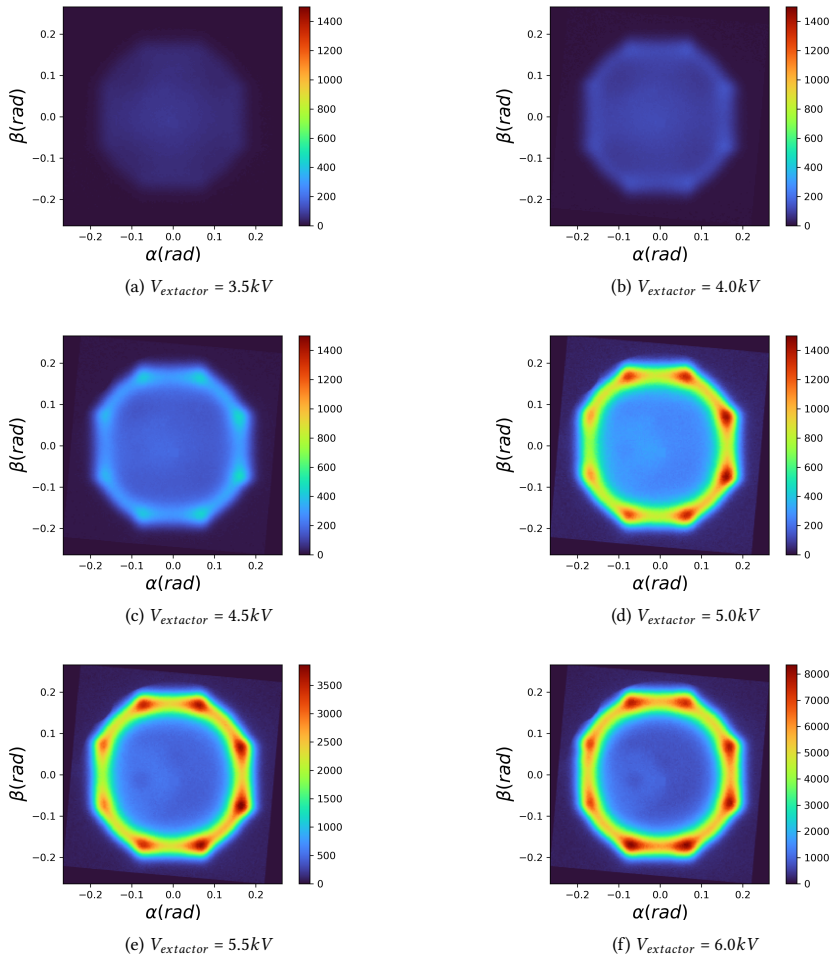


Figure 3.4: The angular intensity maps for different extractor voltages, the emitter temperature is 1700 K, the unit of the color bar is $\mu\text{A}/\text{sr}$.

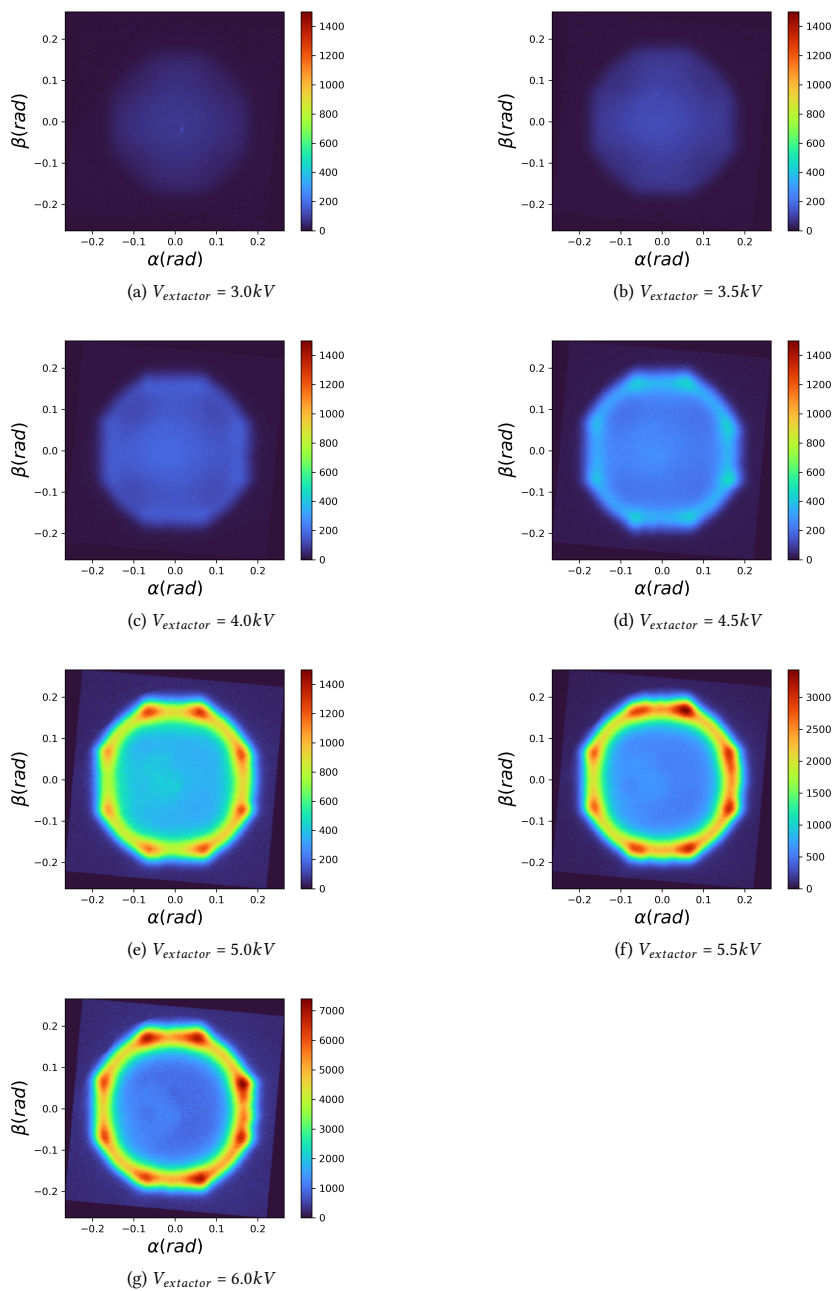


Figure 3.5: The angular intensity maps for different extractor voltages, the emitter temperature is 1750 K, the unit of the color bar is $\mu\text{A}/\text{sr}$.

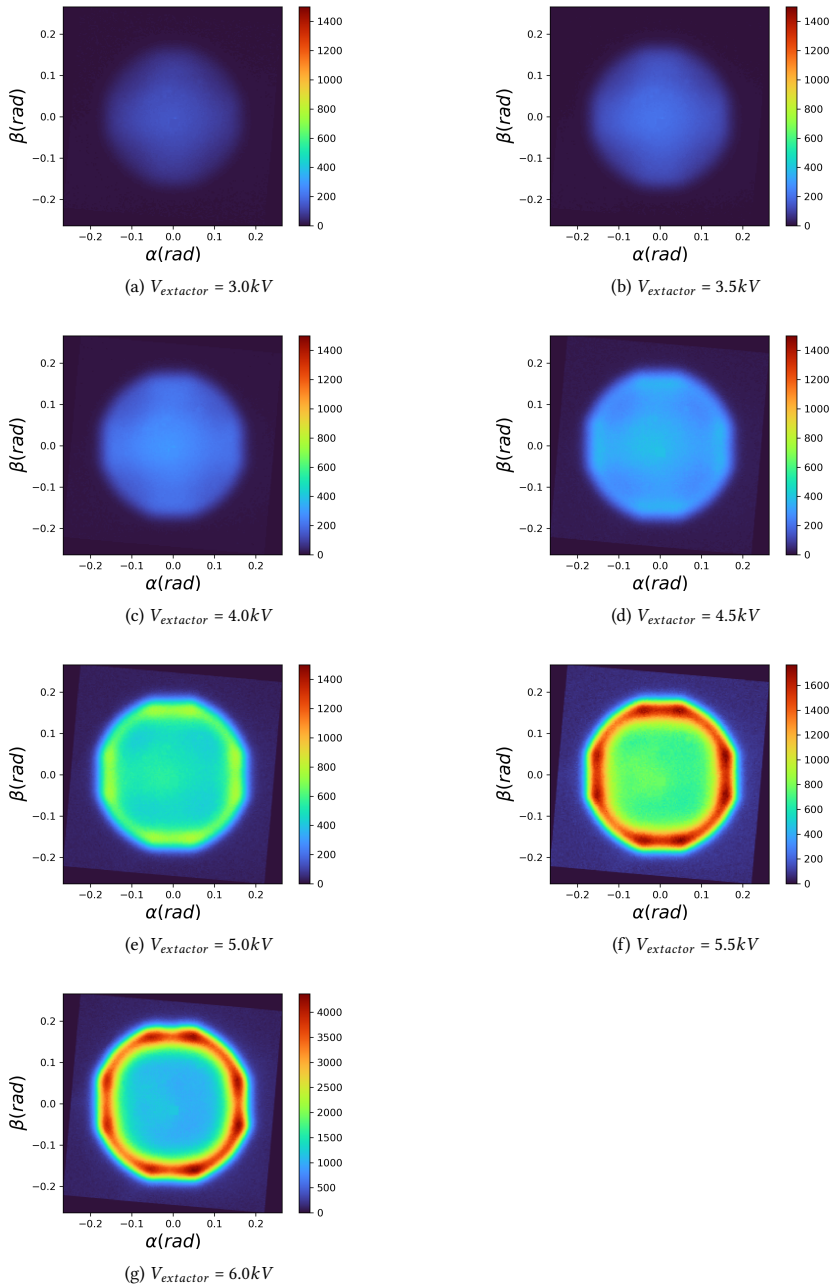


Figure 3.6: The angular intensity maps for different extractor voltages, the emitter temperature is 1800 K, the unit of the color bar is $\mu\text{A}/\text{sr}$.

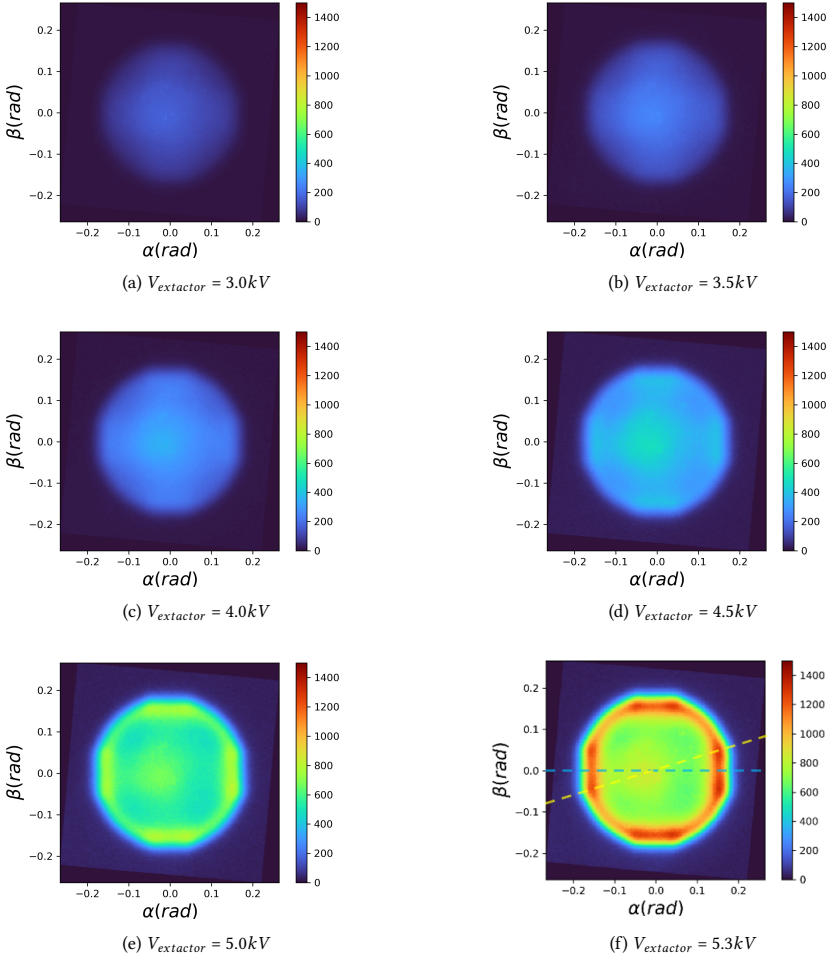


Figure 3.7: The angular intensity maps for different extractor voltages, the emitter temperature is 1850 K, the unit of the color bar is $\mu\text{A}/\text{sr}$.

Figure 3.8 and Figure 3.9 show the angular intensity profiles for different extractor voltages at emitter temperatures of 1700 K, 1750 K, 1800 K, and 1850 K. The figures give a description of the emission patterns for extractor voltages above 5.0 kV, and it's difficult to distinguish the curves for the extractor voltage below 5.0 kV because the curves merged at a low value with respect to the graph scale. For the extractor voltages of 5.0 kV and below, the profile curves are better visible in the logarithm scale in figure 3.10 and figure 3.11. With these profiles, we find the 1.0 mA/sr angular intensity is achievable for the temperatures from 1700 K to 1800 K. For the temperature of 1850 K, we could only apply extractor voltage more than 5.3 kV, because the extractor current will reach the 1.0 mA limit of the power supply and the extractor voltage will drop if I increase the extractor voltage to a higher value.

When we investigate between 1700 K to 1850 K, we see the higher temperature, the lower the dog ears, which should be preferable for a long lifespan, and the stable performance of a TFE emitter. For the emitter temperature of 1850 K, the center area inside the dog ear is not very uniform, though the height of the dog ear is relatively low. So, it's not an optimal temperature, either.

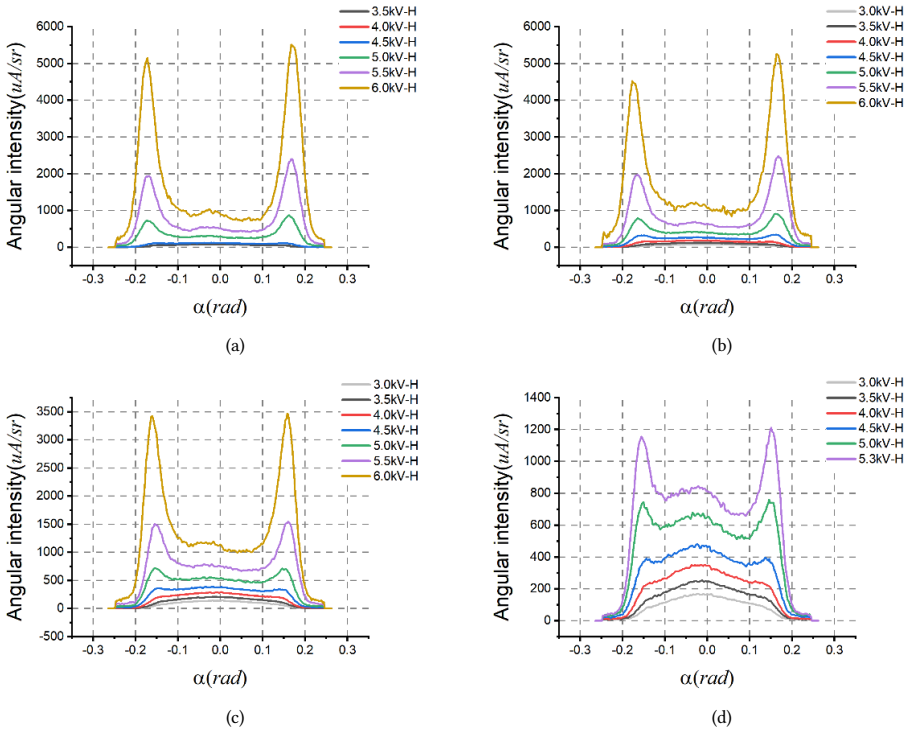


Figure 3.8: Profiles along the horizontal line in linear scale for 4 temperatures (a:1700 K, b:1750 K, c:1800 K, d:1850 K).

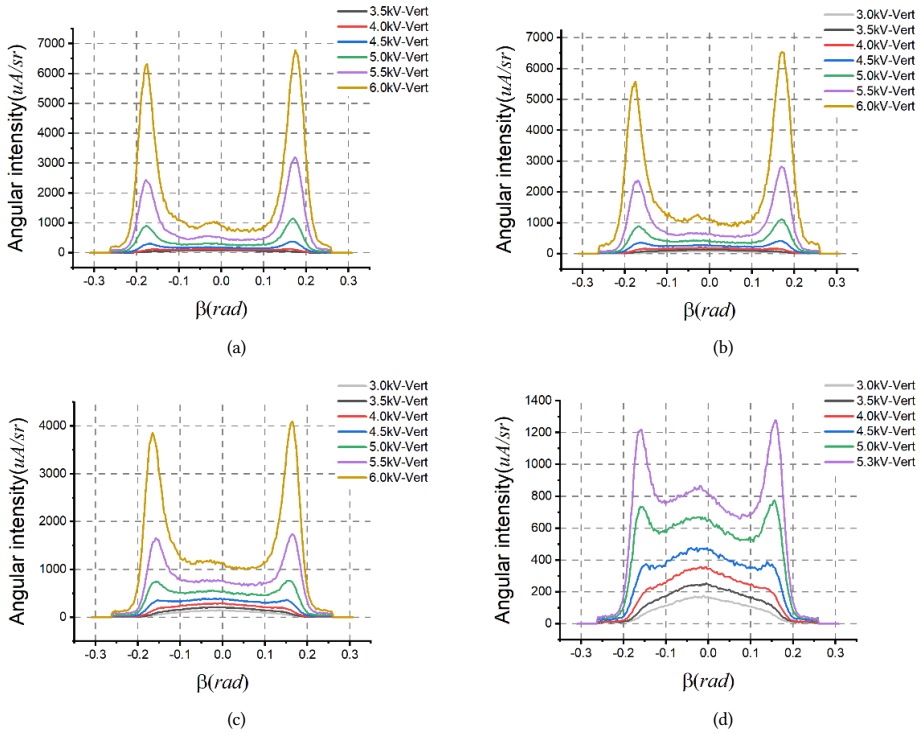


Figure 3.9: Profiles along the slant line in linear scale for 4 temperatures (a:1700 K, b:1750 K, c:1800 K, d:1850 K).

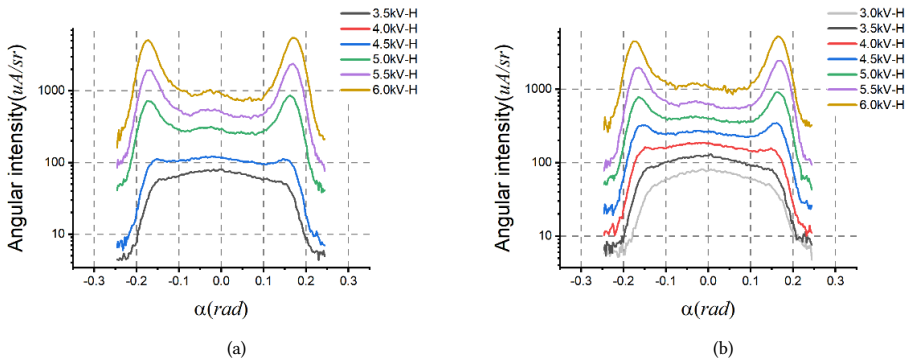


Figure 3.10: Profiles along the horizontal line in logarithm scale for 4 temperatures (a:1700 K, b:1750 K, c:1800 K, d:1850 K).

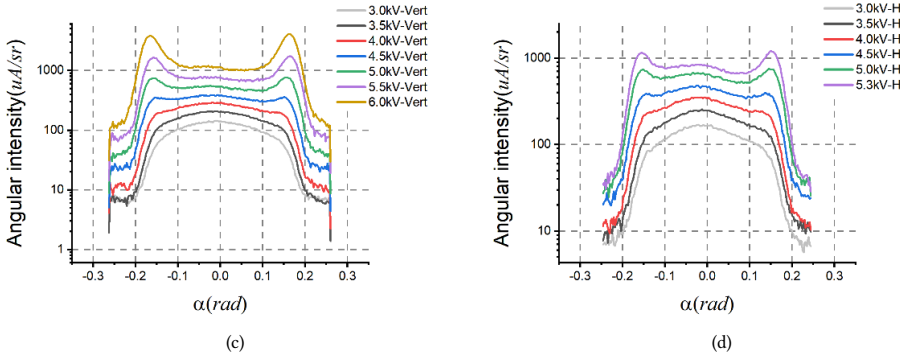


Figure 3.10: Profiles along the horizontal line in logarithm scale for 4 temperatures (a:1700 K, b:1750 K, c:1800 K, d:1850 K).

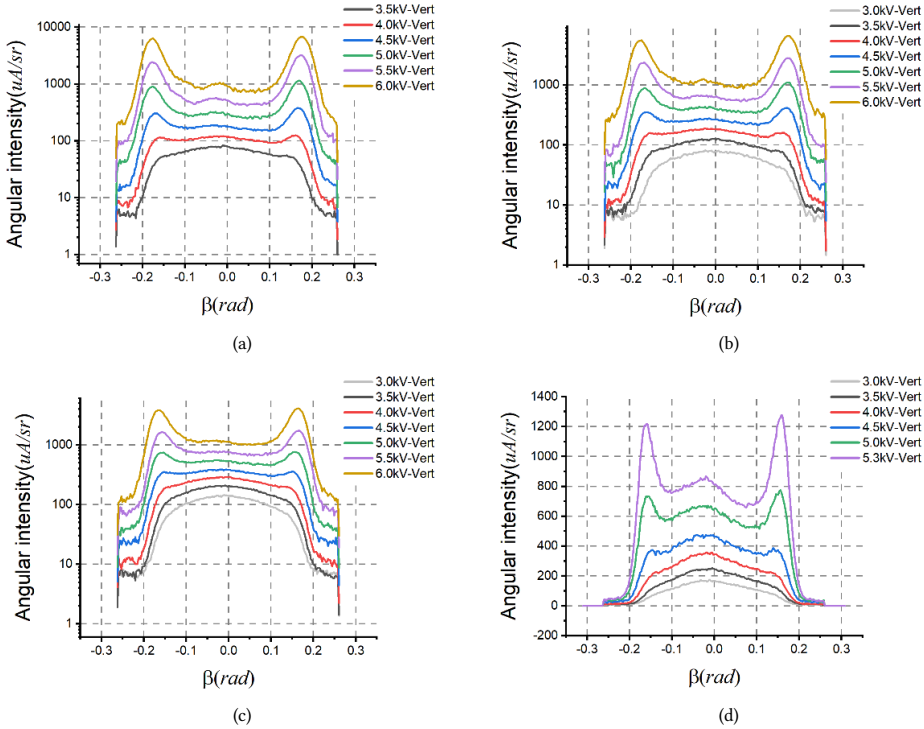


Figure 3.11: Profiles along the slant line in logarithm scale for 4 temperatures (a:1700 K, b:1750 K, c:1800 K, d:1850 K).

Figure 3.12 shows the screen current, extractor current, and total current versus the central angular intensity I' for different temperatures. The screen current is the current received by the Faraday cup. It's mainly the current received by the YAG screen on the Faraday cup. The extractor current is the current received by the extractor, this value can be read out from the source high voltage power supply, and it's mainly the current emitted from the shank of an emitter. Finally, the sum of the screen current and extractor current is the total current emitted from the emitter.

First, we can notice that the extractor current (black curves, mostly from the shank emission) is greater with respect to the percentage for higher emitter temperatures. The extractor will intercept the shank emission, therefore, the shank emission could not benefit the primary electron beams. Even more, larger shank emissions will make the total current close to 1.0 mA, which is usually the limit of a commercial electron source power supply, and cause problems. Therefore, we should also avoid high emitter temperatures to limit a large shank emission. Secondly, when we check only the screen current (blue curves), the current emitted from the central area of the facet on the emitter should be linear to the central angular intensity I' , it's the current in the dog-ear area that causes the steep increase of the screen current. And for the higher emitter temperatures, the increase above the 'linear' screen current (let's assume a 'linear' screen current, which is proportional to the central angular intensity) is relatively less. It tells the same story as figure 3.8: the 'dog area' contains relatively less current for the higher emitter temperatures. These two conclusions suggest taking an intermediate temperature between 1700 K and 1850 K.

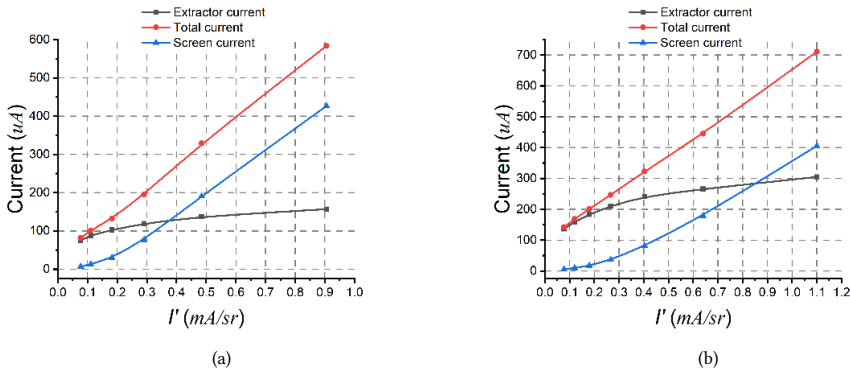


Figure 3.12: The relation between emission currents and central angular intensity (a:1700 K, b:1750 K, c:1800 K, d:1850 K).

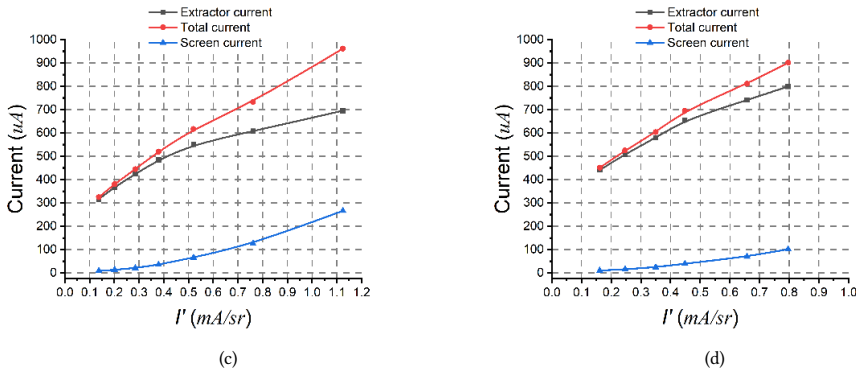


Figure 3.12: The relation between emission currents and central angular intensity (a:1700 K, b:1750 K, c:1800 K, d:1850 K).

If we define the ratio between the central angular intensity and total current as transmission, figure 3.13 shows the transmission of different angular intensities (interpolated from the data point in figure 3.12) over the four temperatures. Though the transmission ratio doesn't have a clear physical meaning, the higher value is the better for many reasons. When we increase the temperature from 1700 K to 1850 K, the transmission drops for all the angular intensities because of the increase of the shank emission for higher temperatures. Figure 3.14 shows the relations between the total current and emitter temperature for different central angular intensities. The total current is also higher for higher temperatures for the same angular intensity.

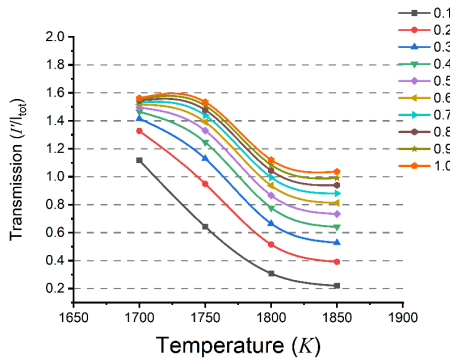


Figure 3.13: The transmission between angular intensity I' and total current at different temperatures for different angular intensities. The legend is the angular intensity, and the unit is mA/sr .

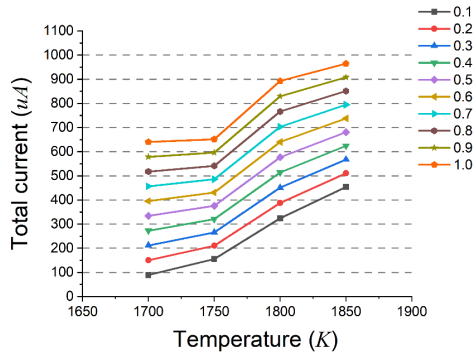


Figure 3.14: The relation between total current and emitter temperature. The legend is the angular intensity, and the unit is mA/sr .

3.5 LONG-TERM EMISSION MEASUREMENT CURVES

3.5.1 THE ANGULAR INTENSITY AND YAG CURRENT EVOLUTION FOR A LONG-TERM OPERATION

The steps of the YAG screen current in figure 3.15 are caused by increasing the filament current/emitter temperature. The YAG screen current was dropping at every filament current. However, the calculated angular intensities show that the central angular intensity increased after increasing the filament current. The drop in the YAG current may be caused by the lower 'dog ear' height. The longest period without any adjustment is about a month, from 23/09/2020 to 28/10/2020.

Figure 3.16 shows the log data from 02/11/2020 to 05/12/2020. In this period, we kept the

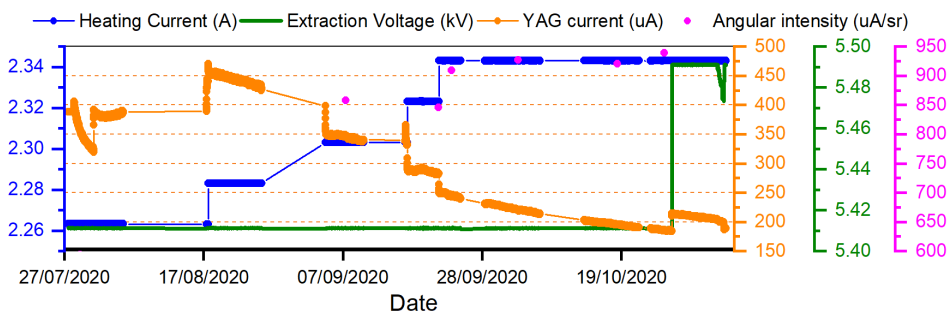


Figure 3.15: The angular intensity and YAG screen current evolution between 27/07/2020 and 02/11/2020. The angular intensity was measured on the optical axis.

filament current constant at 2.34 A. If the emitter's total current (not shown in the graph) reaches 1.0 mA, which is the maximum output current of the source HV power supply, then the power supply will lower the extractor voltage (see the green curve 30/11/2020). So, the suppressor voltage was increased to suppress the total emission, this action happened

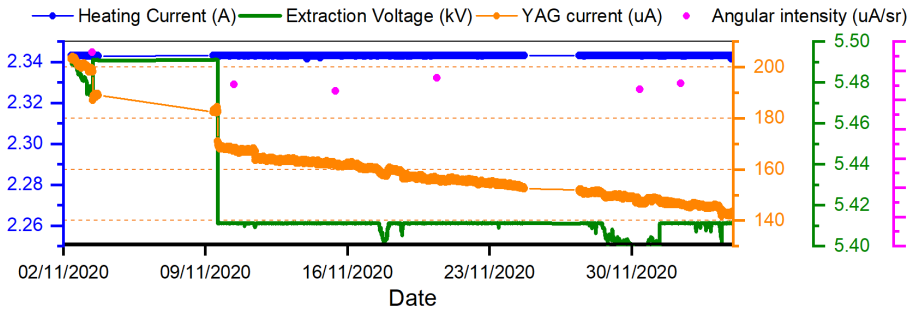


Figure 3.16: The angular intensity and YAG screen current evolution between 02/11/2020 and 5/12/2020. The angular intensity was measured on the optical axis.

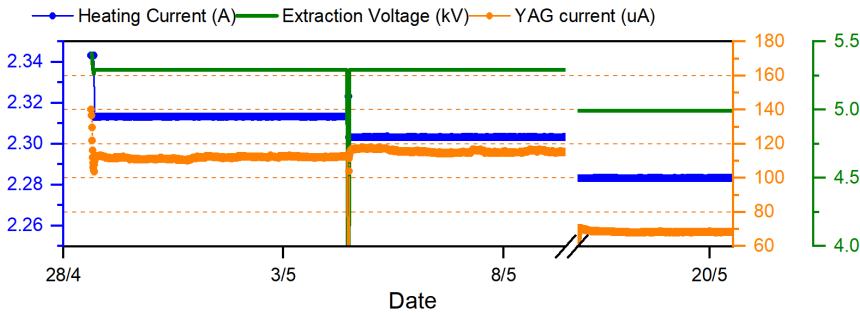


Figure 3.17: The angular intensity and YAG screen current evolution between 28/04/2021 to 21/05/2021, and the suppressor voltage is 400V for the graph to suppress the shank emission.

several times from 02/11/2020 to 5/12/2020. The YAG screen current drops in this period, the dropping speed slowed down somehow.

Figure 3.17 shows the log data from 28/04/2021 to 21/05/2021. The angular intensity in the early period on the graph was 0.81 mA/sr, and the YAG current was very stable for two sections on the graph, indicating a stable emitter facet shape throughout the whole period.

3.5.2 THE SCREEN CURRENT AND THE CENTRAL ANGULAR INTENSITY FOR LONG TERM

After running the emitter for two months, we got the data points as shown in table 3.3. In the beginning, the screen current was higher than the value in the datasheet, but the angular intensity was much lower than the datasheet value. We can see the filament current was increased several times to increase the angular intensity, and the goal of the angular intensity was 1.0 mA/sr. During this process, the screen current decreased.

Table 3.3: The screen current and the central angular intensity on different dates.

		V_{ex} /kV	I_f /A	I_{screen} / μ A	Angular intensity/ μ A/sr
	From datasheet	5.42	2.27	268.2	957.0
1	29/07/2020	5.41	2.26	356.2	594.1
2	07/09/2020	5.41	2.30	345.7	857.4
3	21/09/2020	5.41	2.32	271.0	845.3
4	23/09/2020	5.41	2.34	234.0	908.8
5	03/10/2020	5.41	2.34	220.0	925.9
6	18/10/2020	5.41	2.34	196.0	920.1
7	25/10/2020	5.41	2.34	185.4	938.8
8	28/10/2020	5.49	2.34	211.7	972.9
9	02/11/2020	5.49	2.34	203.2	986.8
10	03/11/2020	5.48	2.34	189.5	931.8
11	10/11/2020	5.41	2.34	167.4	876.9
12	15/11/2020	5.41	2.34	161.3	865.4
13	20/11/2020	5.41	2.34	156.3	887.8
14	30/11/2020	5.39	2.34	146.5	868.2
15	01/12/2020	5.41	2.34	145.8	878.7

3.5.3 THE PROFILES OF EMISSION PATTERNS FOR THE LONG-TERM RUN

Figure 3.18a and figure 3.18b show the profiles of the emission patterns along a horizontal and slant line (as shown in figure 3.7f for total 15 emission patterns (as shown in table 3.3). We can see the fluctuations in the central area are very small, but the fluctuations in the dog ear area are significant, which indicates morphologic changes at the edge of the emitter facet.

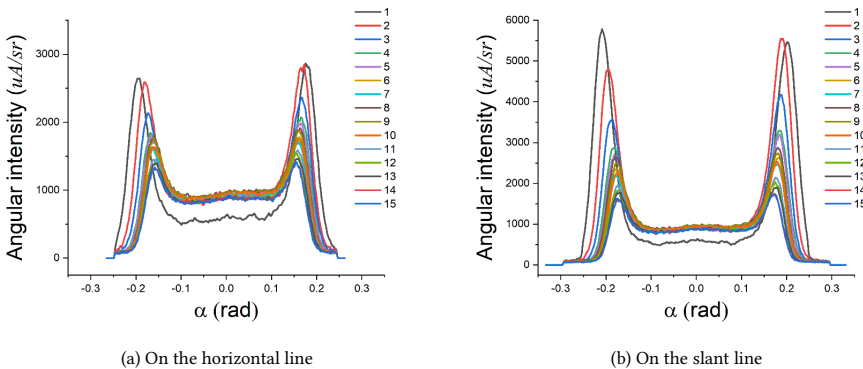


Figure 3.18: Profiles along the horizontal line and slant line in linear scale for 15 emission patterns. Legend is the sequence number in table 3.3.

3.6 FACET SHAPE COMPARISON FOR BEFORE AND AFTER LONG-TERM RUNNING

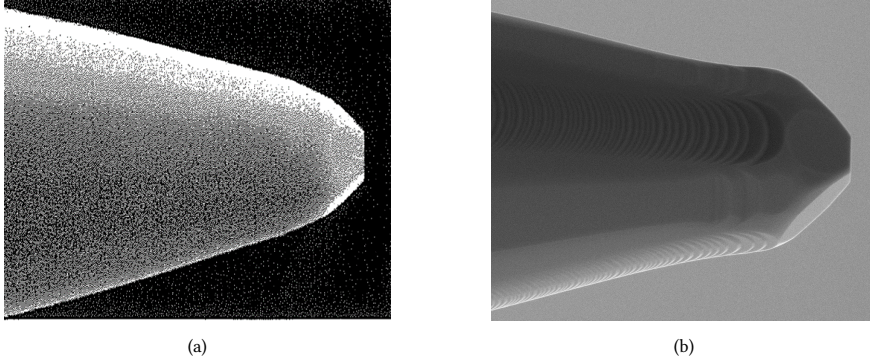


Figure 3.19: SEM photos of the emitter. a. the photo taken in the factory. b. the photo taken after long-term running in our experiment. Two photos are not in the same scale.

Figure 3.19 shows two SEM photos of the emitter used in our experiment. The left photo came in with the datasheet from the Denka, the right photo was taken after the experiment. This emitter was already conditioned for 1 mA/sr emission angular intensity as claimed by the supplier. The emitter shape was convex at the side and with small faces next to the facet before our experiment. After several months running in our setup. The (110) and (101) faces grew larger and there is a necked section next to the side faces, and the configuration is obviously in phase 2 as designated in some literature [46][51].

3.7 CONCLUSIONS

In this chapter, we aimed to achieve 1.0 mA/sr angular intensity for a radius of $1.0 \mu\text{m}$ TFE emitter, and we found it's possible for different emitter temperatures. The current in the dog ear area and emitted from the shank make things complicated, and we need to balance them and choose an intermediate emitter temperature.

From the angular intensity maps, we found that the uniform region could be as large as about 100 mrad from the emission pattern center (optical axis). These should be the physical limitations caused by the TFE source for the multi-beam application. Of course, engineering may give other limits to the range that we can utilize.

We found it challenging to maintain a stable emission at 1.0 mA/sr for a large opening angle from the long-term running curve. The YAG screen current drops all the time though the angular intensity keeps more or less the same, it's because the morphologic changes happened at the edge of the emitter facet in a long-term running, and it's not good for the long-term stability for a multi-beam application which needs current from both the center and off-axial area.

We also found the YAG current could be reasonably stable for the whole emitting facet at 0.81 mA/sr angular intensity. A constant YAG current indicates a stable facet shape without morphologic change or further faceting of the tip, and this is essential for a multi-beam

source that is supposed to work perfectly for a whole year.

We speculate that to obtain a stable 1.0 mA/sr for up to 100 mrad half opening angle, an emitter with slightly larger radius should be chosen.

4

MULTI-BEAM SOURCE EXPERIMENT ON INDIVIDUAL BEAM CHARACTERISTICS

4.1 INTRODUCTION

In this chapter, we will introduce a Multi-Beam Source (MBS) design that can deliver a few hundred electron beams with a few mm pitch and a total current of several μA . Dr. Ali Mohammadi-Gheidari did the electron optic part of this MBS design based on his earlier design [29] of a multi-beam source for 196 beams with $70 \mu m$ pitch and $157 nA$ total current.

We built a setup to verify the optical performance of the MBS design. The beam spot size, size uniformity, grid distortion, and through focus properties will be measured. In addition, different implements of the MBS will be explained, and different aperture lens array patterns will be tested in the experiments.

In section 4.2, we will explain the verification setup of the multi-beam source, and in section 4.3, we will explain two different multi-beam source designs used in the setup. Section 4.5 is about the automatic measurement software written in LabVIEW and the corresponding post-process Python script, and this work was carried out by Dr. Marco Wisse. Sections 4.6 to 4.9 describe several measurements for different configurations of the MBS. And section 4.10 summarizes the results of all the measurements.

4.2 DESIGN OF THE EXPERIMENTAL SETUP

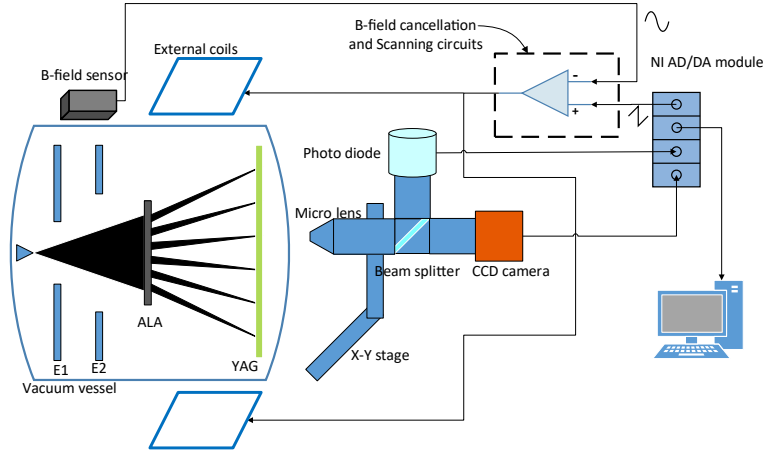


Figure 4.1: Schematic diagram of the multi-beam source characterization setup.



Figure 4.2: The photo of the multi-beam source characterization setup.

As shown in figures 4.1 and 4.2, we designed a setup to characterize the individual off-axial beamlets generated by the MB source. The setup mainly consists of two parts: the MBS assembly in the vacuum and the characterization setup outside the vacuum vessel.

4.2.1 THE MB SOURCE ASSEMBLY IN AN ULTRA-HIGH VACUUM (UHV) VESSEL

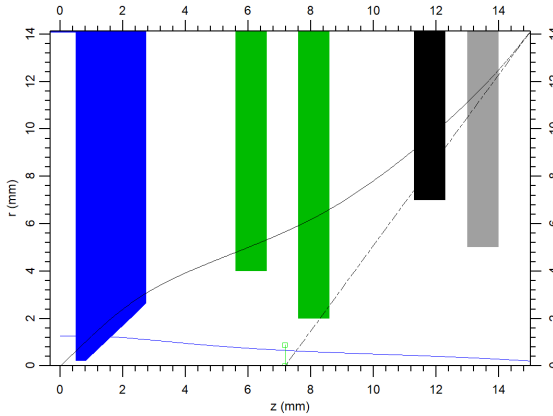


Figure 4.3: Electron optics simulation of the Zero Strength Lens (ZSL) design in the MBS. The blue electrode is an extractor, the green electrodes are called the E1 group, and the black and grey electrodes are called the E2 group. The Aperture lens array (ALA) is located at the $z=15.0 \text{ mm}$ plane.

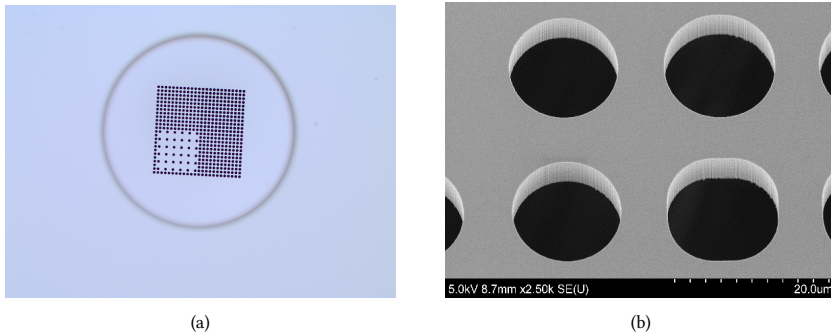


Figure 4.4: The optical microscope image of an ALA wafer (a) and an SEM photo of the ALA wafer (b) that was used in the experiment.

The source part of the setup consists of a gun head flange, a standard Schottky source, an Aperture Lens Array (ALA) after the Schottky source, several electrodes between the extractor and the ALA, and a YAG screen. The latter is the image plane for the focused beams next to the viewport. The ALA is made of a silicon-on-insulator (SOI) wafer with many etched holes (Figure 4.4). It splits the electron beam launched from the emitter into a few hundred beamlets, meanwhile, the ALA will also focus the beamlet at the image plane (YAG screen) because the electrostatic field in front of the ALA makes it an aperture lens array.

Because we use a simulation program that can only do rotationally symmetric systems,

the simulation of a multi-beam source should be done in two steps: zero-strength lens (ZSL) simulation and multi-beam source (MBS) simulation. ‘Zero strength’ means that the off-axis beams are not deflected, thus avoiding the problem associated with chromatic deflection errors. ZSL indicates the regime up to the ALA, where the holes in the ALA are closed. MBS indicates the whole system, including the on-axis aperture lens and the field-free area below the ALA till the image plan.

Figure 4.3 shows a ZSL model in the simulation software EOD [60]. The black and blue curves are the two fundamental ray in the electron optics, and the dash line indicate the virtual source position via back tracing the ray from the ALA plane. In the simulation, the ALA is only a line electrode at the right boundary of the model. Three parameters will be optimized by sweeping E1 and E2 voltages [29] :

1. The spherical and chromatic aberration coefficients of the zero-strength lens C_{S-ZSL} . C_{S-ZSL} should be as small as possible. We will use those aberration coefficients to derive the aberrations in the off-axis beams.
2. The field curvature (FC). The E2 potential can modify the electrostatic field in front of the individual apertures and make the focal length of apertures longer for the edge apertures than the central apertures, such that the images formed by different apertures will be as close as possible to the YAG screen plane.
3. The position of the virtual source. In the simulation of the MBS, the distance between the virtual source and the ALA will shift the effective object position and thus determine the pitch of the beam spots on the YAG screen.

After the ZSL simulation, we will make the axial aperture hole in the model and set the image plane at the YAG screen $z = 300 \text{ mm}$ in EOD software. In this MBS model, we can get the axial aberrations from the EOD simulation. With the method explained in [29], we can combine all the aberrations and evaluate the spot size for all electron beams from the center to the edge.

In our multi-beam source design, the dimensions are shown in figure 4.3, the potential on the E1 group is about 23.4 kV (with respect to the emitter potential), and the potential on the E2 group is 9.0 kV , the potential of the ALA is 5.0 kV , the same as the extractor, the beam energy is 5.0 keV as well. After the simulation, the MBS should deliver tens \times tens beamlets, the spot size on the YAG is about $0.5 \mu\text{m}$, and the pitch between beam spots is a few mm ; the virtual source size is assumed as 25 nm for a $0.7 \mu\text{m}$ radius emitter, the magnification of ZSL M_{zsl} is 0.53 (virtual image), and the magnification of the ALA is 35.63 (real image).

4.2.2 THE CHARACTERIZATION SETUP OUTSIDE THE VACUUM VESSEL.

The characterization setup is designed to verify the performance of the designed MBS and the related manufacturing technology. To this pupose, it needs to measure the exact positions of the focused beams and the current density distribution in the spots on the YAG. The setup is outside the vacuum vessel, and it consists of an XY stage, a digital camera and macro-objective on the stage, a photodiode, a magnetic sensor, a set of small coils near the vacuum vessel, a group of big coils to compensate for the earth magnetic field and a computer with corresponding code made in LabVIEW software.

The movement of the XY stage is 50 mm by 50 mm so that it can cover the whole YAG surface (diameter = 50 mm). During the measurement, the code made in LabVIEW software will drive the XY stage from one spot to another, and the position of spots is pre-defined manually. When the stage moves the camera to one spot, the software will take a photo of the spot and record its position. The spot photos and positions will be post-processed to extract many parameters, such as spot size, spot shape, beam current, angular current density, astigmatism, and other aberrations.

More details will be discussed in sections 4.4 and 4.5.

4.3 THE EMBODIMENTS OF THE MBS DESIGN (MEMS AND CONVENTIONAL STACKS)

4

The electrode stack in an MBS design, like the one mentioned in section 4.2, can be implemented with either MEMS technology or traditional machining of metal technology. Below we will explain both embodiments of implementing an MBS.

4.3.1 THE SOURCE WITH THE MEMS STACK

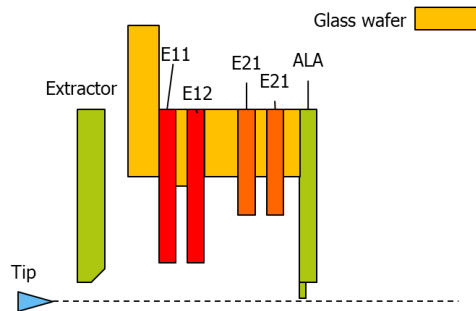


Figure 4.5: The schematic view of the multi-beam source design.

Because MEMS technology can easily produce precise geometries and accurately align lens electrodes [11], we first make the electrode stack with MEMS technology.

Figure 4.5 shows the structure of an MBS made with a MEMS stack. Glass spacers insulate the electrodes and ALA. All the electrodes are aligned on a homemade hexapod aligner, which can align the electrodes within 1 μm tolerance. The electrodes and glass spacers are glued together step by step during the alignment. The whole stack has a big glass wafer as a base (c), which will be glued to a metal plate (b), and the metal plate will be mounted to a gun flange (a) in the end (see figure 4.6).

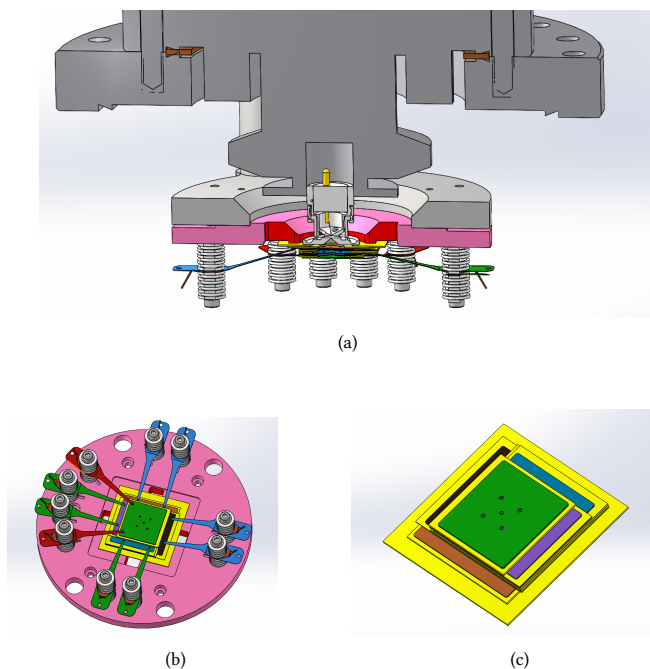


Figure 4.6: The 3D drawings of the multi-beam source design with a MEMS stack.

4.3.2 HV INSULATION ISSUE IN THE MEMS STACK AND ATTEMPTED SOLUTIONS

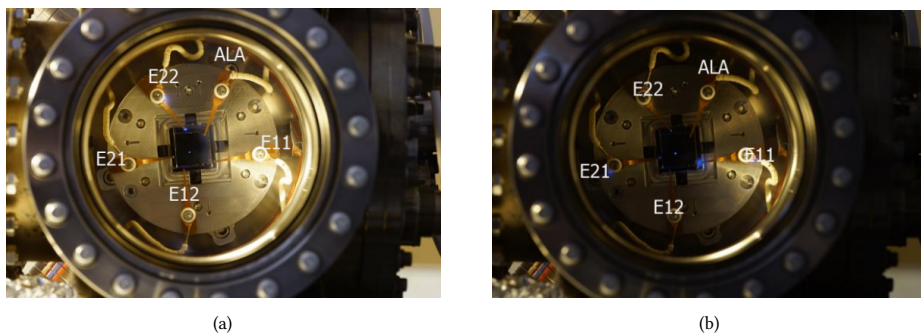


Figure 4.7: Glows (blue light in the vacuum chamber) appeared at several places in the stack when the high voltages were applied.

Because the MEMS stack is very compact, the high voltage insulation is sometimes challenging. To study these discharges, we put the flange in a separate vacuum setup in which the MEMS stack is visible. In figure 4.7, we can see some blue glows, which indicate discharging in these areas. The discharging at the stack usually causes surface flashovers if we increase the voltage on the pins. At most, this stack can hold about 12-14 kV with

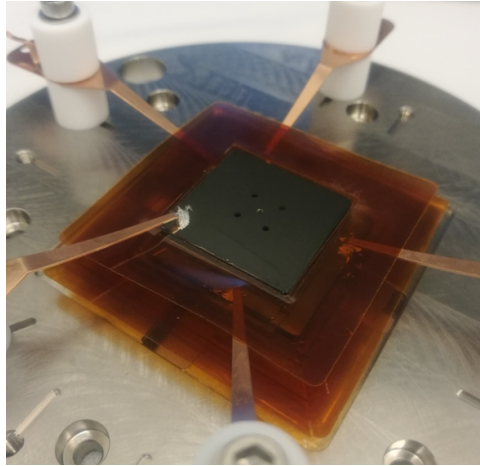


Figure 4.8: Kapton sheets are added to the glass spacer to enhance the insulation on a dummy stack.

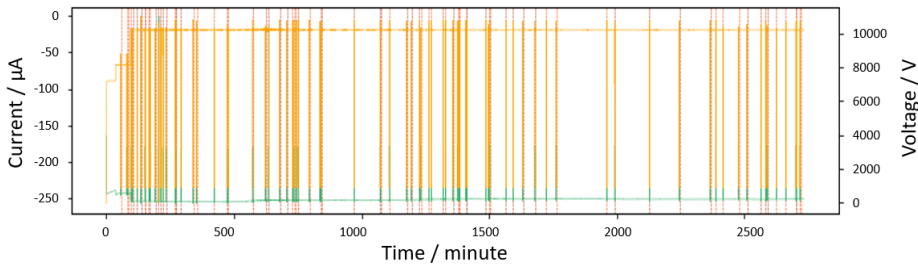


Figure 4.9: The voltage and current curves recorded in the conditioning procedure.

respect to ground on the E1 group. For this voltage on the E1 group, the maximum beam energy that can be focused on the YAG screen is 4 keV . Therefore, we need to do some high voltage conditioning under certain protection of the emitter.

To protect the emitter, we made software that can monitor the parameters of the emitter and vacuum pressure at the same time. When the vacuum pressure ramps up to a threshold, like $5.0 \times 10^{-8} \text{ mBar}$, the software will switch off the power supply of the emitter to limit the damage to the emitter. To suppress the surface flashover, we tried putting some Kapton sheets on the glass spacer (figure 4.8). We connected the E1 group to the HV tester and grounded all the other electrodes; after about 30 hours of conditioning, the frequency of discharge decreased (figure 4.9) at a voltage of 10 kV . By comparison, the same stack could not even hold 8 kV before adding the Kapton sheet.

Kapton sheet can help with the HV insulation, but in our trial, it's not sufficient to eliminate the discharge thoroughly, which is essential to a Schottky emitter.

4.3.3 THE SOURCE DESIGN WITH THE CONVENTIONAL STACK

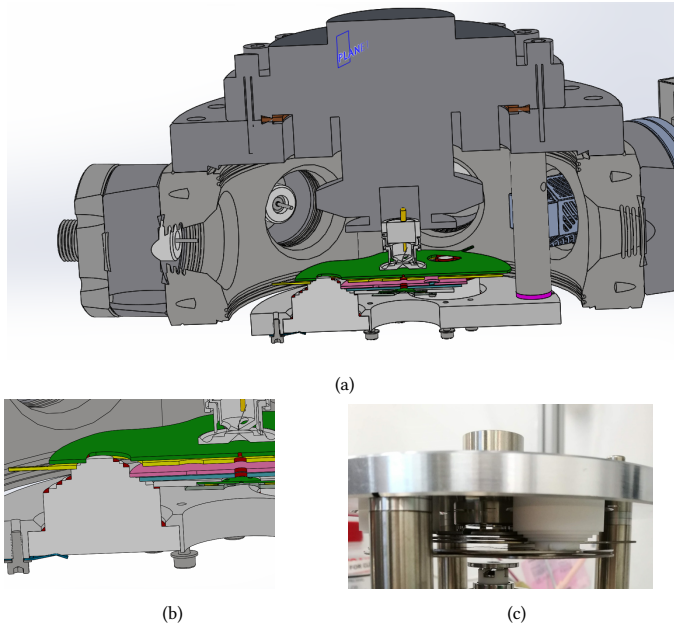


Figure 4.10: The drawings of the stack, which is made in a conventional way. a. The section view of the MB source with a conventional stack. b. An enlarged view of the insulation pillar and electrodes sitting on it. c. the photo of the MB source with a conventional stack taken during assembling.

An MBS design with conventional metal electrodes and MacorTM insulators and a picture taken during the assembling are shown in figure 4.10. The electrodes are made of titanium, and they are located on the different steps of 3 MacorTM pillars. The 3 MacorTM pillars are mounted on a metal plate, which in turn is mounted on the gun head flange with 3 rods. The steps on the MacorTM pillars are designed such that the creepage distance for all the electrodes is more than the value calculated by the 1.0 kV/mm constraint, so the chance of surface flashover is very low.

After some HV conditioning¹, this stack can hold voltages of about 21 kV with respect to ground on the E1 group, which is enough to focus the electron beam of 5.0 keV energy. figure 4.11 shows the shadow image of the 4.0 keV electron beam and the focused beam spots on the YAG screen. The ALA wafer is shown in figure 4.4, with the 4-quadrant pattern. The pattern of the ALA is explained in detail in section 4.7.

¹The conditioning here indicates applying a proper high voltage to the electrodes in a non-destructive way for a while, and a better insulation performance can be achieved after several flashovers.

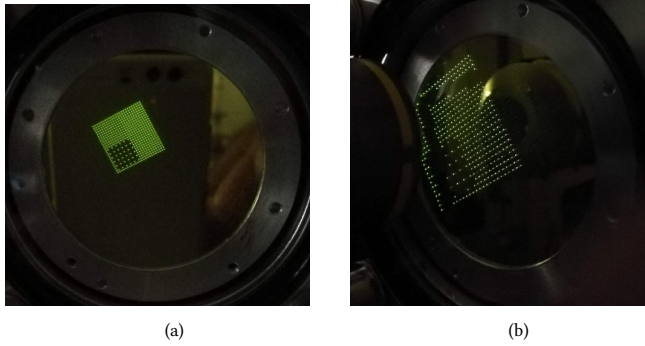


Figure 4.11: Electron beam photos of the MBS with conventional stack are taken from a cell phone camera, a. the shadow image of 4 keV beams. b. focused beam spots of 4 keV beams. The tungsten square border on the YAG causes the black stripe in photo b.

4.4 CCD IMAGE ACQUISITION AND KNIFE-EDGE METHODS

There are two basic methods for the measurement of the spot size and spot shape on the YAG screen, one is the direct CCD image acquisition, the other is the knife-edge scan method. Figure 4.14 sketches the imaging system on the setup. The imaging system consists of an optical microscope and a photodiode. The optical microscope is mounted on the linear x-y stage with a 50 mm travel range in both axes (figure 4.12). The stage is driven by stepper motors. The optical system is controlled by a control box whose code is written in LabVIEW.

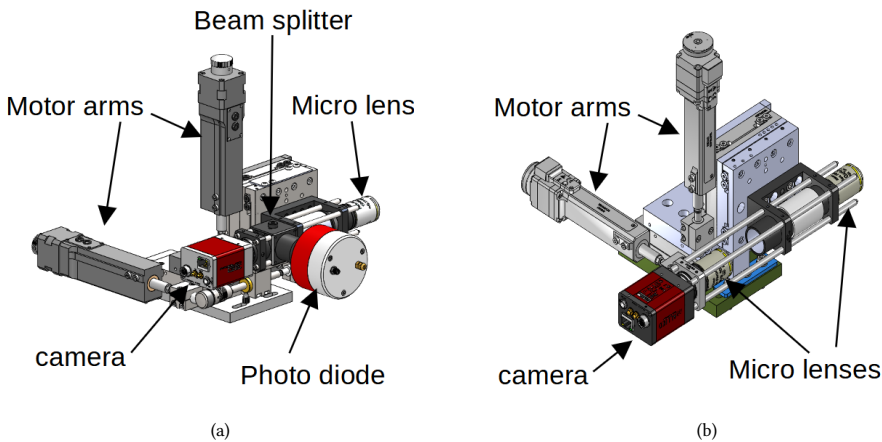
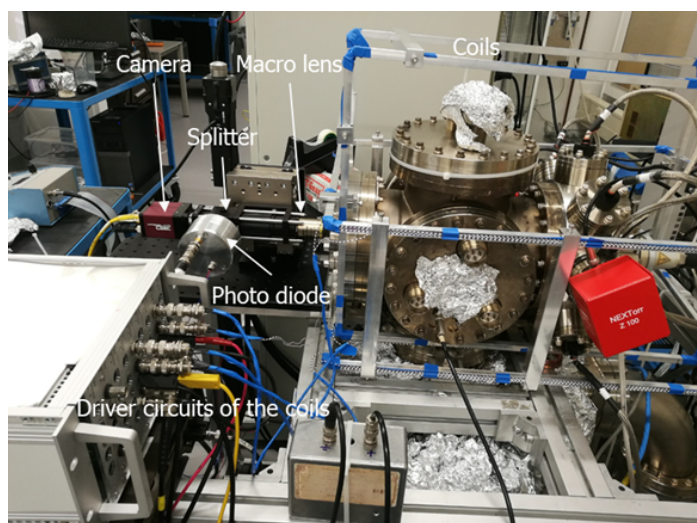


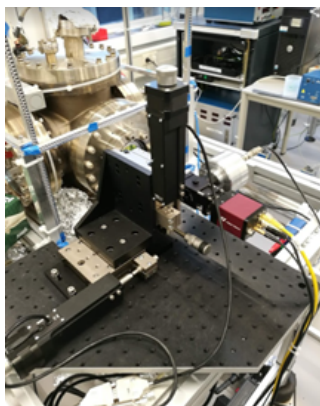
Figure 4.12: Two variants of the X-Y stage, which holds the optical system. a. The optical system is combined with a photodiode detector. b. the optical system has two Nikon objectives and has higher magnification.

As shown in figure 4.14, electron beams hit the YAG screen at $z=300\text{ mm}$, which has a tungsten grid on the electron-incident side and is additionally coated with a layer of

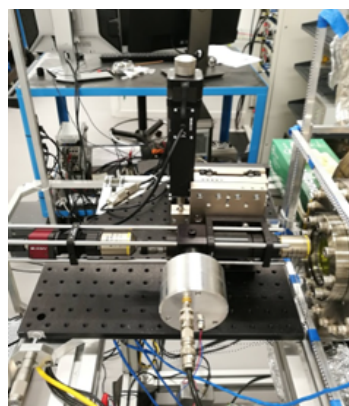
aluminum to avoid charge accumulating on the YAG surface. This YAG screen is close to the viewport and will convert the electron beam into an optical signal. A Nikon objective lens (WD=16 mm, NA=0.3, Mag=10 \times) and camera (Allied vision GE680) are used to capture the light signal. A beam splitter (figures 4.1 and 4.13) is located after the Nikon objective. One beam is directed through another objective lens which focuses the light beam onto the GE 680 camera, while the other beam travels towards the photo-diode detector (Hamamatsu MPPC C13365-3050SA).



(a)



(b)



(c)

Figure 4.13: The photos of the real setup. a.the X-Y stage with the vacuum chamber, small coils, and its driver circuits. b. the photo of the X-Y stage with and lens combined lens and photodiode. c. another view of the X-Y stage.

The resolution of this microscope is mainly limited by diffraction, which is often expressed with respect to the full width at half maximum (FWHM) of the intensity profile

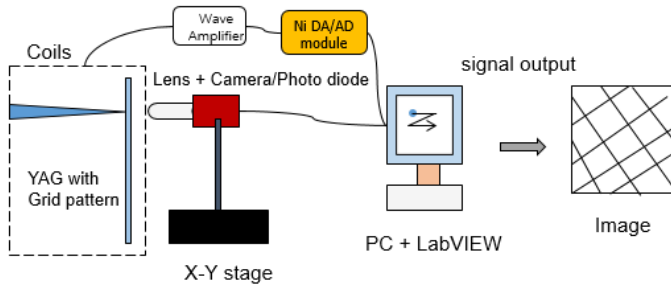


Figure 4.14: The schematic diagram of the imaging system in the setup.

[61][62],

$$d_{FWHM} = 0.51 \frac{\lambda}{NA} \quad (4.1)$$

where λ is the wavelength of the light, and NA is the numerical aperture of the objective of the microscope. The mean wavelength of the light generated from YAG:Ce is 550 nm , and the NA of the Nikon objective is 0.30 , hence the limit in resolution of the microscope due to diffraction is approximately $0.94 \mu\text{m}$, which is sufficient for our application, where we expect spot sizes of about $1.0 \mu\text{m}$ for an emitter of $1.0 \mu\text{m}$ radius.

Besides photography with the camera, the knife-edge scanning method is another approach

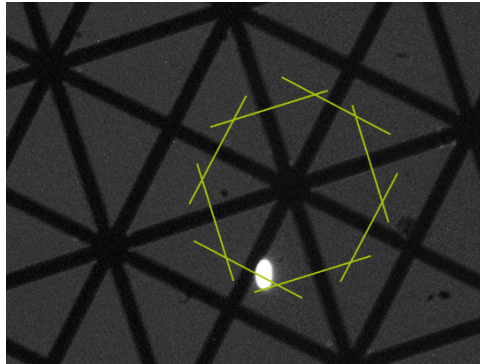


Figure 4.15: The microscope photo of the tungsten line on the YAG (illuminated by an electron beam spot).

to measure the spot size and shape. Around the vacuum vessel, two sets of coils are placed perpendicular to each other and to the beam. These coils fulfil two functions: firstly, one is able to cancel the 50 Hz electromagnetic noise from the environment with dedicated circuits, secondly, one can scan the spots over the sharp edge of the tungsten grid line, the intensity will be detected by the photo-diode detector. Because the edge of the tungsten line is very steep, about several nm width over 200 nm in height, the blur of the edge in the image acquired by the photodiode detector is only caused by the electron beam size.

We can use a 12%-88% definition, like some SEM images, to represent the spot size. If we scan the lines in different directions (figure 4.15), we will also measure the width of the spot in different directions. Therefore, we can get the shape information of a beam spot.

4.4.1 50 Hz ELECTROMAGNETIC NOISE

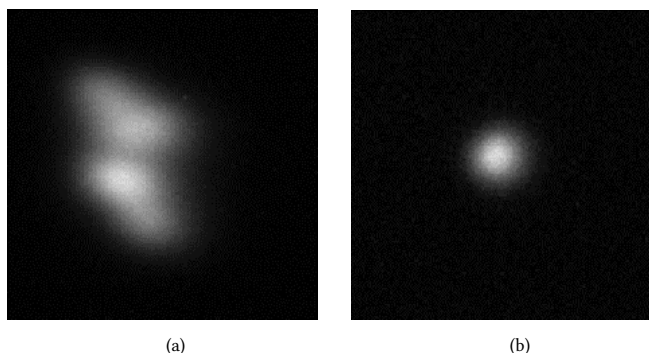


Figure 4.16: The spots were taken with 30 ms (a) and 3 ms (b) exposure time, respectively.

During the experiments, we found that the spot shape could be strange under certain camera conditions (graph a in figure 4.16), which turns out that it is caused by the mains 50 Hz electromagnetic (EM) noise. The period of 50 Hz is 20 ms; when we set the exposure time that is longer than 20 ms, the camera will take an image of the whole trace of the spot scanned by the periodic noise. When we set the exposure time much shorter than 20 ms, e.g. 3 ms, we are able to capture a clear spot on the camera (graph b in figure 4.16).

The vacuum chamber of our setup is made of stainless steel, which cannot shield the low frequent EM noise. One approach to suppress the 50 Hz EM noise is generating another EM field, which has the same amplitude as the ambient field but the opposite phase of the ambient field. Similar work has been done several times in our group, and figure 4.17 shows some information about an experiment carried out in 2015 [63]. The purpose is to reduce the magnetic fields around an SEM from up to 300 nT (50 Hz and 150 Hz harmonics) to 30 nT and compensate for the earth's magnetic field (45 μ T). Because of the magnetic shielding of the SEM, the magnetic field inside the chamber will be lower than 1 nT. The setup (figure 4.17) consists of three sets of Helmholtz coils placed in a cage. A magnetic field sensor is placed inside the cage around the SEM, which measures the magnetic fields. A controller is used to reduce the fields and power up the coils. Helmholtz coils are a pair coils of equal size with a distance of their radius, which thus, create a homogeneous magnetic field between them. The SEM will be placed in this homogeneous area. The coils used for that work are 2 by 2 meters and have 30 windings.

The experimental results of the work in 2015 were not very successful, and the authors concluded two possible reasons:

1. The SEM chamber is made of ferromagnetic material for good shielding but would distort the field around it.
2. The design of the controller needs to be improved.

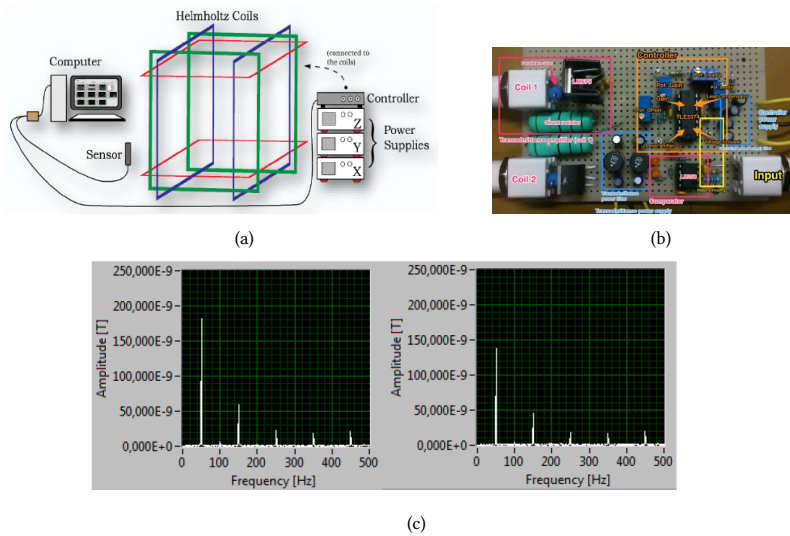
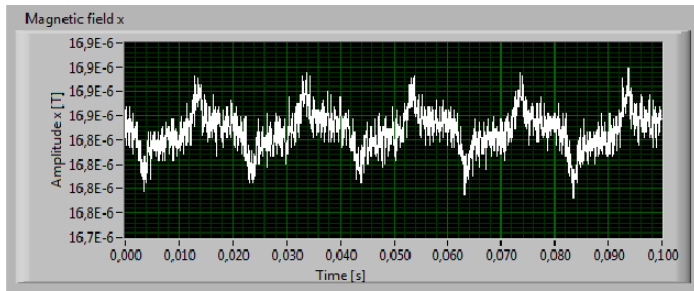


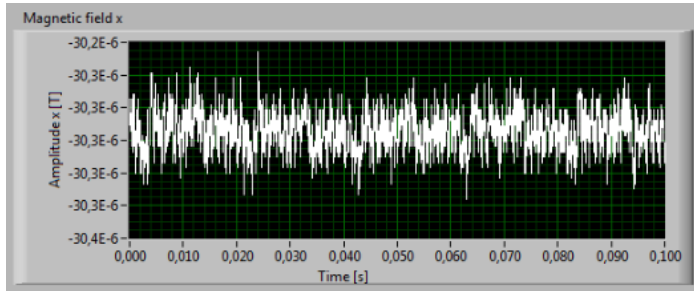
Figure 4.17: The attempt to cancel 50Hz EM noise made before in our group. (a). The schematic overview of the compensation system was made in 2015 in our group. (b). The driver circuits of the controller. (c). the spectrum of the background EM noise with the FFT method.

Based on the research made in 2015, we made some improvements. First, we made two sets of smaller rectangular coils (figure 4.17), 56 cm by 38 cm, which just fit our vacuum chamber and can generate a sufficiently homogeneous field area. These coils have smaller impedance, and therefore, they are much easier to drive by the circuits. Secondly, we made new drive circuits and limited the frequency to 150 Hz to suppress the noise of the circuits. We left the two large coils to only compensate for the earth magnetic field with general DC power supplies. All the measures turn out sufficient to reduce the magnitude of the 50 Hz harmonic from 16 nT to 2 nT (figure 4.18), which is sufficient to have a static spot on the camera for the live view mode.

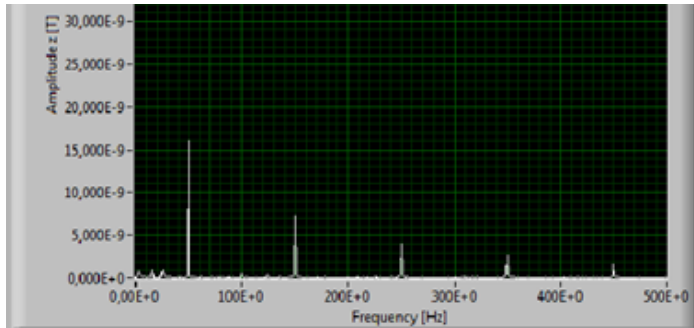
Unfortunately, we found there was still a non-periodic and very low-frequency disturbance after we reduced the 50 Hz noise. Therefore, we decided to synchronize the camera and photodiode to the 50 Hz magnetic field by a Transistor-Transistor Logic (TTL) pulse generator. The generator can generate the TTL pulses with the same phase as the 50 Hz wave in the mains. The sampling rate of the photodiode then also has to be 50 Hz, which makes the knife-edge scanning method slower than the direct CCD method when measuring the spot size and spot shape. Therefore, we decided to use the CCD method for the measurement as much as we could.



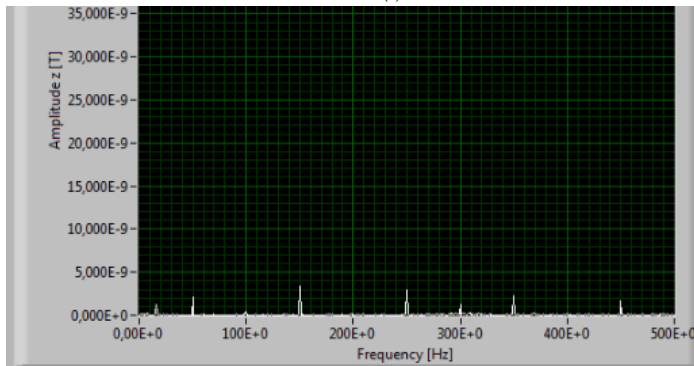
(a)



(b)



(c)



(d)

Figure 4.18: The new circuits' effect after tuning the course parameters. a. the EM wave without noise cancellation. b. the EM wave with the noise cancellation. c. the spectrum of the EM wave in a. d. the spectrum of the EM wave in b.

4.5 PRINCIPLES OF THE AUTOMATIC MEASUREMENT: LABVIEW SOFTWARE AND POST-PROCESS PYTHON SCRIPTS

Since we have a few hundred beam spots on the YAG screen to be measured, it is necessary to automate the measurement, otherwise, the action will be time-consuming. Therefore, we decided to write measurement software in LabVIEW, for which many module suppliers provide drivers. Dr. Marco Wisse wrote the corresponding software in LabVIEW and wrote the original post-process Python script. Below is a brief explanation from a user's point of view.

We need to define spot locations for four corners for the LabVIEW program, and then the software generates locations for all the beam spots together with the row number and column numbers we set in the program, assuming they are in a good grid. To number the grid, we followed the Python tradition, counting from 0, from left to right, and from top to bottom; the row number is in front of the column number for a 2-dimension grid. For example, the coordinates of the top-left corner, top-right corner, bottom-left corner and bottom-right corner are (0, 0), (0, 22), (22, 0), (22, 22), respectively, for a 23 by 23 grid.

After defining the grid, the camera moves row by row from the top left to the top right, then the second row. For every spot, the camera is at a fixed location and one scans over the voltage range (from under-focusing voltage to over-focusing voltage) over the focusing electrodes with a certain interval, which is defined by us in advance. For every voltage, the camera will take a 12-bit image and save it to a folder. Because of the misalignment, the spot moves out of the center of the camera during scanning voltage, then the LabVIEW program can determine the displacement and move the camera back to the spot center by applying the proper current in the small coil set.

After we go through all the beam spots, we can collect all the photos for a through focus series. The Python scripts are made to do the post-processing. First, one script will figure out the brightness center of a photo and crop it for a smaller size. Then another script will analyze all the cropped photos and extract some parameters, like full width 50 (FW50) [20], smallest width out of focus, and so on. More explanations of these parameters will be described in the next sections. Finally, a script is made to plot all the parameters. The original Python scripts were made by Dr. Macro Wisse, but some of them were modified by the author according to the different situations and requirements we had.

For a round spot with a Gaussian profile, the full width at half maximum (FWHM) is a proper parameter to describe the probe size, and it is easy to acquire with most software. Therefore, it is often used. However, for a non-Gaussian profile, the FWHM is not suitable for the beam size [20][64]. The diameter containing a fraction of the current is always important and not related to the assumption of the beam profile. Therefore, the full width 50 (FW50), which means the diameter within which 50% of the beam current is found, will be adopted in most graphs, determined in the post-process Python scripts, where the brightness is taken as current density. Of course, for a round beam with a Gaussian profile, FWHM equals FW50.

4.6 MEASUREMENT FOR THE REGULAR ALA

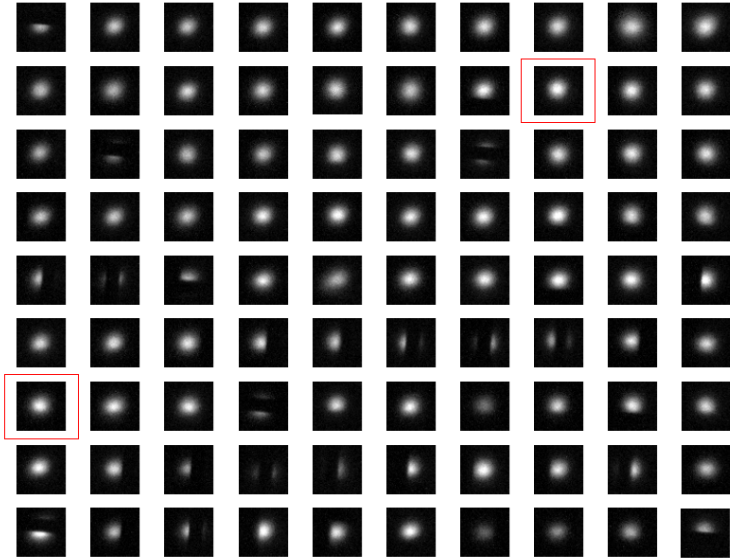
We first did some measurements for the source with the MEMS stack. Because of the high voltage flashover issue, the MEMS stack could not hold sufficiently high voltages on the E1

Table 4.1: Voltage (with respect to ground) configuration in the simulation and experiment

	PE /kV	E1 /kV	E21 /kV	E22 /kV	ALA /V	Pitch /mm
EOD simulation	4.0	12.1	3.0	2.7	0	1.60
Measurement	4.0	12.4	3.0	2.7	0	~1.62

electrodes to focus a 5 keV energy beam. We applied the voltage configuration as shown in table 4.1 and focused the electron beam of 4 keV energy at the YAG screen. We had a modified vacuum chamber for this experiment, so the distance from the emitter to the YAG screen was 460 mm .

The automatic measurement system was not yet made at that moment, therefore, we did manual measurements. All the results in this section are acquired manually. First, we took photos of the electron beam spots of 9 rows by 10 columns. They are shown in figure 4.19. Some of them are obscured by the tungsten lines. Statistically, most of them are all in a round shape and have similar brightness and size. Two beam spots are taken out to make profiles (figure 4.20). The pixel size in figure 4.20 is $0.7\text{ }\mu\text{m}/\text{pixel}$. The full width at half maximum (FWHM) of all spots is about 15 pixels . Therefore, the beam size of these two spots is about $10\text{ }\mu\text{m}$ in the measurement.

Figure 4.19: Photos of 9×10 electron beams on the YAG screen.

Assuming the virtual source size is 50 nm for a $1\text{ }\mu\text{m}$ radius emitter, and the distance from the emitter to the YAG screen is 300 mm , for an optimized voltage configuration, the simulated beam spot size is about $1\text{ }\mu\text{m}$. Because the distance from the emitter to the YAG

screen is 460 mm in this measurement, the spot size should be 1.5 times larger, about $1.5\ \mu\text{m}$. There are still three possible contributions to the larger measured spot size,

1. The voltages in table 4.1 are not optimal for the system.
2. The emitter encountered several flashovers before the measurement, and its virtual size could be larger than 50 nm .
3. The other aberrations.

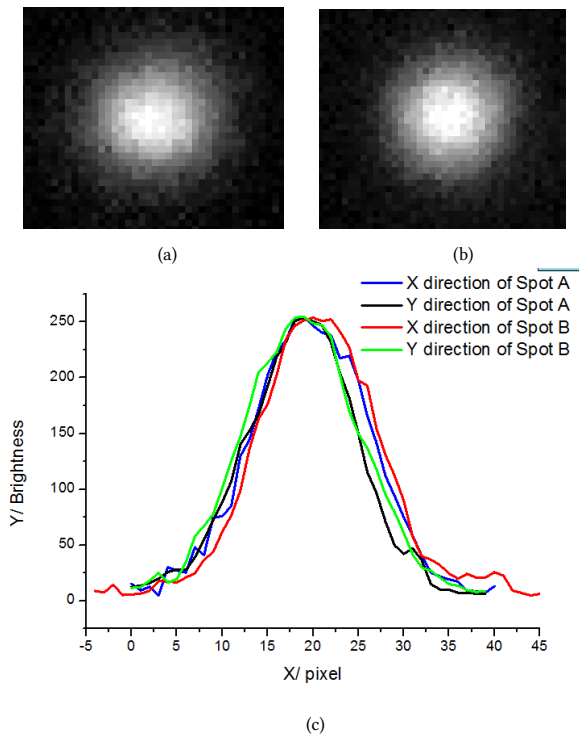


Figure 4.20: Two beam spots from figure 4.19 and their profiles. (a). the beam spot in the left red box. (b). the beam spot in the right red box. (c). the profiles of these two spots in x and y directions.

Besides the photos, the positions of the beam spots are also recorded and displayed in figure 4.21. Their positions match the grid of 1.62 mm intervals quite well. Only at the top right corner and left bottom corner, some spots deviate from the grid. Since this deviation doesn't happen at the other two corners, we think the misalignment between the YAG screen and the X-Y stage movement causes this distortion. Therefore, we conclude that the source has very little distortion.

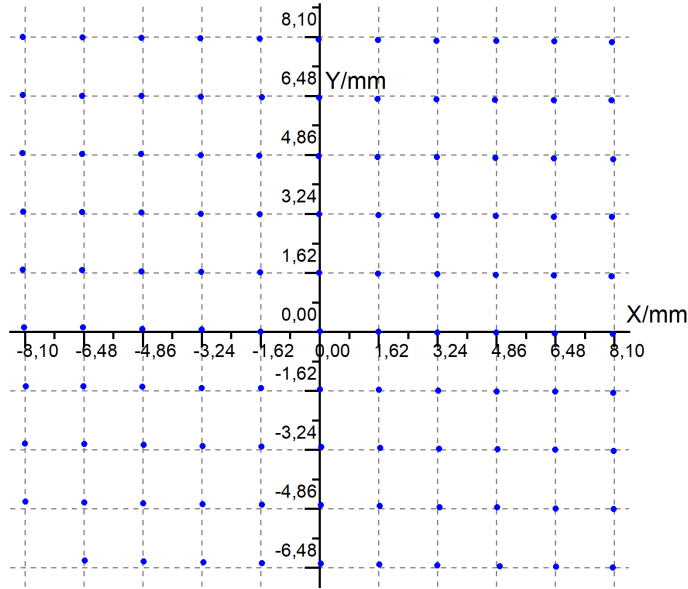


Figure 4.21: Positions of 9×10 electron beam spots on the YAG screen

4.7 MEASUREMENT FOR THE 4-QUADRANT ALA

During the experiment, we noticed that when the electron beam is under-focused or overfocused by several hundred volts, the shape of the electron beam is a cross instead of a round spot, and the orientation of the cross rotates by about 45° when going through focus (see figure 4.22). This is the typical behaviour of an octupole field. Our simulation in GPT [65] confirms this is caused by the influence of the neighboring apertures on the ALA. More details about the simulation have been published [66].

There are several ways to suppress or eliminate this octupole effect [67], for example, when the apertures are in a hexagonal pattern, the symmetry does not allow an octupole effect, the twelve-pole effect that can be expected in that case will probably be weaker. Another approach is to make a special shape of the aperture to compensate for the influence of the neighbors., The last way is to make the pitch larger to reduce the influence of neighboring apertures, but this will reduce the total number of apertures within a certain emission angle.

We decided to take advantage of the MEMS technology, which can make specific shapes of the aperture in an accurate way. Thereby the aperture with a dedicated shape can generate an opposing octupole effect that cancels the octupole effect from the surrounding apertures.

The stack in the MBS of this experiment is made of titanium electrodes and MacorTM insulators, as already described in section 4.3.3.

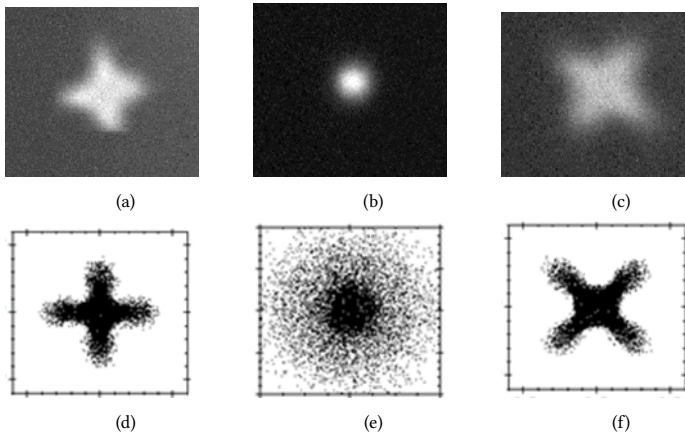


Figure 4.22: The 8-pole effect is noticed when the electron beams are out of focus and are confirmed with simulation [66].

4.7.1 THROUGH FOCUS SERIES FOR 4-QUADRANT ALA

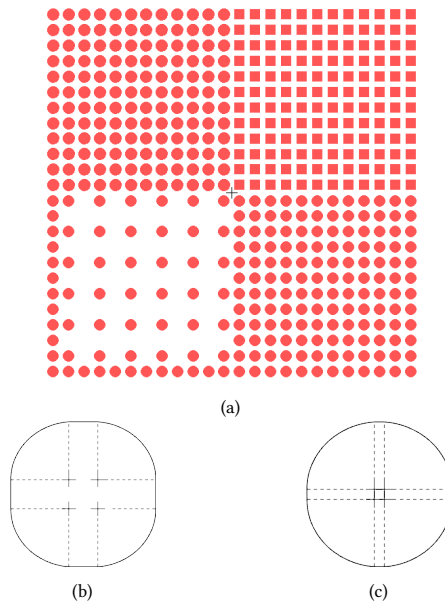


Figure 4.23: A 4-quadrant ALA is designed to investigate the 8-pole effect and optimal shape of the aperture. a. the complete 4-quadrant ALA design in a schematic view. b. overcompensated shape (not in scale). c. the optimized shape of the aperture (not in scale).

Figure 4.23 shows a 4-quadrant ALA design that is used to investigate the octupole effect. A 12×12 matrix in every quadrant (except for the bottom left quadrant) represents one hundred beams in a ten by ten matrix, and the beams at the edge line are used to minimize

the edge effect. In the top left quadrant, the apertures are round and have the same diameter and pitch as the original ALA, they are used as a reference for the test. In the bottom left quadrant, the apertures have the same diameter but the double pitch of the original ALA, they are used to see how the octupole effect drops for a larger pitch. In the top right quadrant, the apertures have the original pitch but a different shape (figure 4.23 b) from the round aperture, which's shape can be seen as a combination of 4 apertures with displaced centers by $1.2 \mu\text{m}$. Thereby an overcompensation of octupole effect is generated. In the bottom right quadrant, the apertures have the same pitch as the original ALA, while the shape is also a combination of 4 apertures, but the displacement of the 4 apertures is $0.4 \mu\text{m}$, which, according to the GPT simulation [65], will eliminate the octupole effect and the FW50 value in this quadrant will be 65% of the value of a spot in the non-corrected quadrant (top-left quadrant).

4

A new ALA chip is made following the concept of figure 4.23. After assembling the source with this ALA and the HV conditioning for several days, we switched on the source and got the shadow image of the ALA on the YAG screen. Figure 4.24 shows a stitched image of all the shadow images of the ALA, with an un-focused electron beams. Since the diameter of a shadowed spot is more than $300 \mu\text{m}$, the tungsten grid ($10 \mu\text{m}$ width) on the YAG screen can be seen in the shadow images.

We also focused the beam spots on the YAG screen, which is at $z=285 \text{ mm}$ in this experiment,

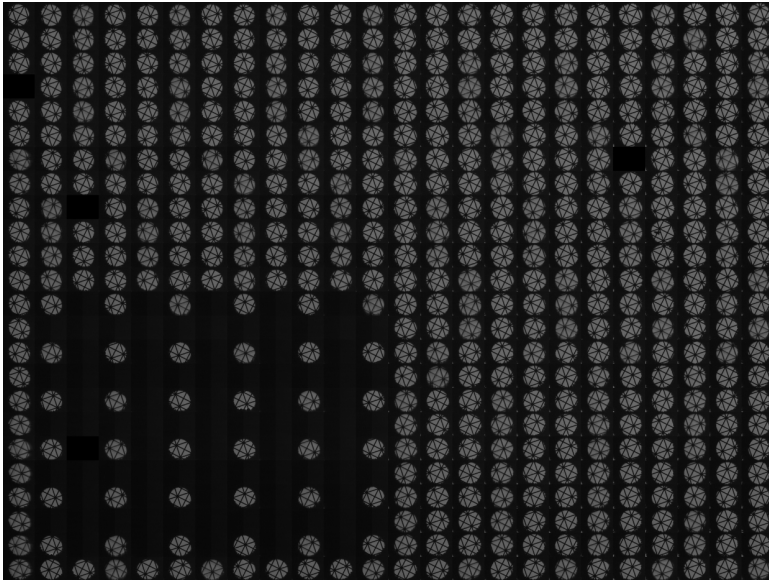


Figure 4.24: The stitched shadow image for the 4-quadrant ALA. The feature within the spots is the tungsten lines made for the knife-edge scan measuring.

because the vacuum chamber was changed from the last experiment, and the beam spot size should be about $1.0 \mu\text{m}$ according to section 4.2. We applied conditions as shown in table 4.2 to the source except for the E1 group electrodes and swept voltage on the E1 group electrodes to focus the electron beams on the YAG screen. Figure 4.25, figure 4.26, and

Table 4.2: The source conditions used for the experimental measurement.

Filament Current/A	Filament temperature /K	Extractor voltage /kV	E2 group voltage /kV
2.33	1810	5.0	3.0

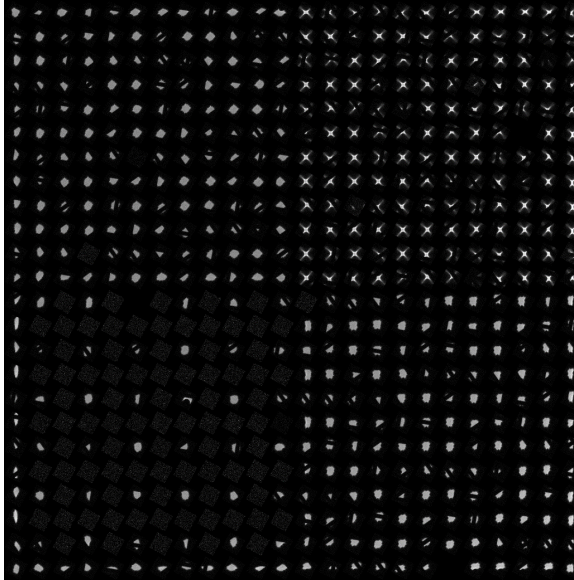


Figure 4.25: The stitched image for under-focused electron beam spots when the E1 group electrodes are at 19.0 kV.

figure 4.27 show the stitched image on the YAG screen for E1 voltage at 19.0 kV, 20.5 kV, and 21.5 kV, respectively. All the photos are rotated before stitching because the pattern of spots is not horizontal. When the camera did not capture a bright spot for some positions, it raised the noise level and generated grey squares, as seen in figure 4.26 and figure 4.27. In table 4.3, the central spots in the four quadrants are shown in more detail under three different E1 voltages. Different shapes for the under-focused beams (E1 voltage = 19.0 kV) are shown in the first column; the spot in the top left quadrant (original shape and pitch quadrant) has a diamond shape, which is the result of the octupole effect. The spot in the bottom left quadrant (original shape and double pitch quadrant) shows a rounded diamond, which indicates less octupole effect for the double pitch pattern. The spot in the top right quadrant shows the obvious shape of a starburst, which indicates a too strong octupole effect generated by the squarish shape of the aperture. The spot in the bottom right quadrant is half obscured by a tungsten line. In the second column (E1 voltage = 20.5 kV), all the spots are almost focused and too tiny to distinguish the shape. A more detailed description follows in the next section. In the third column (E1 voltage = 21.5 kV), all the spots are over-focused. The top quadrants show the typical effects of the octupoles. The spots in the bottom quadrants are not quite round, perhaps by astigmatism.

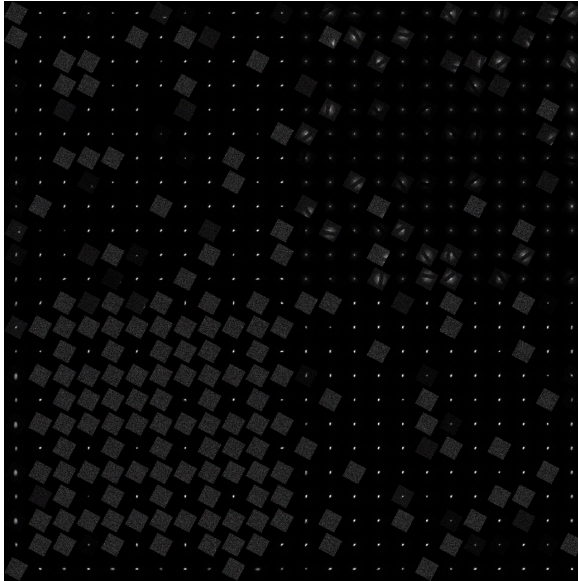


Figure 4.26: The stitched image for under-focused electron beam spots when the E1 group electrodes are at 20.5 kV.

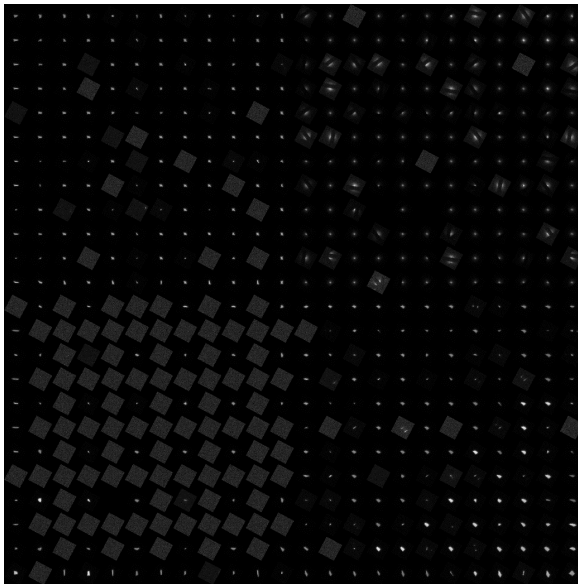


Figure 4.27: The stitched image for over-focused electron beam spots when the E1 group electrodes are at 21.50 kV.

Table 4.3: The under-focused, focused, and over-focused 5.0keV electron beam spots from different quadrants on YAG

E1 group voltage / kV	19.0	20.5	21.5
Top left			
Bottom left			
Top right			
Bottom right			

4.7.2 HIGH MAGNIFICATION (×20) THROUGH FOCUS SERIES.

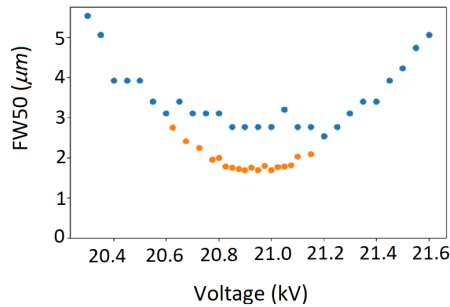


Figure 4.28: The measurement result made by direct CCD image (blue dots) and knife edge scan method (orange dots) for a spot in the top left quadrant. The voltage on the horizontal axis is the E1 group voltage.

We made both CCD image measurements and knife-edge scanning measurements using the methods described in section 4.4. In figure 4.28, we can see the curve measured by the CCD image, pronounced a flat bottom, while the knife-edge scanning method offers a better resolution. Because of Nyquist theorem and the feature of a digital image, the smallest feature can be seen in a digital camera is about 4 to 5 pixels [68], the pixel size for this figure is about 0.7 μm/pixel, therefore, the CCD image can only measure a feature down to about 2.8 -3.5 μm, not to the diffraction limit (0.94 μm) yet. The measuring ability of the system can be increased by increasing the magnification of the optical system. Since the CCD imaging method is faster, we decided to improve it. From the calibration, we find the magnification from YAG to the camera is about 10 times for one Nikon macro-objective, thus, we put another identical Nikon macro-objective to magnify the image of the first

objective (figure 4.29). The calibrated optical magnification from the YAG screen to the camera sensor is then about 20 times.

With this high-magnification optical system, we can now acquire the through-focus series

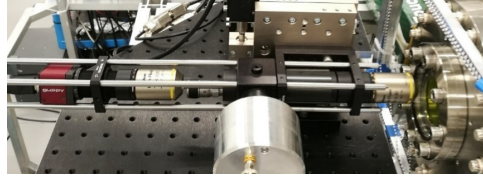


Figure 4.29: The optical system of two macro lenses with the total optical magnification of 20 times.

4

of the beam spots. Figure 4.30 shows the analysis of 4 central spots from 4 quadrants, the coordinates of the spots are as explained in section 4.5. From this figure, we found several results:

1. The spot shape in the top right quadrant is too odd and doesn't show a clear trend, and we will skip this quadrant in the next sections.
2. The minimal values of the other 3 spots don't appear at the same focusing voltage. This could be caused by the field curvature, different aperture lens strength, or a combination of the two.
3. The spot in the bottom left quadrant has the smallest spot size.

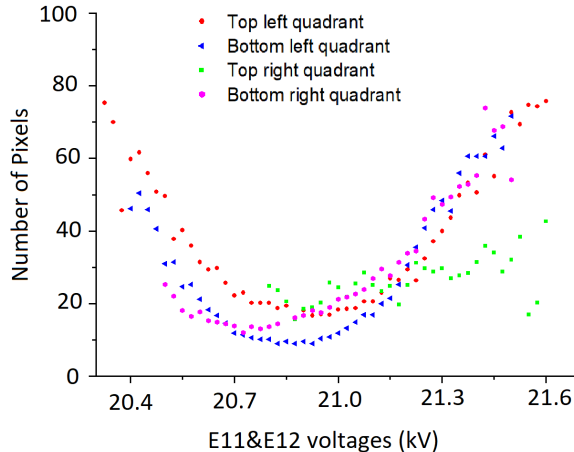


Figure 4.30: The number of pixels that are above the half maximum brightness for beams from 4 quadrants, respectively. The coordinates of these 4 spots are (6,6) (16,5) (6,17) (17,17).

Compared to the spot in the quadrant with the ideal shape, the spot in the double-pitch quadrant (bottom left quadrant) has a smaller spot size. We believe that the shaped aper-

ture’s octupole field is extremely sensitive to the shape’s dimensions, making it challenging to compensate the octupole field produced by nearby apertures.

The enlarged view of the three spots in the individual-focused situation is shown in figure 4.31, and their profiles are shown in figure 4.32 We get the effective pixel size in the plane of the YAG screen of about $0.35 \mu m$ from the calibration on the YAG screen. After fitting a Gaussian function and converting the unit from pixel to μm , we receive the FWHM given in table 4.4, and the FWHM value of the central spot in the double-pitch quadrant of $2.8 \mu m$. Abbreviations in the table are: T: top, B: bottom, L: left, R: right. V: vertical, H: horizontal.

In fact, we see clear astigmatism in the through-focus series of the central location in the

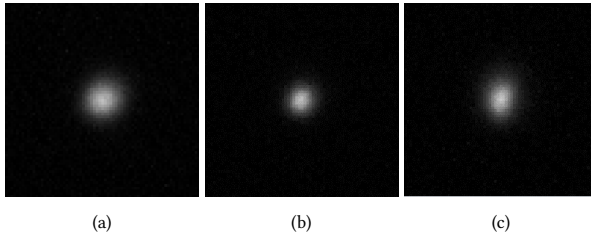


Figure 4.31: The photos of focused beam spots. (a) spot(6,6) at E1 of 20.925 kV, (b) spot(16,5) at E1 of 20.875 kV, (c) spot(17,17) at E1 of 20.725 kV.

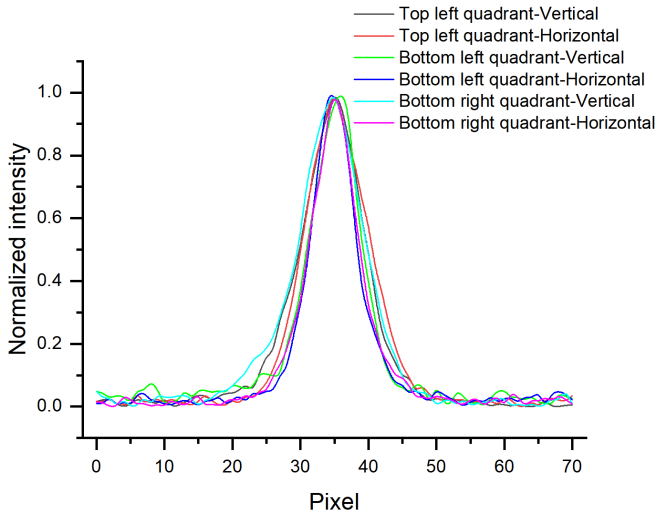


Figure 4.32: The vertical and horizontal profiles of the 3 spots.

top-left quadrant (figure 4.33). The narrowest widths in horizontal and vertical directions are smaller than the value when focused, although they emerge for various electrode focusing voltages of E1 group. The values in this graph are smaller than those in table 4.4, that is because the spot is rotated by 28 degrees clockwise to match the horizontal and

Table 4.4: The FWHM values of the spots

	TL-H	TL-V	BL-H	BL-V	BR-H	BR-V
FWHM / μm	3.9	3.6	2.8	2.8	3.0	3.8

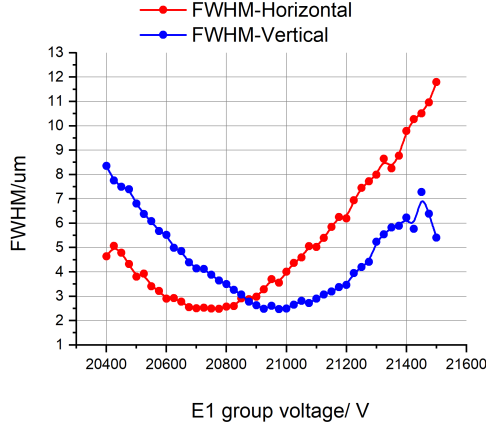


Figure 4.33: The FWHM values for the through-focus series of beam spot (6,6), the photos are rotated by 28 degrees to be straight.

vertical direction with the aperture pattern on ALA. The smallest width out of focus is about $2.5 \mu m$. And the expected value is $1.0 \mu m$, as shown in section 4.7.1.

4.7.3 BEAM CURRENT FOR ALL THE FOUR QUADRANTS

Table 4.5: The conditions used for the experimental measurement.

Filament current / A	YAG current / nA	Extractor voltage / kV	E1 group voltage / kV	E2 group voltage / kV
2.33	579	5.0	20.6	3.0

The beam current for every beamlet has been examined. We assume the light intensity is proportional to the beam current, so we sum up the intensity of all the beam spots (via camera photo) and calculate the percentage of individual spot intensities, then, we figure out the beam current for every electron beam. The results are shown in figure 4.34. Within each quadrant the current per beam fluctuated less than $0.1 nA$. The current range for the top left and bottom left quadrants (the round apertures) is from about $1.0 nA$ to about $1.08 nA$. The range for the top right quadrant is $1.30-1.44 nA$, and the range for the bottom right is from $1.1-1.2 nA$. All four quadrants show a trend that the beam current for the inner beams is higher than that of the outer beams.

The beamlet current in this experiment is about $1.0 nA$, which is less than the desired $5.0 nA$ current for every beamlet. The $5.0 nA$ beamlet current is derived from a $1.0 mA/sr$

angular intensity of a beam delivered from a Schottky source and 1.25 mrad half opening angle. However, we did not achieve both conditions in the experiment for two reasons as shown below.

- (a) **The Schottky source was not running at 1.0 mA/sr angular intensity.** The Schottky source in the experiment was running at about 0.3 mA/sr for some reasons, e.g. HV insulation between electrodes will deteriorate when we increase the beam current.
- (b) **The half opening angle is less than 1.25 mrad that we intend to use in the end.** In the mechanical design of the source, the thickness of the spacers is thicker than the value in the EOD model. However, the diameter of the apertures in the ALA is the same as it in the EOD model, therefore, the half opening angle of an aperture is less than the designed value of 1.25 mrad .

The source characterization experiment mentioned in chapter 3 proved that it's possible to reach 1.0 mA/sr angular intensity and below 1.0 mA extractor current for a $1.0 \mu\text{m}$ radius Schottky emitter. For a stable emission in long-term, 0.8 mA/sr angular intensity is feasible for a Schottky emitter.

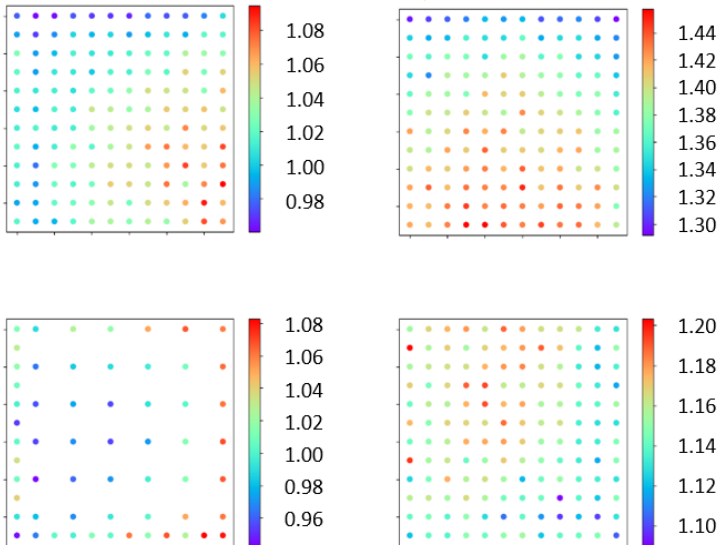


Figure 4.34: The current for the individual electron beam with the assumption that the intensity of the spot is proportional to the beam current. The unit for the color bar is nA .

4.7.4 ASTIGMATISM MANIPULATION WITH VOLTAGE SETTINGS.

From subsection 4.7.2, we know there is noticeable astigmatism in this MBS design, we would like to figure out if it's caused by the unoptimized voltage configuration or the unperfect alignment during the assembling. Thus, we did the simulation in EOD and made two setups of voltage, one setup had large astigmatism (table 4.6 I), and the other setup had small astigmatism (table 4.6 II). Astigmatism in the off-axis beams is caused by the spherical aberration of the macro lens (ZSL). We can manipulate the aberration by changing the voltage on the E2 group. The main difference between the two sets of data is the voltage of the E2 group and the corresponding focusing voltages on the E1 group. The voltages of electrodes in table 4.6 are with respect to ground.

Table 4.6: Two setups of voltages, one has large astigmatism (I), and the other has small astigmatism (II).

	I	II
Extraction voltage /kV	5.0	5.0
E11&E12 /kV	18.5-19.8	20.65-21.65
E21&E22 /kV	4.5	2.25
ALA /V	0	0
YAG /nA	530	630
Astigmatism coefficient/1/mm	3.86	1.44
Pitch mm	0.96	0.52

After applying the voltages according to table 4.6 on the MBS setup, we analyzed the acquired photos as described in section 4.5. The results are shown in figure 4.35. The dark purple dots are invalid data points as the post-processing failed.

Figure 4.35 shows that the FW50 results, and the voltage set with small astigmatism also

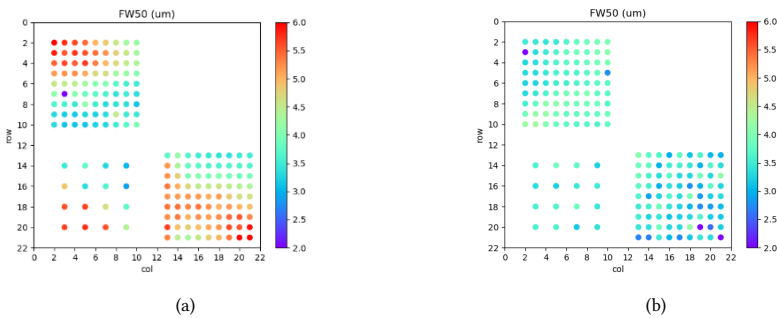


Figure 4.35: FW50 of the two setup voltages: Situation I (a) and situation II (b).

generates a smaller and more uniform spot size comparing to the other voltage set.

To evaluate the spot size without astigmatism, we need to examine the minimal width out of the focus plane/voltage. To represent the spots for this purpose, we created an ellipse model (figure 4.36), which we assume for every spot and further, has a 2D Gaussian current density distribution. The angle between the horizontal and the long axis of the ellipse

defines the rotation angle. All the spots are analyzed through the series of different E1 group voltages and compare the short axis to determine the spot's minimal width. Usually, this minimal width occurs outside the focusing plane/voltage. Therefore, we call these results the minimum width out of focus.

Figure 4.37 shows the minimum width out of focus for both voltage setups. In the right graph, there are many missing spots in the bottom left and bottom right quadrants caused by the processing software failure. Additionally, the simulated optimal shape does not achieve the smallest spot size (also see figure 4.30), we decided not to continue with this solution. Hereafter, we will concentrate on the top left quadrant of the ALA.

The minimal width of the top left quadrant is plotted in a histogram (figure 4.38), where

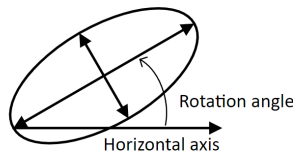


Figure 4.36: The assumption of the ellipse model.

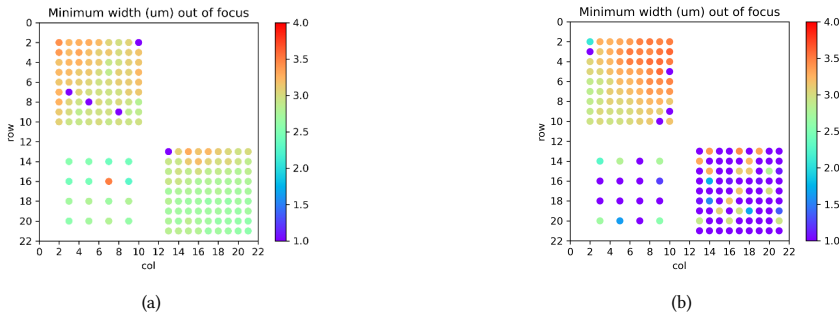


Figure 4.37: The minimum width out of focus for the situation I(a) and situation II(b).

it can be seen that voltage setting I has a better performance, taking the whole quadrant's minimal width into account. However, the astigmatism is larger for this voltage setting. Figure 4.39 and figure 4.40 show the through focus FW50 and minimal width of the spots on the diagonal for both situations I and situation II. For a larger astigmatism voltage setting, the spot size becomes larger from the center to the edge of the ALA, but the spot size of the voltage setting with small aberration is quite constant from the center to the edge.

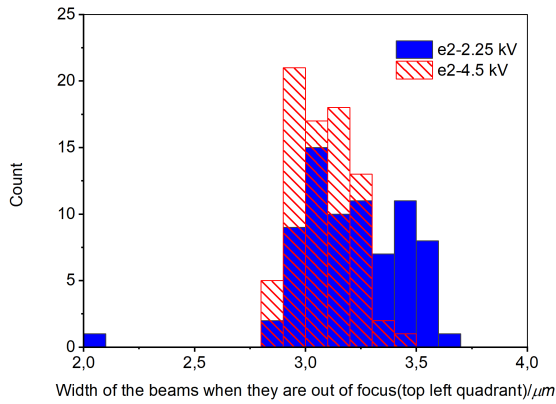


Figure 4.38: Histogram of the minimal width for the top left quadrant under two voltage settings.

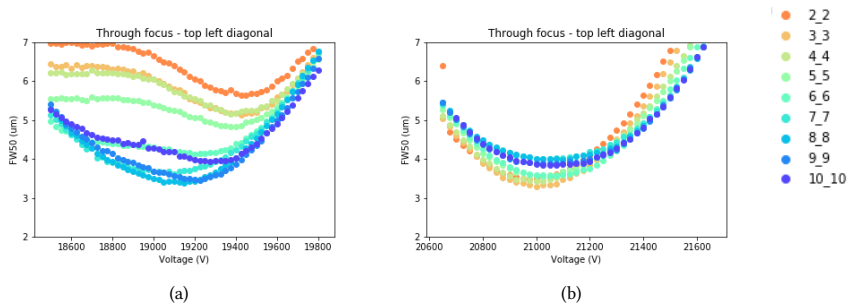


Figure 4.39: FW50 through focus series for the spots on the diagonal in the top left quadrant, (a). situation I , (b). situation II.

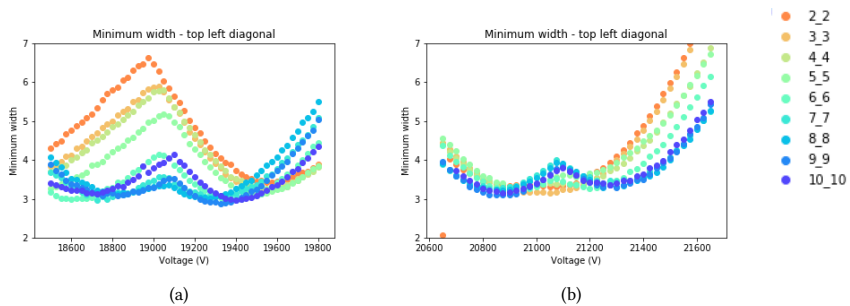
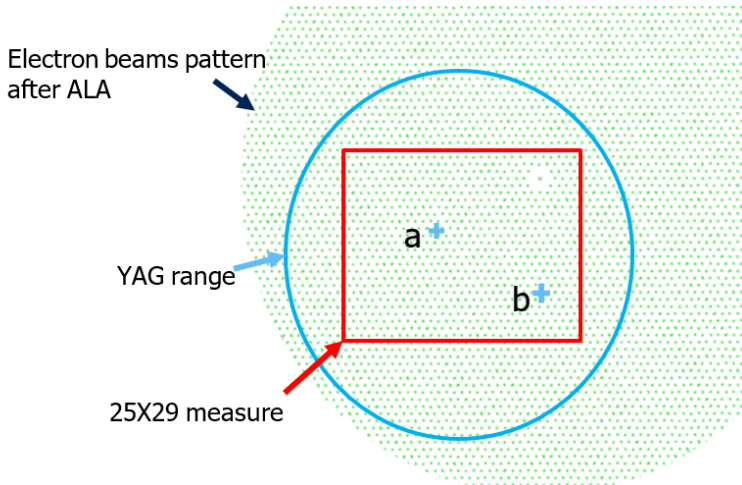


Figure 4.40: Minimum width through focus series for the spots on the diagonal in the top left quadrant, (a). situation I , (b). situation II.

4.8 MEASUREMENT FOR THE LARGE HEXAGONAL PATTERNED ALA.



4

Figure 4.41: Schematic diagram of the correlation between total electron beam at YAG plane, YAG screen, measure area, location a, and location b.

We designed an ALA in a hexagonal pattern, the aperture size is $20 \mu\text{m}$, and the distance from one aperture to another is $26 \mu\text{m}$, all the apertures are within a 2.0 mm circle. The surrounding apertures of the central aperture are left out as well as an aperture next to the circle of missing apertures; the latter is to indicate the orientation of the pattern. The green dots in figure 4.41 show most of the shadow images of the ALA.

Because there is a 0.5 mm displacement of the ALA with respect to the axis of the multi-

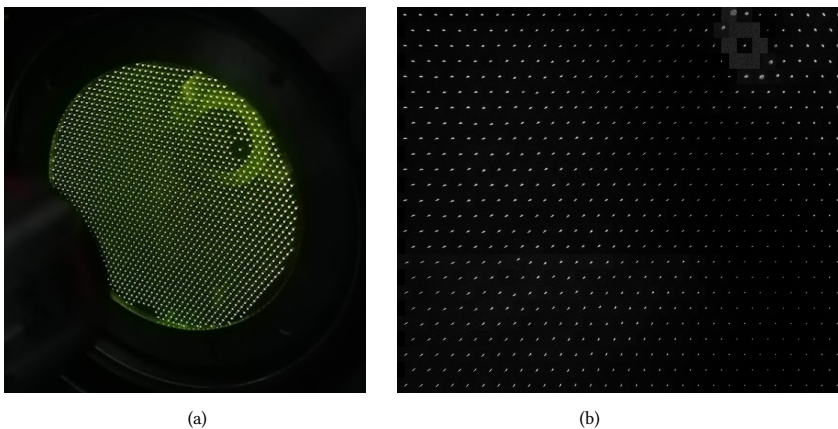


Figure 4.42: (a) The cell phone photo of beam spots on the YAG. (b) 25x29 beam spots in a stitched image.

beam source, the center of the ALA is not on the axis, whose center is given by location

a. The correlation between the beam spots and the YAG screen is shown in figure 4.41. We set the beam energy to 4 keV , E2 group voltage to 3 kV , and ALA to 0 V with respect to the ground potential and got focused beam spots when we set the E1 group voltage to around 16 kV . The beam current is about 1 nA per beamlet. In figure 4.42, a photo of the focused beam spots is shown, taken by a cell phone and stitched image of 25×29 beam spots taken by our optical microscope. From the stitched image, we found unexpected astigmatism for the spots over the whole YAG screen. Surprisingly, the spots at location b (figure 4.41) exhibit the least astigmatism. Therefore, two 9×9 spot areas are inspected, with the centers at locations a and b, respectively.

In table 4.7 the through-focus serial photos for the spots at locations a and b are given.

Table 4.7: Through focus serial photos for two different locations.

E1 voltage / kV	14.0	15.0	16.0	17.0
Location a				
Location b				

We observe that the spot at location b shows less astigmatism than at location a, and an apparent 12-pole effect can be seen for the E1 group voltage of 14.0 kV for both spots, which is what we expected.

We also analyzed both 9×9 spots area at locations a and b and display the FW50 and minimum width for the spots on the diagonal in figures 4.43 and 4.44, respectively. The minimum width of hexagonal patterned ALA can be as low as $2.1\ \mu\text{m}$ for the 4 keV electron beam. In contrast, the minimum width of a square patterned ALA could be as low as between $3.0\ \mu\text{m}$ and $3.5\ \mu\text{m}$ at 5.0 keV beam energy (figure 4.40).

Therefore, hexagonal patterned ALA can also suppress the octupole effect of an aperture lens array.

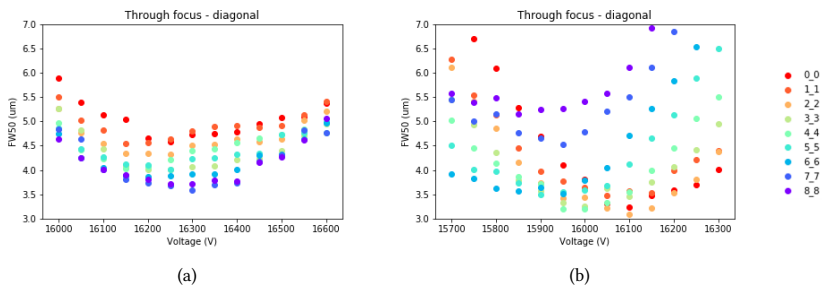


Figure 4.43: The FW50 for the spots on the diagonal of a. location a and b. location b.

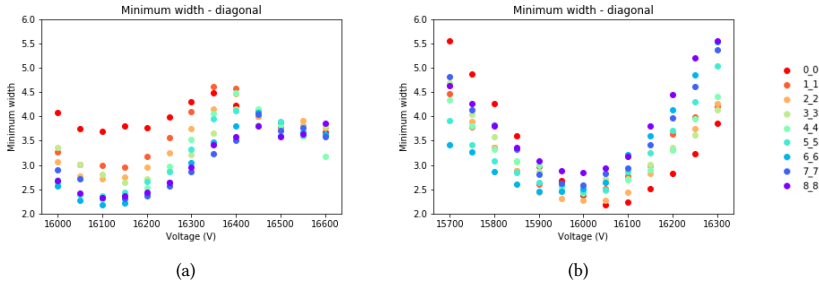


Figure 4.44: The minimum width for the spots on the diagonal of a. location a and b. location b.

4.9 MEASUREMENT FOR THE DECELERATING LENS MODE

We continue the MBS experiment on a horizontal demonstrator setup, which is aiming to prove the concept of the whole column including a MBS, and it has effective magnetic field shielding. There is a differential pumping aperture to separate the vacuum of the emitter chamber and the other vessels. This differential aperture is about 2.0 mm below ALA, has a 2.0 mm hole, and is always connected to ground potential.

We tried a decelerating lens mode in the MBS, because this mode can work with lower voltages with negative polarity with respect to ground, and we can save time from conditioning the electrode as we did in the normal accelerating lens mode. When a negative voltage is applied to the ALA, the lens between ALA and this differential pumping aperture will focus the electron beams. Unfortunately, the differential pumping aperture is not aligned with the other optical components, which may cause unexpected aberrations. Table 4.8 shows the voltage setting on the power supplies for the decelerating lens mode and the accelerating lens mode setting as a comparison, and the potential differences with respect to the emitter are included in the table.

Figure 4.45 shows two photos of the spots (not focused yet) on the YAG screen for both modes. The center spot is easy to recognize because of the absence of the spots around it. We can see a big distortion in the grid of decelerating lens mode, while the distortion is negligible in the grid of the accelerating lens mode.

Table 4.8: Voltage (w.r.t. ground) and potentials w.r.t. emitter for the decelerating lens mode and accelerating mode, unit is kV.

	w.r.t. ground	w.r.t. ground	w.r.t. emitter	w.r.t. emitter
Lens mode	Dec	Acc	Dec	Acc
PE energy	5.5	3.5	5.5	3.5
Emitter	-5.5	-3.5	0	0
Extractor	0	1.3	5.5	4.8
E1 group	-2	12.4~13.4	3.5	15.9~16.9
E2 group	-4.2	3.5	1.3	7
ALA	-3.3~ -3.4	0	2.1~2.2	3.5
Diff aperture	0	0	5.5	3.5

Figure 4.46 shows a selection of spots around the central beam spot (10, 10) with the

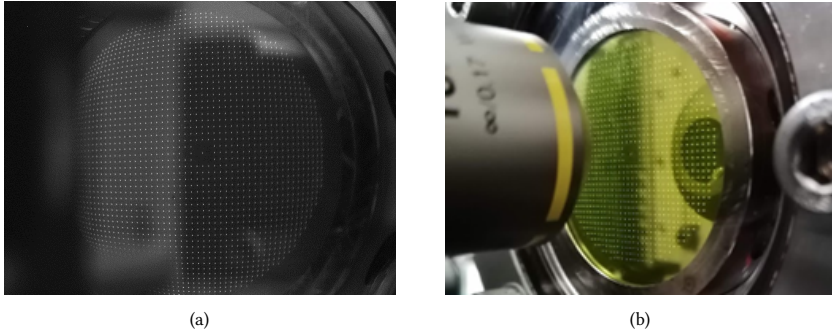


Figure 4.45: (a) Photos of the spot pattern on the YAG screen for a decelerating lens mode. (b) an accelerating lens mode.

coordinates at the border, the ALA voltage here is -3340 V , and we set the electrodes at the decelerating lens mode. We can see some double-dot shape spots in the figure with different orientations. We made through-focus series for two typical spots, indicated in the figure with green borders, shown in table 4.9. The spot (10, 3) is overfocused at -3340 V and shows a two-dot shape. There are still electrons distributed around and between the two dots at this voltage, and the shape turned into almost a horizontal line at voltage -3380 V . The spot (15, 10) displays the octupole effect when it is out of focus, but stretched by astigmatism to some extent. In order to find out if the double dots are a result of a damaged emitter with two emission spots, we went back to the accelerating mode although the maximum beam energy there was only 3.5 keV , limited by breakdowns at higher voltages of the E1 and E2 electrodes.

Table 4.9: Through focus series of two spots for the decelerating lens mode.

The voltage on ALA /kV	-3.25	-3.28	-3.30	-3.32	-3.34	-3.36	-3.38
(10, 3)							
The voltage on ALA /kV	-3.30	-3.32	-3.34	-3.345	-3.3	-3.38	-3.40
(15, 10)							

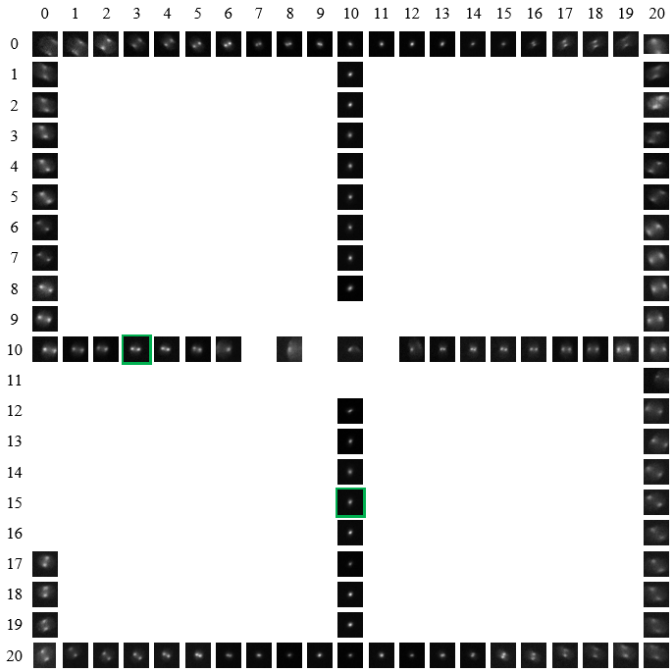


Figure 4.46: Some beam spots on the YAG screen for the decelerating lens mode.

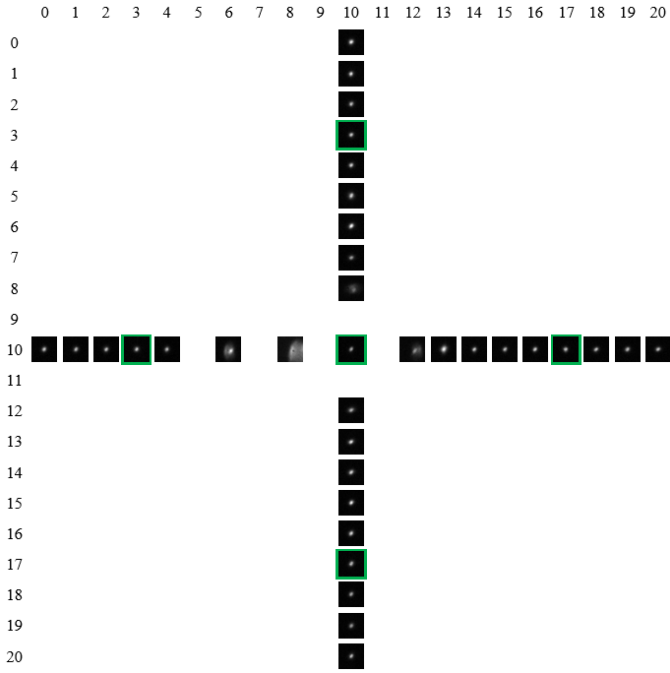


Figure 4.47: Some beam spots on the YAG screen for the accelerating lens mode.

Figure 4.47 shows a selection of spots around the central beam spot (10, 10) with the coordinates at the border, the E1 group electrode voltages here is 12.9 kV. The shape of all spots is a single dot, which proves that the double-dot shape for the deceleration lens mode is not caused by an abnormal emitter. We made through-focus series for several spots, again indicated with green borders. Through-focus series of these spots are shown in table 4.10. We can see the spot shape is uniform even when the spots are out of focus, except the central spot (10, 10). The asymmetric shape of the central spot when it is out of focus is probably caused by the asymmetry of its neighboring apertures, but could also be a result of charging of the aperture. In some spots, we can see a few hairline traces, which are scratches on the YAG screen surface generated in its manufacturing.

Table 4.10: Through focus series of several spots for the accelerating lens mode.

The voltage on E1 /kV	12.4	12.5	12.6	12.7	12.8	12.9	13.0	13.1
(10,3)								
(10,17)								
(3,10)								
(17,10)								
(10,10)								

Table 4.10: Through focus series of several spots for the accelerating lens mode(continued).

The voltage on E1 /kV	13.2	13.3	13.4	13.5
(10, 3)				
(10, 17)				
(3, 10)				
(17, 10)				
(10, 10)				

Now we are about to prove that the double-dot shape in figure 4.46 is not caused by the emitter, we try to explain it with aberration theory by simulating the spot shape with Zernike polynomials [69][70]. In light optics, for complicated aberrations, it is convenient to take a representation with completeness and orthogonality. In Noll's ordering scheme, index 5 (Z_2^{-2}) and 14 (Z_4^4) are astigmatism and fourfold effect, respectively, and we found

that with a combination of these two factors, the shapes in figure 4.46 and table 4.9 can be reproduced when the beams are out of focus.

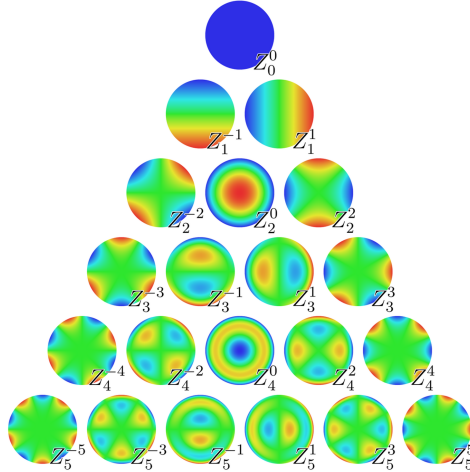


Figure 4.48: Zernike polynomials, ordered vertically by radial degree and horizontally by azimuthal degree [71].

The simulation including two aberrations is done in MATLAB and shown in table 4.11. In the table, we can see the spot shape in different planes for two typical spots (double-dot and single-dot shapes) in figure 4.46. Planes 1 to 5 represent five planes from under-focus to over-focus locations in the beam axis direction. The simulation of spot (10, 3) has more astigmatism than spot (15, 10). When we now look again at figure 4.46 we interpret the double dots in the most left and right vertical stripes as the result of astigmatism. From the fact that there is no astigmatism in the vertical stripe in the middle, we tentatively conclude that the differential pumping aperture is displaced horizontally with respect to the axis of the ALA chip.

When there is no obvious astigmatism, and only a fourfold effect exists, like what we have seen for the accelerating lens mode in figure 4.47 and table 4.10, the simulation also shows exactly the same through focus series in table 4.12.

Table 4.11: Simulation for two spots in decelerating lens mode.

Defocus	1	2	3	4	5
(10, 3)					
(15, 10)					

Table 4.12: Simulation for one spot in accelerating lens mode.

Defocus	1	2	3	4	5
					

4.10 CONCLUSIONS

In this chapter, we experimentally proved the possibility of manufacturing a Multi-Beam Source which can deliver a few hundred beams with a beam current of a few nA per beamlet and minimum spot widths between 2.1 and $3 \mu m$ at a $300 mm$ image plane. In many cases, there was astigmatism that increased the in-focus size of the spots.

We observed an obvious octupole effect for the square-patterned ALA and tried to compensate for it with shaped apertures. The simulation indicates that with a proper correction the FW50 value of the focused spot can be 65% of the value for a non-correct spot. However, the experimental results indicate that the octupole field generated by the shaped aperture is too sensitive to give a stable compensation of the octupole field generated by the surrounding apertures.

We did not find an indication that the off-axis spots have a noticeable coma or spreading by dispersion caused by the energy spread in the beams.

Hexagonal patterned apertures can also suppress the octupole field and leave a small 12-pole effect which will generate a smaller spot size.

With these solid experimental results, we are ready to build a demonstrator of the whole system, including the objective lenses and detection system. In the experiment, the measurement suffered from the $50 Hz$ electromagnetic noise. Therefore, the demonstrator should have a good magnetic shielding. It is also good to have the ability to adjust the position, pitch and rotation of the beam pattern, which can be done with certain coils in the MBS of the demonstrator.

Finally, we conclude that if the astigmatism and fourfold astigmatism (octupole effect) is corrected near the objective lenses, the system should be able to deliver a few hundred beams with the same quality as a beam in a single beam system.

5

SUMMARY

In this thesis, the author investigates the extended Schottky source for the application in a multi-beam source (MBS). The work has been done in both theoretical work and experimental work. The major conclusions are summarized in this chapter.

The goal of chapter 2 was to find the virtual source properties of off-axis beams from the Schottky source, beams which are usually created by positioning an off-axial aperture in the emission cone. We first reviewed some research on the off-axial electron beam in a source from the literature. Then, we briefly explained the theory of boundary element method (BEM). With the software CPO2D, which is based on the Boundary Element Method, we first did ray tracing of a Schottky source for the cold emitted electrons in a line. We calculated the spherical aberration coefficient for 10 apertures of 3 cases with the rays from the facet to a field-free plane. The first case is a radius $0.5 \mu\text{m}$ emitter at 5 kV extraction voltage, the second case is a radius $1.0 \mu\text{m}$ emitter at 5 kV extraction voltage, and the third case is also a radius $1.0 \mu\text{m}$ emitter but with 6 kV extraction voltage, the virtual source plane of the central aperture was chosen for the fitting. We also calculated some aberrations individually for on-axis and off-axial apertures.

We also derived the defocus and displacement of the meridional focus plane for the off-axial beams. We calculated the planes with these formulas and the spherical aberration coefficient from the last step.

By checking the emission area at the facet for an off-axial aperture in the field-free area, we calculated the virtual source size on both x and y directions for off-axial apertures. We found that the virtual source size is different in the x and y direction for off-axial beams, which must be taken into account for a multi-beam application.

We also calculated the size and shape of the aberrations, and we found that both the virtual source and aberration spot will be elongated in the y direction, and individual stigmators will be needed to correct for astigmatism. The blur caused by defocus and astigmatism, in the virtual source plane of the central beams, is smaller than the virtual source sizes up to the maximum polar angles for every case, and the virtual source size is the dominant contribution of the total source size in a Schottky source system.

In chapter 3, We aimed to achieve 1.0 mA/sr angular intensity for a radius of $1.0 \mu\text{m}$ TFE emitter, and we found it's possible for different emitter temperatures. The current in the dog ear area and emitted from the shank make things complicated, and we need to balance them and choose an intermediate emitter temperature.

From the angular intensity maps, we found that the uniform region could be as large as about 100 mrad from the emission pattern center (optical axis). These should be the physical limitations caused by the TFE source for the multi-beam application. Of course, engineering may give other limits to the range that we can utilize.

We found it challenging to maintain a stable emission at 1.0 mA/sr for a large opening angle from the long-term running curve. The YAG screen current drops all the time though the angular intensity keeps more or less the same, it's because the morphologic changes happened at the edge of the emitter facet in a long-term running, and it's not good for the long-term stability for a multi-beam application which needs current from both the center and off-axial area.

We also found the YAG current could be reasonably stable for the whole emitting facet at 0.81 mA/sr angular intensity. A constant YAG current indicates a stable facet shape without morphologic change or further faceting of the tip, and this is essential for a multi-beam source that is supposed to work perfectly for a whole year.

We speculate that to obtain a stable 1.0 mA/sr for up to 100 mrad half opening angle, an emitter with slightly larger radius should be chosen.

5

In chapter 4, we experimentally proved the possibility of manufacturing a Multi-Beam Source which can deliver a few hundred beams with a beam current of a few nA per beamlet and minimum spot widths between 2.1 and $3 \mu\text{m}$ at a 300 mm image plane. In many cases, there was astigmatism that increased the in-focus size of the spots.

We observed an obvious octupole effect for the square-patterned ALA and tried to compensate for it with shaped apertures. The simulation indicates that with a proper correction the FW50 value of the focused spot can be 65% of the value for a non-correct spot. However, the experimental results indicate that the octupole field generated by the shaped aperture is too sensitive to give a stable compensation of the octupole field generated by the surrounding apertures.

We did not find an indication that the off-axis spots have a noticeable coma or spreading by dispersion caused by the energy spread in the beams.

Hexagonal patterned apertures can also suppress the octupole field and leave a small 12-pole effect which will generate a smaller spot size.

With these solid experimental results, we are ready to build a demonstrator of the whole system, including the objective lenses and detection system. In the experiment, the measurement suffered from the 50 Hz electromagnetic noise. Therefore, the demonstrator should have a good magnetic shielding. It is also good to have the ability to adjust the position, pitch and rotation of the beam pattern, which can be done with certain coils in the MBS of the demonstrator.

Finally, we conclude that if the astigmatism and fourfold astigmatism (octupole effect) is corrected near the objective lenses, the system should be able to deliver a few hundred beams with the same quality as a beam in a single beam system.

6

SAMENVATTING

Samenvatting In dit proefschrift onderzoekt de auteur de eigenschappen van de Schottky-bron voor toepassing in een multi-bundel bron (MBS). Het bevat zowel theoretisch als experimenteel werk. De belangrijkste conclusies zijn in dit hoofdstuk samengevat.

Het doel van hoofdstuk 2 was om de eigenschappen van de virtuele bron te vinden van niet-axiale bundels van de Schottky-bron, bundels die meestal worden gecreëerd door een naast de as geplaatst apertuur in de emissiekegel te zetten. We hebben eerst wat onderzoek naar niet-axiale elektronenbundels besproken zoals gevonden in de literatuur.

Vervolgens hebben we kort de theorie van de ladingsdichtheid methode (BEM) uitgelegd die de basis vormt van de software CPO2D waarmee we baanberekeningen hebben gedaan van een Schottky-bron. We berekenden de sferische aberratiecoëfficiënt voor 10 openingen van 3 gevallen met de stralen van het facet naar een veldvrij vlak. Het eerste geval is een tip met een straal van $0,5 \mu\text{m}$ bij een extractiespanning van 5 kV , het tweede geval is een tip met een straal van $1,0 \mu\text{m}$ bij een extractiespanning van 5 kV , en het derde geval is ook een tip met een straal van $1,0 \mu\text{m}$, maar met een extractiespanning van 6 kV , de virtuele Voor de fitting werd gekozen voor het bronvlak van de centrale opening. We hebben ook enkele aberraties individueel berekend voor openingen op de as en buiten de axiale richting. We hebben ook de defocus en verplaatsing van het meridionale focusvlak afgeleid voor de niet-axiale bundels. We hebben de vlakken berekend met deze formules en de sferische aberratiecoëfficiënt uit de laatste stap.

Door het emissiegebied aan het facet te controleren op een niet-axiale opening in het veldvrije gebied, berekenden we de virtuele brongrootte in zowel de x- als de y-richting voor niet-axiale openingen. We ontdekten dat de virtuele brongrootte verschillend is in de x- en y-richting voor niet-axiale bundels, waarmee rekening moet worden gehouden bij een toepassing met meerdere bundels.

We hebben ook de grootte en vorm van de aberraties berekend en we hebben vastgesteld dat zowel de virtuele bron als de aberratievlek in de y-richting groter zijn dan in de x-richting, en dat er individuele stigmatoren nodig zullen zijn om astigmatisme te corrigeren. De onscherpte veroorzaakt door onscherpte en astigmatisme in het virtuele bronvlak van de centrale bundels is kleiner dan de virtuele brongroottes, tot aan de maximale polaire

hoeken voor elk geval, en de virtuele brongrootte is de dominante bijdrage van de totale brongrootte in een Schottky-bron systeem.

In hoofdstuk 3 streefden we naar een hoekintensiteit van $1,0 \text{ mA/sr}$ te bereiken voor een straal van $1,0 \mu\text{m}$ TFE tip, en we ontdekten dat dit mogelijk is voor verschillende emittertemperaturen. De stroom in het gebied van het hondenoor en de stroom die door de schacht wordt uitgezonden, maken de zaken ingewikkeld, en we moeten ze in evenwicht brengen en een tussenliggende emittertemperatuur kiezen.

Uit de hoekintensiteitskaarten hebben we ontdekt dat het uniforme gebied ongeveer 100 mrad vanaf het centrum van het emissiepatroon (optische as) kan bedragen. Dit is dan de fysieke beperking die wordt veroorzaakt door de TFE-bron voor de toepassing met meerdere bundels. Uiteraard kan de techniek andere grenzen stellen aan het bereik dat we kunnen benutten.

We vonden het een uitdaging om een stabiele emissie van $1,0 \text{ mA/sr}$ te handhaven voor een grote openingshoek ten opzichte van de langetermijncurve. De YAG-schermstroom daalt voortdurend, hoewel de hoekintensiteit min of meer hetzelfde blijft. Dit komt doordat de morfologische veranderingen op de lange termijn aan de rand van het emitterfacet plaatsvonden, en dat is niet goed voor de stabiliteit op lange termijn voor een toepassing met meerdere bundels die stroom nodig heeft vanuit zowel het midden als het niet-axiale gebied.

We ontdekten ook dat de YAG-stroom redelijk stabiel kon zijn voor het hele emitterende facet bij een hoekintensiteit van $0,81 \text{ mA/sr}$. Een constante YAG-stroom duidt op een stabiele facetvorm zonder morfologische verandering of verdere facettering van de punt, en dit is essentieel voor een bron met meerdere bundels die een heel jaar perfect zou moeten werken.

We speculeren dat om een stabiele $1,0 \text{ mA/sr}$ te verkrijgen voor een halve openingshoek van maximaal 100 mrad , een emitter met een iets grotere straal moet worden gekozen.

In hoofdstuk 4 hebben we experimenteel de mogelijkheid bewezen om een Multi-Beam Source te vervaardigen die een paar honderd bundels kan leveren met een bundelstroom van een paar nA per bundeltje en minimale spotbreedtes tussen $2,1$ en $3 \mu\text{m}$ bij een beeldvlak van 300 mm . In veel gevallen was er sprake van astigmatisme waardoor de scherpte van de vlekken groter werd.

We observeerden een duidelijk achtpooleffect veroorzaakt door de aperture lens array ALA met vierkant patroon en probeerden dit te compenseren met niet-ronde openingen. De simulatie geeft aan dat met een juiste correctie de FW50-waarde van de gefocusseerde vlek 65% kan zijn van de waarde voor een niet-correcte vlek. De experimentele resultaten geven echter aan dat het door de niet-ronde opening gegenereerde achtpoolveld te gevoelig is om een stabiele compensatie te geven van het achtpoolveld dat door de omringende openingen wordt gegenereerd.

We hebben geen indicatie gevonden dat de plekken buiten de as een merkbare coma hebben of zich verspreiden door dispersie veroorzaakt door de energienverspreiding in de bundels. Zeshoekige openingen met patroon kunnen ook het achtpoolveld onderdrukken en een klein 12-polig effect achterlaten dat een kleinere vleggrootte genereert. Met deze solide experimentele resultaten zijn we klaar om een demonstrator van het hele systeem te

bouwen, inclusief de objectieflenzen en het detectiesysteem. In het experiment had de meting last van de elektromagnetische ruis van 50 Hz . Daarom moet de demonstrator een goede magnetische afscherming hebben. Het is ook goed om de mogelijkheid te hebben om de positie, toonhoogte en rotatie van het straalpatroon aan te passen, wat gedaan kan worden met bepaalde spoelen in de MBS van de demonstrator.

Ten slotte concluderen we dat als het astigmatisme en het viervoudige astigmatisme (octupoleeffect) worden gecorrigeerd nabij de objectieflenzen, het systeem in staat zou moeten zijn om een paar honderd bundels te leveren met dezelfde kwaliteit als een bundel in een enkel bundelsysteem.

BIBLIOGRAPHY

REFERENCES

- [1] Andras E. Vladar and Michael T. Postek. The scanning electron microscope. In *book* [25], pages 437–496. CRC Press, 2009.
- [2] Ankush Oberai and Jiann Shiun Yuan. Smart E-beam for defect identification & analysis in the nanoscale technology nodes: Technical perspectives. *Electronics (Switzerland)*, 6(4):1–28, 2017.
- [3] Hitachi High-Tech Corporation. Semiconductor Manufacturing. <https://www.hitachi-hightech.com/global/en/knowledge/semiconductor/room/manufacturing/>. [Online, accessed 28-December-2023].
- [4] Renjie Zhou, Chris Edwards, Amir Arbabi, Gabriel Popescu, and Lynford L Goddard. Detecting 20 nm Wide Defects in Large Area Nanopatterns Using Optical Interferometric Microscopy. *Nano Letters*, 13(8):3716–3721, 2013.
- [5] Sanyogita Purandare, Jinlong Zhu, Renjie Zhou, Gabriel Popescu, Alexander Schwing, and Lynford L Goddard. Optical inspection of nanoscale structures using a novel machine learning based synthetic image generation algorithm. *Optics Express*, 27(13):17743, 2019.
- [6] J E Barth and P Kruit. Addition of different contributions to the charged particle probe size. *Optik (Jena)*, 101(3):101–109, 1996.
- [7] T H P Chang. Arrayed miniature electron beam columns for high throughput sub-100 nm lithography. *Journal of Vacuum Science & Technology B: Microelectronics and Nanometer Structures*, 10(6):2743, 1992.
- [8] J E Schneider. Semiconductor on glass photocathodes as high-performance sources for parallel electron beam lithography. *Journal of Vacuum Science & Technology B: Microelectronics and Nanometer Structures*, 14(6):3782, 1996.
- [9] T H Newman, R F W Pease, and W DeVore. DOT MATRIX ELECTRON BEAM LITHOGRAPHY. In *Journal of Vacuum Science and Technology B: Microelectronics and Nanometer Structures*, volume 1, pages 999–1002. American Vacuum Society AVS, 1983.
- [10] Hiroshi Yasuda, Soichiro Arai, Jun Ichi Kai, Yoshihisa Ooae, Tomohiko Abe, Yasushi Takahashi, Syunsuke Hueki, Sigeru Maruyama, Satoru Sago, and Keiichi Betsui. Fast Electron Beam Lithography System With 1024 Beams Individually Controlled By

- Blanking Aperture Array. *Japanese Journal of Applied Physics*, 32(12 S):6012–6017, 1993.
- [11] P Kruit. The role of MEMS in maskless lithography. *Microelectronic Engineering*, 84(5-8):1027–1032, 2007.
- [12] E Slot, M J Wieland, de G Boer, P Kruit, ten G F Berge, A M C Houkes, R Jager, van de T Peut, J J M Peijster, S W H K Steenbrink, T F Teepen, van A H V Veen, and B J Kampherbeek. MAPPER: high throughput maskless lithography. <https://doi.org/10.1117/12.771965>, 6921:517–525, 2008.
- [13] Yanxia Zhang. *A 100-electron-beam source from a high brightness Schottky emitter for fast patterning applications*. PhD thesis, TU Delft, 2008.
- [14] M J Van Bruggen, B Van Someren, and P Kruit. Development of a multi-electron-beam source for sub- 10 nm electron beam induced deposition. *Journal of Vacuum Science and Technology B: Microelectronics and Nanometer Structures*, 23(6):2833–2839, 2005.
- [15] A Mohammadi-Gheidari, C W Hagen, and P Kruit. Multibeam scanning electron microscope: Experimental results. *Journal of Vacuum Science & Technology B, Nanotechnology and Microelectronics: Materials, Processing, Measurement, and Phenomena*, 28(6):C6G5–C6G10, 2010.
- [16] Wilco Zuidema and Pieter Kruit. Transmission imaging on a scintillator in a scanning electron microscope. *Ultramicroscopy*, 218:113055, 2020.
- [17] A L Eberle, S Mikula, R Schalek, J Lichtman, M L Knothe Tate, and D Zeidler. High-resolution, high-throughput imaging with a multibeam scanning electron microscope. *Journal of Microscopy*, 259(2):114–120, 2015.
- [18] Thomas Kemen, Matt Malloy, Brad Thiel, Shawn Mikula, Winfried Denk, Gregor Dellemann, and Dirk Zeidler. Further advancing the throughput of a multi-beam SEM. *Metrology, Inspection, and Process Control for Microlithography XXIX*, 9424:94241U, 2015.
- [19] Yan Ren. *Imaging Systems for the Delft Multi- Beam Scanning Electron Microscope 1*. PhD thesis, TU Delft, 2017.
- [20] M S Bronsgeest, J E Barth, L W Swanson, and P Kruit. Probe current, probe size, and the practical brightness for probe forming systems. *Journal of Vacuum Science and Technology B: Microelectronics and Nanometer Structures*, 26(3):949–955, 2008.
- [21] Merijn Bronsgeest. *PHYSICS OF SCHOTTKY ELECTRON SOURCES*. PhD thesis, TU Delft, 2009.
- [22] Pieter Kruit. Cathodes for Electron Microscopy and Lithography. *Topics in Applied Physics*, 135:251–292, 2020.

- [23] van den A J Brom, van A H V Veen, W M Weeda, G Z M Berglund, M Wieland, and P Kruit. Cathode ray tube type electron gun as a source for multibeam electron lithography. *Journal of Vacuum Science & Technology B: Microelectronics and Nanometer Structures Processing, Measurement, and Phenomena*, 25(6):2245, 2007.
- [24] SK Chapman. Optimising the performance of a tungsten hairpin scanning electron microscope. *Scanning Microscopy*, 13(1):141–146, 1999.
- [25] Jon Orloff. *Handbook of Charged Particle Optics, Second edition*. CRC Press, 2009.
- [26] Sean M Kellogg, Kun Liu, Gregory A Schwind, and Lynwood W Swanson. Off-axis modeling and measurement of emission parameters for the Schottky emitter. *Journal of Vacuum Science and Technology B: Microelectronics and Nanometer Structures*, 31(6), 2013.
- [27] Shin Fujita and Hiroshi Shimoyama. Theory of cathode trajectory characterization by canonical mapping transformation. *Journal of Electron Microscopy*, 54(4):331–343, 2005.
- [28] CPO Limited. CPO2D software. <https://www.electronoptics.com/>. [Online, accessed 28-December-2023].
- [29] A. Mohammadi-Gheidari and P. Kruit. Electron optics of multi-beam scanning electron microscope. *Nuclear Instruments and Methods in Physics Research, Section A: Accelerators, Spectrometers, Detectors and Associated Equipment*, 645(1), 2011.
- [30] H Craig Miller. Flashover of insulators in vacuum the last twenty years. *IEEE Transactions on Dielectrics and Electrical Insulation*, 22(6):3641–3657, 2015.
- [31] R. A. Anderson and J. P. Brainard. Mechanism of pulsed surface flashover involving electron-stimulated desorption. *Journal of Applied Physics*, 51(3):1414–1421, 1980.
- [32] J. Worster. The brightness of electron beams systems. *Journal of Physics D: Applied Physics*, 2(3):457–462, 1969.
- [33] J. C. Wiesner, T. E. Everhart, D. W. Tuggle, J. Z. Li, L. W. Swanson, J. C. Wiesner, and T. E. Everhart. Point-cathode electron sources-electron optics of the initial diode region. *Journal of Applied Physics*, 45(6):2797–2798, may 1974.
- [34] L. W. Swanson and N. A. Martin. Field electron cathode stability studies: Zirconium/tungsten thermal-field cathode. *Journal of Applied Physics*, 46(5):2029–2050, 1975.
- [35] D. W. Tuggle, J. Z. Li, and L. W. Swanson. Point cathodes for use in virtual source electron optics. *Journal of Microscopy*, 140(3):293–301, dec 1985.
- [36] Richard Young, Sander Henstra, Jarda Chmelik, Trevor Dingle, Albert Mangnus, Gerard van Veen, and Ingo Gestmann. XHR SEM: enabling extreme high resolution scanning electron microscopy. *Scanning Microscopy 2009*, 7378(May 2009):737803, 2009.

- [37] Harald H. Rose. *Geometrical Charged-Particle Optics*. Springer Berlin Heidelberg, Nov 2010.
- [38] Shin Fujita and Hiroshi Shimoyama. A new evaluation method of electron optical performance of high beam current probe forming systems. *Journal of Electron Microscopy*, 54(5):413–427, 2005.
- [39] K. Liu, G. A. Schwind, L. W. Swanson, and J. A. Campbell. Field induced shape and work function modification for the ZrO/W(100) Schottky cathode. *Journal of Vacuum Science & Technology B, Nanotechnology and Microelectronics: Materials, Processing, Measurement, and Phenomena*, 28(6):C6C26–C6C33, 2010.
- [40] M. S. Bronsgeest and P. Kruit. Reversible shape changes of the end facet on Schottky electron emitters. *Journal of Vacuum Science & Technology B: Microelectronics and Nanometer Structures Processing, Measurement, and Phenomena*, 27(6):2524, dec 2009.
- [41] S. Fujita, T. R.C. Wells, W. Ushio, H. Sato, and M. M. El-Gomati. Enhanced angular current intensity from Schottky emitters. *Journal of Microscopy*, 239(3):215–222, 2010.
- [42] K. Liu, G. A. Schwind, and L. W. Swanson. Off-axis emission properties for the extended Schottky electron source. *Journal of Vacuum Science and Technology B: Microelectronics and Nanometer Structures*, 27(6):2547–2552, 2009.
- [43] Frank H. Read and Nicholas J. Bowring. Simulation of thermionic cathodes. *Nuclear Instruments and Methods in Physics Research, Section A: Accelerators, Spectrometers, Detectors and Associated Equipment*, 531(3):407–415, 2004.
- [44] F. H. Read, A. Adams, and J. R. Soto-Montiel. Electrostatic cylinder lenses. I. Two element lenses. *Journal of Physics E: Scientific Instruments*, 4(9):625, sep 1971.
- [45] John T. Katsikadelis. The Boundary Element Method for Engineers and Scientists: Theory and Applications: Second Edition. *The Boundary Element Method for Engineers and Scientists: Theory and Applications: Second Edition*, pages 1–446, jul 2016.
- [46] Lyn Swanson and Gregory Schwind. Review of ZrO/W Schottky Cathode. In *Handbook of Charged Particle Optics, Second Edition*, pages 1–28. CRC Press, dec 2008.
- [47] W SCHERLE. Beschreibung von Aberrationen mit Begriffen der Statistik. *Optik (Stuttgart)*, 67(4), 1984.
- [48] E KASPER. On the numerical determination of electron optical focusing properties and aberrations. *Optik (Stuttgart)*, 69(3):117–125, 1985.
- [49] M.A.J. A.J. J van der Stam and P. Kruit. A general framework for numerical calculation of properties of charged-particle optical systems. *Nuclear Instruments and Methods in Physics Research, Section A: Accelerators, Spectrometers, Detectors and Associated Equipment*, 427(1-2):368–374, may 1999.
- [50] M Oral and B Lencová. Calculation of aberration coefficients by ray tracing. *Ultramicroscopy*, 109(11):1365–1373, 2009.

- [51] J. K. Trolan, J. P. Barbour, E. E. Martin, and W. P. Dyke. Electron Emission from a Lattice Step on Clean Tungsten. *Physical Review*, 100(6):1646, dec 1955.
- [52] J. P. Barbour, F. M. Charbonnier, W. W. Dolan, W. P. Dyke, E. E. Martin, and J. K. Trolan. Determination of the Surface Tension and Surface Migration Constants for Tungsten. *Physical Review*, 117(6):1452, mar 1960.
- [53] M. S. Bronsgeest and P. Kruit. 'Collapsing rings' on Schottky electron emitters. *Ultramicroscopy*, 110(9):1243–1254, 2010.
- [54] MS Bronsgeest and P Kruit. Effect of the electric field on the form stability of a schottky electron emitter: A step model. *Journal of Vacuum Science & Technology B: Microelectronics and Nanometer Structures Processing, Measurement, and Phenomena*, 26(6):2073–2079, 2008.
- [55] Shin Fujita and Hiroshi Shimoyama. Mechanism of surface-tension reduction by electric-field application: Shape changes in single-crystal field emitters under thermal-field treatment. *Physical Review B - Condensed Matter and Materials Physics*, 75(23):1–10, 2007.
- [56] Alan Bahm, Greg Schwind, and Lyn Swanson. The ZrO/W(100) Schottky cathode: Morphological modification and its effect on long term operation. *Journal of Applied Physics*, 110(5), 2011.
- [57] Itseez. Open Source Computer Vision Library. <https://github.com/itseez/opencv>, 2015. [Online, accessed 29-December-2023].
- [58] Python Core Team. Python: A dynamic, open source programming language. <https://www.python.org/>, 2019. [Online, accessed 29-December-2023].
- [59] D. W. Tuggle and L. W. Swanson. EMISSION CHARACTERISTICS OF THE ZrO/W THERMAL FIELD ELECTRON SOURCE. *Journal of Vacuum Science & Technology B: Microelectronics Processing and Phenomena*, 3(1):220–223, 1984.
- [60] J Zlamal and B Lencova. Development of the program EOD for design in electron and ion microscopy. *Nuclear Instruments and Methods in Physics Research, Section A: Accelerators, Spectrometers, Detectors and Associated Equipment*, 645(1):278–282, 2011.
- [61] A. A. Maznev and O. B. Wright. Upholding the diffraction limit in the focusing of light and sound. *Wave Motion*, 68, 2017.
- [62] Max Born, Emil Wolf, A. B. Bhatia, P. C. Clemmow, D. Gabor, A. R. Stokes, A. M. Taylor, P. A. Wayman, and W. L. Wilcock. *Principles of Optics*. Cambridge University Press, oct 1999.
- [63] A H J Bansagi, R Duba, S S Grimbergen, M D Klapwijk, T Nagaki, and R P Rikken. Magnetic field compensating system for a Scanning Electron Microscope. *TU Delft Master project*, 2015.

- [64] Ludwig Reimer Helmut Kohl. *Transmission electron microscopy : physics of image formation*. Springer series in optical sciences:36. Springer New York, NY, 5th edition, 2008.
- [65] Pulsar Physics. GPTwebpage. <http://www.pulsar.nl/gpt>. [Online, accessed 29-December-2023].
- [66] A Mohammadi-Gheidari, ER Kieft, X Guo, M Wisse, and P Kruit. In multi electron beam systems,“neighbours matter”. *Ultramicroscopy*, 249:113735, 2023.
- [67] Martijn J Adriaans. Multibeam electron optical system - neighbors matter. <https://research.tue.nl/nl/studentTheses/multibeam-electron-optical-system-neighbours-matter>, 2020. [Master Thesis, TU Eindhoven, accessed 28-December-2023].
- [68] James B Pawley. Points, pixels, and gray levels: Digitizing image data. *Handbook of Biological Confocal Microscopy: Third Edition*, pages 59–79, 2006.
- [69] F Zernike and F J M Stratton. Diffraction Theory of the Knife-Edge Test and its Improved Form, The Phase-Contrast Method. *Monthly Notices of the Royal Astronomical Society*, 94(5):377–384, 1934.
- [70] Jason D. Schmidt. *Numerical Simulation of Optical Wave Propagation: With Examples in MATLAB*. SPIE, 2010.
- [71] Wikimedia Commons. Zernike polynomials, ordered vertically by radial degree and horizontally by azimuthal degree. https://commons.wikimedia.org/wiki/File:Zernike_polynomials2.png, 2008. [Online, accessed 29-December-2023].

ACKNOWLEDGMENTS

I started my Ph.D project in Delft since in June 2017. It has been a great journey to explore the edge of science and technology these years. I could not have undertaken this journey without the support and help of many people.

First, I would like to express my deepest appreciation to Prof. Pieter Kruit. Pieter has generously provided his knowledge and expertise in many different aspects, and we had many fruitful discussions on electron optics and other topics. He also provided an enormous help to me when I was writing my thesis. Additionally, this achievement would not have been possible without the generous support from Applied Materials, who financially supported my research and provided some key equipment for the project. Ron Naftali from Applied Materials gave a lot of feedback on the work.

I am also grateful to my colleagues in MInT/CPO group of Applied Science faculty, who have contributed to this sophisticated research. Marco Wisse, Ali Mohammadi Gheidari, and Martin Kamerbeek also worked on the project and helped me with preparing the experiments. Johan van der Cingel helped with building up the vacuum system, Paul Keijzer and Han van der Linden built many electronics for the setup, Carel Heerkens and Martin Kamerbeek made the essential MEMS parts for the project. Ruud van Tol did most of the mechanical design work for the setups mentioned in the thesis.

Lastly, I would be remiss in not mentioning my family, especially my wife, Hui Wang, and daughter Yuchen (Bella) Guo. Their belief in me has supported me during this process, especially during the hard moments of COVID-19.

*Xiaoli
Delft, January 2024*

CURRICULUM VITÆ

Xiaoli Guo

Jan 1981 Born in Xinxiang city, Henan Province, China.

EDUCATION

Sep 1999– Jun 2003 Xi'an Jiaotong University
Bachelor's degree in Electronic Science and Technology

Sep 2003– Jun 2006 Xi'an Jiaotong University
Master's degree in Physical Electronics

EXPERIENCE

Jun 2006– May 2017 Hermes Microvision Inc. (Beijing)
Senior Electron Optics Engineer

Jun 2017– May 2021 Delft University of Technology, the Netherlands
PH.D candidate

Jun 2021– Nov 2022 Delft University of Technology, the Netherlands
Postdoc

Dec 2022– Dec 2023 Applied Materials, the Netherlands
Scientist